Aus der Klinik für Nuklearmedizin

Direktor: Prof. Dr. med. Markus Luster

des Fachbereichs Medizin der Philipps-Universität Marburg

Data-Driven Iterative Image Reconstruction For Motion Correction In Head Computed Tomography

Inaugural-Dissertation

zur Erlangung des Doktorgrades der Naturwissenschaften

dem Fachbereich Medizin der Philipps-Universität Marburg

vorgelegt von

Afshan Ashfaq

aus Lahore, Pakistan

Marburg, 2022

Angenommen vom Fachbereich Medizin der Philipps-Universität Marburg am: 31.08.2022

Gedruckt mit Genehmigung des Fachbereichs.

Dekanin: Prof. Dr. Denise Hilfiker-Kleiner

Referent: Prof. Dr. Markus Luster

Dr. Tino Schurrat

Korreferent: Prof. Dr. Martin Fiebich

Abstract

Computed tomography (CT) has become the diagnostic modality of choice for head trauma due to its accuracy, reliability, safety, and its availability. CT scanning of the head is typically used to detect infarction, calcifications, tumors, bone trauma, and hemorrhage.

Motion correction (MC) is of general interest in CT imaging. Motion correction techniques have two categories. The first group requires motion information and consists of motion acquisition and motion compensation processes. The motion acquisition derives the motion information from reference images, surrogate signals, or the data themselves. Motion compensation compensates the motion during a reconstruction process. The second group is based on image-processing techniques and corrects the motion without prior knowledge of the motion. Based on what prior information is available, one can choose the appropriate approach to perform the motion correction. A CT motion correction method prototype was available from the University of Sydney. The technique is based on the rigid motion of the helical head CT scans and only requires the measured data as the available information. A 3D registration of the object to each 2D view was accomplished individually to estimate the position of the object for each acquired CT view. The initial rough estimate of the 3D object is achieved with a preliminary reconstruction without incorporating motion compensation with this intermediate estimated motion, a motion-compensated reconstruction can be performed. The motion and reconstructed image can be updated alternately within a multi-resolution scheme until an optimal motion estimate is found. The final compensation can be performed in a fine-resolution reconstruction process with acceleration.

The study aimed to validate the data-driven 3D iterative motion estimation (ME) and motion compensation algorithm on phantom as well as clinical studies with head movements during computed tomography (CT) scan and to optimize the data-driven 3D iterative algorithm for robust application.

The Hoffman 3D brain phantom provides a quantitative and qualitative study of the three-dimensional effects of scatter and attenuation similar to the human brain. Water-filled Hoffman brain phantom acquired on Siemens Biograph mCT scanners with 128 slice CT scanner (Siemens Medical Solutions USA, Inc., Malvern, PA) using routine head CT. A reference stationary helical CT scan (gold standard) of the phantom was acquired and afterward, a series of CT scans were acquired with a variety of motions. The effect of MC on phantom CT scans was evaluated by comparing the gold standard stationary phantom images with corresponding

uncorrected and MC images. The phantom scans with small to moderate motion were reconstructed without artifacts. But for fast motion scans, some residual artifacts were observed after motion correction had been applied. It has been seen that these artifacts were due to data insufficiency. These fast massive phantom motions are not clinically expected in human scans.

The raw data of fifteen anonymized patients that moved during head CT scans were collected. Each patient scan was reconstructed using fully automated data-driven 3D iterative image reconstruction with motion compensation. The image data sets were independently assessed by two blinded radiologists and scored on a 4-point scale.

The method performed well even for relatively large patient motions. With data-driven motion estimation and correction, 65% of the patient scans became dramatically better, 14% of the scans much better, 11% negligibly better and 5% of the scans demonstrated no improvement. It has been observed that the proposed approach usually worked well when the amplitude of the rotations was less than 10^{o} and the amplitude of the translations was less than 30 mm, which in our opinion are unlikely to be exceeded in most clinical scans. However, we observed that it did not achieve motion-free images in cases of very severe motion.

In the few patient scan after MC, it was observed that some scans still have residual motion artifacts. To make motion correction robust, it is intended to investigate each shortfall that has a significant impact on ME and MC. After numerous studies, it was identified that smoothing kernel (SK) length, projection tolerance (PT) and angle rebin (AR) can affect the performance of the algorithm. The patient's scans with residual artifacts were reconstructed using various smoothing kernel (SK) lengths, projection tolerance (PT), and angle rebin (AR) to remove residual motion artifacts (MA) in head CT. All reconstructed MC images were scored. The SK length, PT, and AR have a significant impact on ME, and MC. The SK 60, PT 0.001, and AR 8 generate satisfactory artifact-free images. The mean reconstruction score (MRS) for SK 60, AR 8 were found statistically significant ($p < 0.05$) as compared with SK 120, SK 230, and SK 320 and AR 16, AR 32, respectively. Although, MRS for PT 0.001 not providing statistically significant differences ($p > 0.05$) from PT 0.0015, PT 0.0018, PT 0.0025, and PT 0.005 respectively.

Furthermore, we also performed MC for head movement during the CT part of the scan of the brain PET/CT and examined its significance for final image reconstruction. A series of PET/CT scans of Hoffman brain phantom filled with fluorodeoxyglucose (^{18}F-FDG) were acquired using mCT Siemens Biograph PET/CT scanner. The phantom was acquired with a variety of

movements during the CT part of the acquisition, to simulate patient movements, but the phantom remained stationary during the PET scan. Each motion corrupted CT scan was reconstructed using fully automated 3D iterative data-driven image reconstruction with motion compensation (MC) to remove motion artifacts and afterward an attenuation map was generated from this MC CT. The PET raw data was reconstructed offline using the JSrecon algorithm with an attenuation map from motion-corrected CT and compared with the PET scan reconstructed with an attenuation map from motion-corrupted CT. The data-driven motion compensation approach was also implemented on patients presenting head movement during CT part of brain PET/CT scan. All reconstructed images were independently assessed for qualitative analysis and the scenium analysis was performed for quantitative analysis. The reconstructed PET images of 10 basic brain regions using both nMC-PET and MC-PET were analyzed and the results showed that the SUVmean of all brain regions in nMC-PET were significantly higher than those in MC-PET. The 3D-standard surface projection (3D-SSP) Z score was evaluated on both nMC-PET and MC-PET. The 3D-SSP method compares the data from the individual to a database of healthy controls by defining a large number of points on a spatially normalized brain surface. With the little head motion, motion correction had only a slight impact on the Z score image in qualitative terms.

The data-driven ME and MC approach is based on measured raw data and successfully removed motion artifacts in head CT scans for a variety of rigid human head movements in clinical scans. Furthermore, it can be easily implemented to correct motion artifacts in clinical head helical CT scans as no further measurements are needed, and decrease the number of repeat scans. We conclude that the methods developed can provide accurate and artifact-free MC images with most types of head motion likely to be encountered in CT imaging, provided that the motion can be accurately determined. The data-driven iterative motion compensation approach for head CT significantly increases the quantitative and qualitative accuracy of the PET/CT brain image affected by patient movement. The method could be applied to both stand-alone helical CT scans and the CT component of hybrid imaging systems such as PET/CT and SPECT/CT.

Zusammenfassung

Die Computertomographie (CT) hat sich aufgrund ihrer Genauigkeit, Zuverlässigkeit, Sicherheit und breiten Verfügbarkeit zur diagnostischen Methode der Wahl bei Kopftraumata entwickelt. Die CT-Untersuchung des Kopfes wird in der Regel zur Erkennung von Infarkten, Verkalkungen, Tumoren, Knochentraumata und Blutungen eingesetzt.

Die Bewegungskorrektur (MC) ist bei der CT-Bildgebung von allgemeinem Interesse. Es gibt zwei Kategorien von Bewegungskorrekturverfahren. Die erste Gruppe erfordert Bewegungsinformationen und besteht aus Verfahren zur Bewegungserfassung und zum Bewegungsausgleich. Bei der Bewegungserfassung werden die Bewegungsinformationen aus Referenzbildern, Surrogatsignalen oder den Daten selbst abgeleitet. Die Bewegungskompensation gleicht die Bewegung während eines Rekonstruktionsprozesses aus. Die zweite Gruppe basiert auf Bildverarbeitungsverfahren und korrigiert die Bewegung ohne vorherige Kenntnis der Bewegung. Je nachdem, welche Vorabinformationen verfügbar sind, kann man den geeigneten Ansatz für die Bewegungskorrektur wählen. Ein Prototyp einer CT-Bewegungskorrekturmethode wurde von der Universität Sydney zur Verfügung gestellt. Die Technik basiert auf der starren Bewegung der helikalen Kopf-CT-Scans und benötigt nur die gemessenen Daten als verfügbare Informationen. Eine 3D-Registrierung des Objekts zu jeder 2D-Ansicht wurde einzeln durchgeführt, um die position des Objekts für jede erfasste CT-Ansicht zu schätzen. Die anfängliche grobe Schätzung des 3D-Objekts wird mit einer vorläufigen Rekonstruktion erreicht, ohne dass eine Bewegungskompensation mit dieser zwischenzeitlich geschätzten Bewegung erfolgt. Die Bewegung und das rekonstruierte Bild können in einem Mehrfachauflösungsschema abwechselnd aktualisiert werden, bis eine optimale Bewegungsschätzung gefunden ist. Der endgültige Ausgleich kann in einem Rekonstruktionsprozess mit Feinauflösung und Beschleunigung erfolgen

Ziel der Studie war es, den datengesteuerten iterativen 3D-Bewegungsschätzungs- (ME) und Bewegungskompensationsalgorithmus an einem Phantom sowie an klinischen Studien mit Kopfbewegungen während eines Computertomographie-Scans (CT) zu validieren und den datengesteuerten iterativen 3D-Algorithmus für eine robuste Anwendung zu optimieren.

Das Hoffman-3D-Gehirnphantom ermöglicht eine quantitative und qualitative Untersuchung der dreidimensionalen Effekte von Streuung und Dämpfung ähnlich dem menschlichen Gehirn. Das mit Wasser gefüllte Hoffman-Gehirnphantom wurde mit Siemens Biograph mCT-Scannern mit 128 Schichten (Siemens Medical Solutions USA, Inc., Malvern, PA) im Rahmen einer Routine-Kopf-CT aufgenommen. Ein stationärer Helical-CT-Referenzscan

(Goldstandard) des Phantoms wurde aufgenommen, danach wurde eine Reihe von CT-Scans mit einer Vielzahl von Bewegungen durchgeführt. Die Auswirkungen von MC auf die Phantom-CT-Scans wurden durch den Vergleich der stationären Goldstandard-Phantombilder mit den entsprechenden unkorrigierten und MC-Bildern bewertet. Die Phantomaufnahmen mit geringer bis mittlerer Bewegung wurden ohne Artefakte rekonstruiert, aber bei Aufnahmen mit schneller Bewegung wurden nach der Bewegungskorrektur einige Restartefakte beobachtet. Es hat sich gezeigt, dass diese Artefakte auf unzureichende Daten zurückzuführen waren. Diese schnellen massiven Bewegungen sind klinisch bei Scans in der Humanmedizin nicht zu erwarten.

Die Rohdaten von fünfzehn anonymisierten Patienten, die sich während der Kopf-CT-Scans bewegten, wurden gesammelt. Jeder Patientenscan wurde mit einer vollautomatischen datengesteuerten iterativen 3D-Bildrekonstruktion mit Bewegungskompensation rekonstruiert. Die Bilddatensätze wurden unabhängig voneinander von zwei verblindeten Radiologen beurteilt und auf einer 4-Punkte-Skala bewertet.

Die Methode schnitt selbst bei relativ großen Patientenbewegungen gut ab. Mit der datengesteuerten Bewegungsschätzung und korrektur wurden 65% der Patientenscans dramatisch besser, 14% der Scans viel besser, 11% vernachlässigbar besser und 5% der Scans zeigten keine Verbesserung. Es wurde festgestellt, dass der vorgeschlagene Ansatz in der Regel gut funktionierte, wenn die Amplitude der Rotationen weniger als 10^{o} und die Amplitude der Translationen weniger als 30 mm betrug, was unserer Meinung nach bei den meisten klinischen Scans kaum überschritten wird. Wir stellten jedoch fest, dass bei sehr starken Bewegungen keine bewegungsfreien Bilder erzielt werden konnten.

Bei wenigen Patienten-Scans wurde nach der MC festgestellt, dass einige Scans noch Restbewegungsartefakte aufwiesen. Um die Bewegungskorrektur robust zu machen, soll jeder Mangel untersucht werden, der einen wesentlichen Einfluss auf ME und MC hat. Nach zahlreichen Studien wurde festgestellt, dass die Länge des Glättungskerns (SK), die Projektionstoleranz (PT) und der angle rebin (AR) die Leistung des Algorithmus beeinträchtigen können. Die Aufnahmen des Patienten mit Restartefakten wurden unter Verwendung verschiedener Glättungskernlängen (SK), Projektionstoleranz (PT) und angle rebin (AR) rekonstruiert, um Restbewegungsartefakte (MA) in der Kopf-CT zu entfernen. Alle rekonstruierten MC-Bilder wurden ausgewertet. Die SK-Länge, PT und AR haben einen signifikanten Einfluss auf ME, und MC. die SK 60, PT 0,001, und AR 8 erzeugen zufriedenstellende artefaktfreie Bilder. Der mittlere Rekonstruktionswert (MRS) für SK 60 und

AR 8 wurde als statistisch signifikant ($p < 0,05$) im Vergleich zu SK 120, SK 230 und SK 320 bzw. AR 16 und AR 32 eingestuft. Obwohl die MRS für PT 0,001 keine statistisch signifikanten Unterschiede ($p > 0,05$) zu PT 0,0015, PT 0,0018, PT 0,0025 bzw. PT 0,005 ergab.

Darüber hinaus haben wir auch MC für Kopfbewegungen während des CT-Teils des PET/CT-Scans des Gehirns durchgeführt und deren Bedeutung für die endgültige Bildrekonstruktion untersucht. Eine Reihe von PET/CT-Scans des Hoffman-Gehirnphantoms, das mit Fluordesoxyglukose (^{18}FDG) gefüllt war, wurde mit dem mCT Siemens Biograph PET/CT-Scanner aufgenommen. Das Phantom wurde während des CT-Teils der Aufnahme mit einer Vielzahl von Bewegungen erfasst, um die Bewegungen des Patienten zu simulieren, aber das Phantom blieb während des PET-Scans stationär. Jeder bewegungsgestörte CT-Scan wurde mit Hilfe einer vollautomatischen, iterativen 3D-Bildrekonstruktion mit Bewegungskompensation (MC) rekonstruiert, um Bewegungsartefakte zu entfernen, und anschließend wurde aus diesem MC-CT eine Abschwächungskarte erstellt. Die PET-Rohdaten wurden offline mit dem JSrecon-Algorithmus mit der Abschwächungskarte aus der bewegungskorrigierten CT rekonstruiert und mit dem PET-Scan verglichen, der mit der Abschwächungskarte aus der bewegungsverfälschten CT rekonstruiert wurde. Der datengesteuerte Ansatz zur Bewegungskompensation wurde auch bei Patienten mit Kopfbewegungen während des CT-Teils der PET/CT-Untersuchung des Gehirns angewandt. Alle rekonstruierten Bilder wurden unabhängig voneinander für die qualitative Analyse bewertet, und die Sceniumanalyse wurde für die quantitative Analyse durchgeführt. Alle rekonstruierten Bilder wurden unabhängig voneinander für die qualitative Analyse bewertet und die Scenium-Analyse wurde für die quantitative Analyse durchgeführt. Die rekonstruierten PET-Bilder von 10 grundlegenden Hirnregionen sowohl mit nMC-PET als auch mit MC-PET wurden analysiert, und die Ergebnisse zeigten, dass der SUV-Mittelwert aller Hirnregionen bei nMC-PET signifikant höher war als bei MC-PET. Der Z-Score der 3D-standard surface projection (3D-SSP) wurde sowohl für nMC-PET als auch für MC-PET ausgewertet. Bei der 3D-SSP-Methode werden die Daten der Person mit einer Datenbank gesunder Kontrollen verglichen, indem eine große Anzahl von Punkten auf einer räumlich normalisierten Hirnoberfläche definiert wird. Bei der geringen Kopfbewegung hatte die Bewegungskorrektur nur einen geringen Einfluss auf das Z-Score-Bild in qualitativer Hinsicht.

Der datengesteuerte ME- und MC-Ansatz basiert auf gemessenen Rohdaten und entfernte erfolgreich Bewegungsartefakte in Kopf-CT-Scans für eine Vielzahl von starren menschlichen Kopfbewegungen in klinischen Scans. Darüber hinaus kann er leicht zur Korrektur von

Bewegungsartefakten in klinischen Helical-CT-Scans des Kopfes eingesetzt werden, da keine weiteren Messungen erforderlich sind und die Anzahl der Wiederholungsscans verringert werden kann. Wir kommen zu dem Schluss, dass die entwickelten Methoden genaue und artefaktfreie MC-Bilder bei den meisten Arten von Kopfbewegungen, die in der CT-Bildgebung vorkommen, liefern können, vorausgesetzt, die Bewegung kann genau bestimmt werden. Die datengesteuerte iterative Bewegungskompensation für die Kopf-CT erhöht die quantitative und qualitative Genauigkeit des PET/CT-Gehirnbildes, das durch Patientenbewegungen beeinflusst wird, erheblich.

Dedication

This work is dedicated to my beloved husband without his constant support this work was not possible and to my lovely kids Emaan, Zuhair, they sacrifice during this work.

Contents

Chapter 1. Aims and objective 1
1.1 Motivation and aims of the research 1
1.2 Significance of study 3
Chapter 2. Introduction 4
2.1 X-ray computed tomography 4
2.2 Historical overview 4
2.3 X-rays production 4
2.4 Photon interaction mechanism with matter 5
2.4.1 Rayleigh scattering 6
2.4.2 The photoelectric effect 6
2.4.3 Compton scattering 6
2.4.4 Pair production 7
2.5 X-ray detection 9
2.6 CT history geometric expansion 11
2.6.1 The generations of CT scanners 11
2.7 Hybrid imaging 16
2.7.1 Significance of hybrid imaging 17
2.8 PET/CT system 17
2.8.1 Basic principles of PET imaging 18
2.8.2 PET detectors 20
2.8.3 PET data corrections 23
2.9 CT based attenuation correction 26
Chapter 3. Tomographic Reconstruction Methods 29
3.1 Image reconstruction 29
3.1.1 Projection 29

3.1.2 Back projection 31
3.2 Reconstruction algorithms 31
3.2.1 Analytic reconstruction 32
3.2.2 Iterative reconstruction 33
3.3 Image artifacts in CT 36
3.4 Motion estimation 38
3.4.1 Non-rigid motion estimation 38
3.4.2 Rigid motion estimation 38
3.5 Motion compensation 40
3.5.1 Joint motion estimation and compensation 40
3.6 Image-processing based methods 40
Chapter 4. 3D Iterative Data-Driven Motion Correction Algorithm 42
4.1 Motion estimation and compensation method 42
4.2 Motion correction method 43
4.2.1 Motion update 44
4.2.2 Image update 48
4.2.3 Multi-resolution alternate update scheme 48
4.2.4 Final reconstruction 48
4.2.5 Data-sufficiency 49
Chapter 5. Validation of 3D iterative data-driven motion correction algorithm 50
5.1 Introduction 50
5.2 Phantom studies 51
5.3 Hoffman brain phantom 52
5.4 Clinical studies 54
5.4.1 Data collection 54
5.4.2 Motion estimation and compensation scheme 55
5.4.3 Scoring of images 57

5.5 Results 58
5.6 Discussion 60
Chapter 6. Optimization 64
6.1 Introduction 64
6.2 Material and methods 65
6.3 Smoothing kernel (SK) 65
6.4 Projection tolerance (PT) 65
6.5 Angle rebin (AR) 66
6.6 Scoring of images 66
6.6.1 Statistical analysis 66
6.7 Results 66
6.7.1 Smoothing kernel 67
6.7.2 Projection tolerance 70
6.7.3 Angle rebin 76
6.8 Discussion 77
Chapter 7. The Effect of Head Movement During CT on Hybrid PET/CT Brain Scan 80
7.1 Introduction: 80
7.2 Materials and methods 81
7.3 Results 83
7.4 Patient scan 85
7.5 Quantitative Scenium analysis 88
7.6 Discussion 93
Chapter 8. Conclusions and Future Work 96
References 98

List of Tables

Table 2.1: Detector crystal properties 22
Table 5.1: Acquisition and reconstruction protocol for Hoffman brain phantom 53
Table 6.1: Mean number of iterations for different PT values at each resolution level 72
Table 7.1: Scenium analysis nMC-PET 91
Table 7.2: Scenium analysis MC-PET 92

List of Figures

Figure 2.1: Schematic image of x-ray production (radiologycafe.com). 4
Figure 2.2: A typical x-ray spectrum produced by an X-ray tube (physicsopenlab.org). 5
Figure 2.3: Schematic representation of photoelectric effect (Cherry et al., 2012). 6
Figure 2.4: Schematic demonstration of Compton scattering (Cherry et al., 2012). 7
Figure 2.5: Schematic demonstration of pair production, energy of incident photon converted into an electron and positron. The position at the end of its range undergoes an annihilation process emitting two 511 keV electrons (Cherry et al., 2012). 8
Figure 2.6: The most probable interactions versus photon energy for elements of different atomic numbers (Cherry et. al., 2012). 9
Figure 2.7: (a) Indirect conversion detector used in clinical multi-row CT and some cone-beam CT. (b) direct conversion detector used in some cone-beam CT (Sun, 2018). 9
Figure 2.8: Photon counting detector output signals are grouped in different bins according to photon energies (Sun, 2018). 10
Figure 2.9: Schematic of four generations of CT scanner from a-d. 12
Figure 2.10: Axial & helical CT scanning. 13
Figure 2.11: Single slice scanner and multi-slice scanner (Rydberg et al., 2000). 14
Figure 2.12: Effects of a different pitch for helical CT scan. 14
Figure 2.13: Schematic of cone-beam CT (Reiser et at., 2009). 15
Figure 2.14: Schematic of fan-beam CT (Reiser et at., 2009). 15
Figure 2.15: Dual-energy CT scan (courtesy Siemens). 16
Figure 2.16: Schematic of PET/CT system 18
Figure 2.17: Line of response and true coincidence events. 19
Figure 2.18: Single event due to non-annihilation events detected at two detectors with the timing and energy window of the system. 20
Figure 3.1: A pencil beam transverse the object and the line integral along the beam path provide one point of the profile $P(r, \theta)$. 30
Figure 3.2: Back Projection. 31
Figure 3.3: Reconstruction with filtered back projection (Gonzalez et al., 2018). 34
Figure 3.4: Schematic of an iterative reconstruction method. 34
Figure 3.5: Schematic of OSEM reconstruction method (Saha et al., 2016). 36

Figure 3.6: Artifacts in CT (a) patient motion, (b) Noise, (c) ring artifact, (d) streak artifact, (e) streak artifact due to photon starvation, (f) metal artifact (Boas et al., 2012). 37
Figure 4.1: The scanner and detector scheme used for motion estimation and compensation (Sun et al., 2016). 42
Figure 4.2: Schematic of motion estimation technique. μ is the update of the attenuation image, *s* is the update of the rigid transform, *n* is the iteration number (Sun et al., 2015). 45
Figure 4.3: The impact of object rotation and translation parallel to the detector can be better approximated in the detector coordinate system as translation and rotation of the projection. m is the magnification factor from the object to the detector. For simplification, the curvature of the detector is omitted (Sun et al., 2015). 47
Figure 5.1: Hoffman brain phantom. 52
Figure 5.2: Hoffman brain phantom acquisition on Biograph mCT. 52
Figure 5.3: Hoffman brain phantom analysis (Kim et al., 2016). The motion-induced phantom scans were reconstructed with and without a motion correction and compared with a reconstructed stationary phantom scan. 54
Figure 5.4: ROI for removal of patient headrest and couch from raw data before motion estimation. 57
Figure 5.5: Motion of Hoffman brain phantom rotation motion (^{o}) and translation motion (mm) of the phantom in CT isocentre coordinates, concerning its pose at the start of the scan. This figure explains the nature of the motion, which is intricate motion in all six DoF, (a) slight motion, (b) moderate motion, (c) fast motion. 59
Figure 5.6: Comparison of axial reconstructed slices from the moving phantom uncorrected and motion-corrected, (a) stationary phantom, (b) slight motion, (c) moderate motion, (d-e) fast motion. 60
Figure 5.7: A 58-year-old man's head CT scan, two different CT scan slices are shown, (a-b) the top row is original scan slices with motion, bottom row is motion-corrected. 61
Figure 5.8: A male patient sneeze during a CT scan a) uncorrected axial slices and b) motion-corrected slices reveal the improvement in image quality. 62
Figure 5.9: Selected transaxial, sagittal, and coronal planes, with and without compensation for residual motion. Top: original image; bottom: motion-corrected image 63
Figure 6.1: (a) Image reconstructed with Siemens software without motion correction, the arrow pointing ghosting, (b) image reconstructed with 3D iterative data-driven motion correction approach. 67

Figure 6.2: (a) Real image reconstructed with Siemens software without motion correction, the arrow pointing ghosting (skull to appear in 3 locations), (b) iterative image reconstruction with data-driven motion correction using smoothing kernel 60, (c-e) iterative image reconstruction with data-driven using SK120, SK 230, and SK 320, respectively. Ghosting was almost completely corrected in (b), but the correction was less complete in (c-e). 68
Figure 6.3: (a) Real image reconstructed with Siemens software without motion-correction, the arrow pointing ghosting (skull to appear in multiple locations), (b) iterative image reconstruction with data-driven motion correction using smoothing kernel 60, (c-e) iterative image reconstruction with data-driven using SK 120, SK 230, and SK 320, respectively. MA was almost completely corrected in (b), but the correction was less complete in (c-e). 68
Figure 6.4: Column (a) various patient scans demonstrating MA with vendor reconstruction without motion correction, column (b-e) iterative image reconstruction with data-driven motion correction SK 60, SK 120, SK 230, and SK 320 respectively, MA was nearly completely corrected in column (b). 69
Figure 6.5: Comparison of different smoothing kernels for three rotation parameters (Rx, Ry, Rz) and three translation parameters (Tx, Ty, Tz). 71
Figure 6.6: Number of iterations and projection error for different SK values, PE drops as the number of iterations increases. 72
Figure 6.7: (a) Image reconstruction obtained using Siemens software without motion correction, the arrow pointing to MA, (b-g) image reconstruction with data-driven using smoothing kernel 60 and PT set to 0.001, 0.005, 0.0012, 0.0015, 0.0018, and PT 0.0025, respectively. MA was completely corrected in (b), but the correction was less complete in (c-g). 73
Figure 6.8: (a) Image reconstruction by using Siemens software without motion correction, (b) image reconstruction with data-driven using SK 60 and PT 0.001 completely corrected MA, (c-g) image reconstruction with data-driven using SK 60 and PT 0.005, PT 0.0012, PT 0.0015, PT 0.0018, and PT 0.0025 respectively. 73
Figure 6.9: Comparison of three rotation parameters (Rx, Ry, Rz) and three translation parameters (Tx, Ty, Tz) for different projection tolerance. 75
Figure 6.10: Number of iterations and projection error for different projection tolerance. 75
Figure 6.11: Impact of extended iteration with constant smoothing kernel, (a) real image without motion correction, (b) SK 60/0.0001, (c) SK 60/0.001, (d) SK 60/0.0015. 76
Figure 6.12: Column (a) Real image reconstruction with Siemens software without motion correction, column (b) iterative image reconstruction with data-driven using smoothing kernel

SK60 / PT 0.001 / AR 8 removed ghosting, column (c, d) SK 60 / PT 0.001 / AR 16 and SK 60 / PT 0.001 / AR 32 respectively still have the residual artifact. 77
Figure 7.1: Hoffman brain phantom acquisition on Biograph mCT. 82
Figure 7.2: Top: phantom scan with couch segment, bottom: couch segments were deleted from the raw data before reconstruction. 83
Figure 7.3: CT scan of a) stationary phantom, b) moving phantom, c) motion-corrected. 84
Figure 7.4: Axial view of an ^{18}F-FDG-PET scan of (a) stationary phantom, (b) reconstructed using a CT image with motion artifacts (nMC), (c) reconstructed using a motion-corrected CT image for attenuation and scatter correction (MC), (d) The profile along the lines for stationary, nMC and MC PET images. 84
Figure 7.5: (a) CT image reconstructed by vendor software without motion-correction, (b) motion corrected reconstruction and ghost artifact removed after motion-correction, (c) absolute difference between a and b image. 85
Figure: 7.6 (a) CT image reconstructed by vendor software without motion-correction, (b) PET image reconstructed using a CT image with motion artifacts (nMC), (c) CT image with motion-corrected reconstruction and artifact removed after motion-correction, (d) image reconstructed using a motion-corrected CT image for attenuation and scatter correction. 86
Figure 7.7: (a) PET image using a CT image with motion artifacts (nMC), (b) PET image reconstructed using a motion-corrected CT image for attenuation and scatter correction (MC), (c) |Difference| bewteen a and b image. 86
Figure 7.8 (a) CT image reconstructed by vendor software without motion-correction, (b) PET image reconstructed using a CT image with motion artifacts (nMC), (c) CT image with motion corrected reconstruction and artifact removed after motion correction, (d) image reconstructed using a motion corrected CT image for attenuation and scatter correction (MC). 87
Figure 7.9: (a) PET (nMC), (b) corrected PET for attenuation and scatter correction (MC), (c) "|Difference|". 88
Figure 7.10: (a) Axial, coronal and sagital PET (nMC), (b) axial, coronal and sagital PET (MC), (c) axial, coronal and sagital PET/CT (nMC), (d) axial, coronal and sagital PET/CT(MC). 89
Figure 7.11: (a) Axial, coronal, and sagittal PET views with attenuation map obtained with nMC-CT attenuation correction, (b) scenium analysis nMC-PET, (c) axial, coronal, and sagittal PET views reconstructed with MC-CT, (d) scenium analysis MC-PET (arrows pointing the differences). 90
Figure 7.12: Z score image of 3D-SSP analysis global normalization nMC-PET. 95
Figure 7.13: Z score image of 3D-SSP analysis global normalization MC- PET. 95

Chapter 1. Aims and objective

1.1 Motivation and aims of the research

The most essential and common diagnostic technique in medicine is X-ray computed tomography (CT). CT is the most common medical imaging, in the United States alone, 70 million scans are performed each year (Brenner et al., 2007). In various medical diagnoses, CT has a vital role, including traumatology, cardiology, vascular radiology, oncology, interventional radiology (Dance et al., 2014) hybrid imaging (Beyer et al., 2000), and radiotherapy planning (Jaffray et al., 2012, Ferrando et al., 2015). CT scanning is commonly available, cost-effective, and provides higher sensitivity for the evaluation of skull fracture, calcification, and acute hemorrhage (Raj at el., 2014).

Generally, CT motion artifacts are due to voluntary and involuntary actions like head motion, cardiac motion, and respiratory motion (Popilock et al., 2008, Yazdi et al., 2008). Head motion is also very frequently noticed in CT brain perfusion imaging of acute ischemic stroke patients (Fahmi et al., 2014). Moreover, severely injured patients or small children often move during scanning, thus generating motion artifacts (Barrett et al., 2004). Children must often be anesthetized, which is accompanied by some risks (Davidson et al., 2006). If the patient moves during the scan the motion artifacts can cause false diagnosis or in severe cases deliver distorted images that are inappropriate for diagnosis (Edlow et al., 2000). For these patients, scanning needs to be repeated resulting in a high undesirable radiation burden to the patient (Boone et al., 2012). The ability to compensate for head motion would reduce the need for a repeat scan and deliver artifact-free images in CT, PET/CT, and SPECT/CT, as these hybrid imaging techniques are dependent on the CT image for accurate anatomical localization and functional data for attenuation correction (Akamatsu et al., 2014, Ay et al., 2007). Moreover, effective head motion compensation methods are available for SPECT, PET, and MRI, but there is a lack of equivalent methods for CT, particularly for rigid motion.

Motion artifacts might be reduced by faster scanning and employing immobilization devices (Beyer et al., 2005), and using sedation for pediatric patients or general anesthesia (Wachtel et al., 2009). However, each of these approaches has limitations, such as fast imaging protocols might compromise on image quality and anesthetics in children can have unfavorable side effects (i.e., respiratory depression, oxygen desaturation, and hypoxemia) (Malviya et al., 2000, Kaste et al., 2004). In some cases, anesthesia does not entirely avoid movement and requires more staff and other resources. It has also been demonstrated that in helical CT scans for the

head and neck, immobilization devices do not eliminate patient movement (Wagner et al., 2003). Therefore, there is an urgent need to mitigate motion artifacts by retrospective motion correction method.

Motion correction methods can be classified into two categories. The first group requires the motion acquisition data, such as surrogate signals or reference images to derive motion information, and motion is compensated during the reconstruction process. The second method is to compensate for motion without prior information about the motion using image-processing techniques. Rigid motion correction in helical CT scan is complicated as the object is continually truncated from the axial side which provides limited data to restore the consistency in projections (Kim et al., 2013) comparatively, a small number of studies already performed motion correction in helical CT scanning, and a few of these studies need supplementary measurement to acquire the motion information (Kyme et al., 2014, Bhowmik et al., 2012, Sisniega et al., 2017, Kim et al., 2015, Kim et al., 2016, Man et al., 2004).

In the present study, a data-driven fully 3D automatic reconstruction approach has been used to minimize motion artifacts in helical CT imaging (Sun et al., 2016). The proposed motion estimation, correlation, and compensation technique only require the measured raw data and the iterative reconstruction process to estimate the correction required. The study aimed to validate the data-driven 3D iterative motion estimation (ME) and motion compensation (MC) algorithm on scans with head movements during computed tomography (CT) and to optimize it for robust application. The implementation and optimization of a data-driven 3D iterative motion correction algorithm will be performed on brain phantom as well as patient scans to correct motion artifacts in human head CT.

This work will involve the development of methods for:

1. Validation of data-driven motion correction algorithm using moving phantoms studies on the helical CT systems.
2. The evaluation goal is to prove that the method is robust.
3. The optimitation of motion estimation and reconstruction in the 3D iterative data-driven motion reconstruction method.
4. To evaluate the effect of CT image motion correction on PET image in hybrid PET/CT brain imaging.

1.2 Significance of study

Motion is an important artifact in patient imaging that causes a reduction in the qualitative and the quantitative accuracy of the image. Primarily there are no motion correction techniques available for commercial CT scanners. Furthermore, this technique has primary importance for the patient all over the world and need immediate attention. The ability to compensate for head motion would alleviate the need for a repeat scan and deliver artifact-free images in CT and PET/CT. Moreover, the development of new techniques for motion correction in CT will be beneficial for patients as they can save their time, money, and undesired radiation exposure due to repeat CT scans.

Chapter 2. Introduction

2.1 X-ray computed tomography

X-ray computed tomography is a noninvasive imaging technique that provides a three-dimensional view of anatomical details of the body. The first x-ray CT was introduced in 1971, with continual development CT scan became an essential diagnostic technique in medicine (Cherry et al., 2012). CT scanning is commonly available, cost-effective, and has a wide range of applications in hybrid imaging, traumatology, cardiology, vascular radiology, oncology, and interventional radiology. The number of CT examinations is growing exponentially all over the world.

2.2 Historical overview

2.3 X-rays production

The x-ray tube is a vacuum tube consisting of a tube housing, a cathode (source of the electron), an anode (target) made up of high Z material, and a focusing cup to control the focal spot size as shown in figure 2.1. When the cathode is heated electrons are generated by thermionic emission. These electrons are accelerated and focused on the target by applying a potential difference between an anode and a cathode. The highest x-ray energy is equal to the peak voltage applied (20 to 150 kVp). A metal filter is used to remove low-energy x-ray before reaching the patient. On the interaction of the electron with the target material, bremsstrahlung and characteristic x-rays are produced.

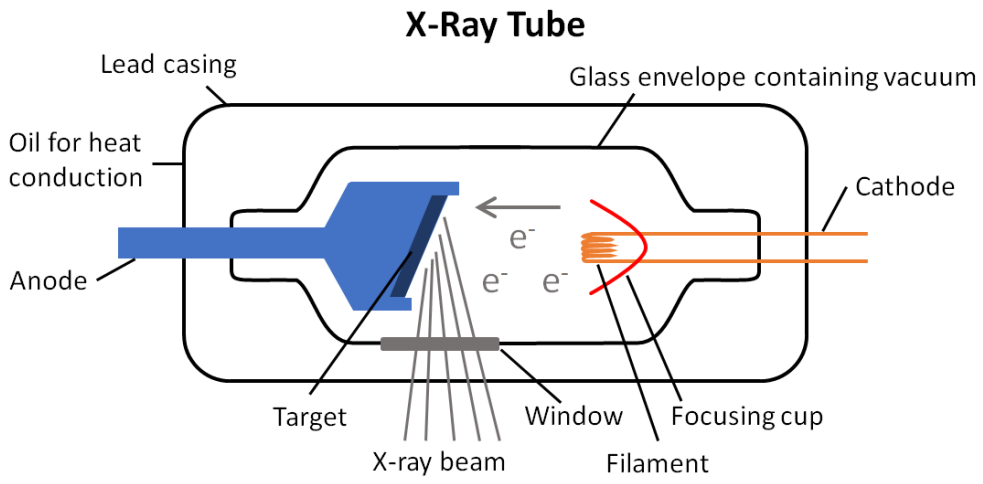

Figure 2.1: Schematic image of x-ray production (radiologycafe.com).

(a) Bremsstrahlung (breaking radiation) produced from inelastic interactions of the high-speed electron and the nucleus of the atom as shown in figure 2.2. When an energetic electron passes close to the nucleus of the atom the attractive coulomb's forces deaccelerate the electron and produce bremsstrahlung. These radiations cover the entire energy range of the spectrum and the total energy of the radiation depends on incident kinetic energy and the amount of energy is given off during the interaction. The target material´s Z^2 determines the liklihood of bremsstrahlung emission.

(b) In the second type of interaction, the high-speed electron collides with one of the target atom's inner shell (K shell) electrons and ejects it. Another electron from the outer shell fills this vacancy and discrete characteristic radiation is released with its energy equal to the difference between the binding energies of two shells.

(c) In the third sort of interaction, an electron collides with a nucleus directly, converting its entire energy into x-ray radiation. The x-ray energy produced by this interaction is the x-ray spectrum's upper energy limit.

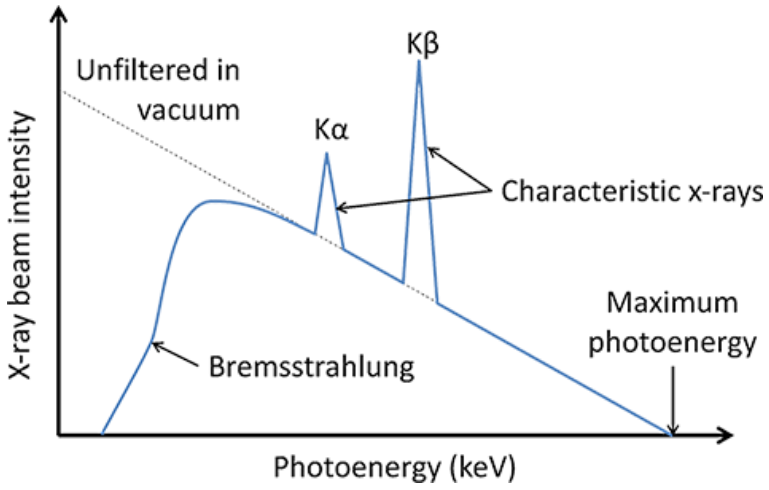

Figure 2.2: A typical x-ray spectrum produced by an X-ray tube (physicsopenlab.org).

It is noticeable that the major portion of the x-ray is produced by bremsstrahlung while the spikes represent the characteristic x-rays. The x-ray quantity is approximately proportional to $Z_{target} \times kV^2 \times mA_S$ and the quality of x-rays depends on kVp, tube filtration as well as generator waveform.

2.4 Photon interaction mechanism with matter

X-rays and gamma rays transverse through matter and transfers their energy via nine different interactions. There are four major types of interaction: Rayleigh scattering, Compton

scattering, photoelectric absorption occurs between 30 keV- 150 keV, and pair production at higher energies > 1.022 MeV. The first three play a significant role in diagnostic radiology.

2.4.1 Rayleigh scattering

When there is an interaction of a photon with an outer shell electron through a non-ionizing process, the photon is scattered without losing energy. The chance of Rayleigh scattering increases as the target material's atomic number (Z) increases and decreases as the incident photon's energy (E) increases.

2.4.2 The photoelectric effect

In this process, incident photons is being absorbed by an atom. Figure 2.3 shows a schematic example of the photoelectric effect, in which a photon is absorbed and its energy is released by an electron known as a photoelectron. The difference in energies between the incident photon and the binding energy of the electron gives the photoelectron kinetic energy. Only when the energy of incident photons surpasses the binding energy of the electron in that shell can the photoelectric effect occur. The photoelectric effect's probability is related to Z^3/E^3.

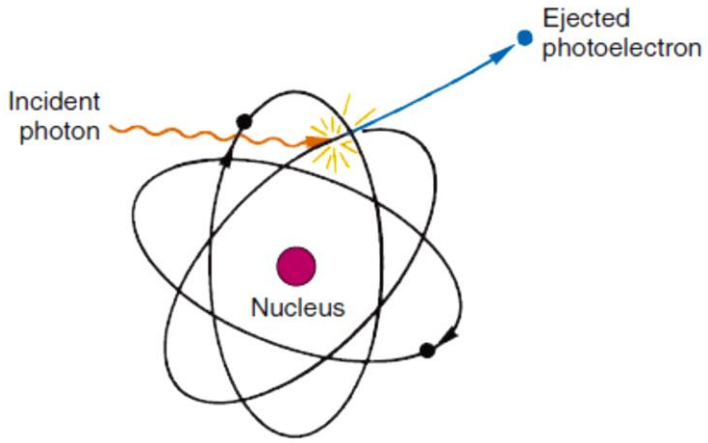

Figure 2.3: Schematic representation of photoelectric effect (Cherry et al., 2012).

2.4.3 Compton scattering

When an extremely high-energy photon collides with an atom's weakly connected outer-shell orbital electron, this interaction happens. The photon is not lost via Compton scattering; instead, it is deflected at an angle, as illustrated in figure 2.4, and only a portion of its energy is passed to the 'recoil' electron. A scattered photon and a Compton electron are created in this process. According to the conservation of energy and momentum, the energy of the scattered photon is proportional to the scattering angle.

$$E' = {}^{E}/_{[1+\alpha(1-\cos\theta)]} \qquad (2.1)$$

Where E′ is scattered and E is incident photon energies, α is E/m_oc^2 and m_oc^2 = 0.511 MeV is the rest energy of an electron. The probability of Compton scattering increases with an increase in E of the incident photon but is independent of Z of the target material.

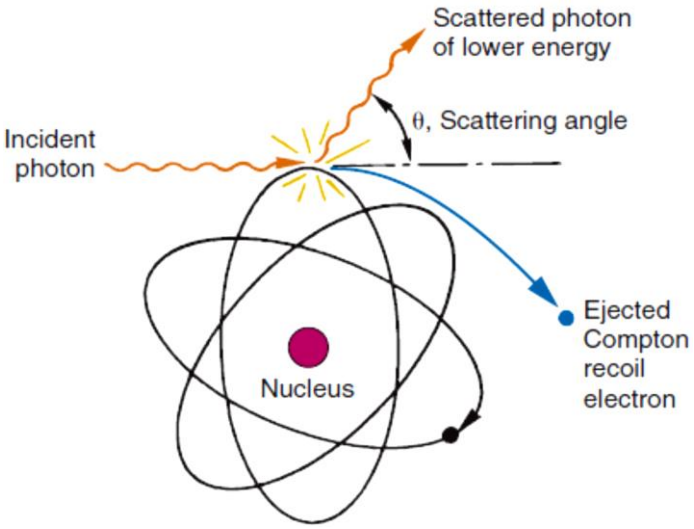

Figure 2.4: Schematic demonstration of Compton scattering (Cherry et al., 2012).

2.4.4 Pair production

A charged particle, generally an atomic nucleus, interacts with the electric field of a photon with an energy of 1.022 MeV. The photons vanished, and their energy was transformed into a pair of positrons (e^+) and electrons (e^-). The kinetic energy between the positron-electron pair is equal to the difference between incident photon energy E and the energy necessary to form the electron pair, as shown in the equation:

$$Ee^+ + Ee^- = E - 1.022\ \text{MeV} \qquad (2.2)$$

Through ionization and excitation, the positron annihilates with another neighboring electron at the end of the route, resulting in a pair of 511 keV photons traveling in opposing directions, as seen in figure 2.5. With rising E and Z^2, the likelihood of pair production rises.

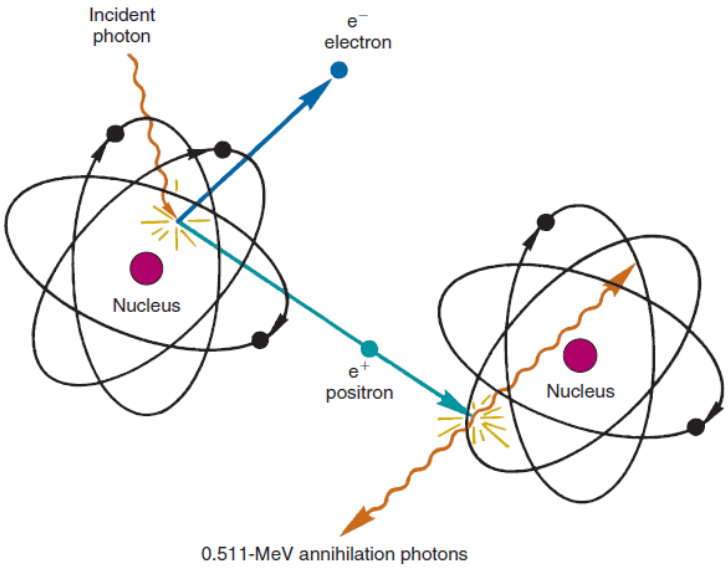

Figure 2.5: Schematic demonstration of pair production, energy of incident photon converted into an electron and positron. The position at the end of its range undergoes an annihilation process emitting two 511 keV electrons (Cherry et al., 2012).

The x-rays beam undergoes different interactions with matter, the flux of the beam reduces depending upon the composition of the material and the energy of the photon. The most probable interactions versus photon energy for elements of different atomic numbers shown in figure 2.6. For the diagnostic x-ray energies, Compton scattering and photoelectric absorption are the two most dominant interactions. The attenuation of a narrow monenergistic x-ray beam transverse through homogenous material of thickness *x* can be written as

$$I = I_o \, exp^{-\mu x} \qquad (2.3)$$

Where Io represents the initial intensity without an absorber, I represent the beam intensity after transmission through an absorber of thickness t and represent the linear attenuation coefficient. The x-ray beam is polychromatic, and the equation (2.3) can be written to represent the diversity of attenuation in biological tissues.

$$I(E) = I_o(E) exp^{-\int_{x=0}^{x=T} \mu(E,x)dx} \qquad (2.4)$$

$I_o(E)$ is x-ray spectra before attenuation and I (E) x-ray spectra after attenuation, T is the thickness of the medium, $\mu(E,x)$ is the linear attenuation coefficient.

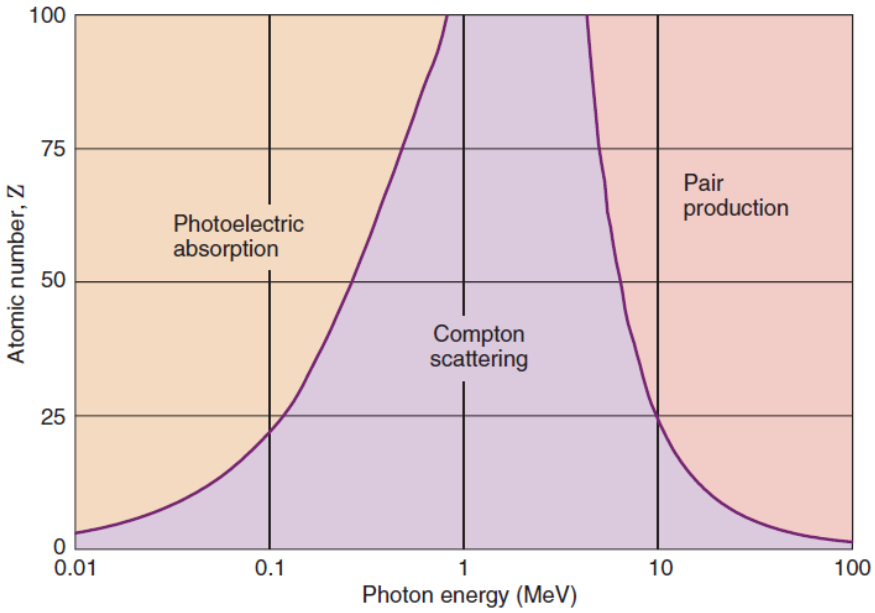

Figure 2.6: The most probable interactions versus photon energy for elements of different atomic numbers (Cherry et. al., 2012).

2.5 X-ray detection

X-ray detectors were used to measure the intensity of x-rays and were often used in the integrating current mode. The detectors' output current is proportional to the number of x-rays that impact the detector (Shefer et al., 2013). The indirect conversion approach was used to measure x-rays with a solid-state detector. The scintillator detector has a high density and atomic number, and it typically has a high x-ray absorption efficiency. A scintillator and a photodetector combine to form a solid-state CT detector. When x-rays hit the scintillator detector it converts x-rays into optical photons, a photodiode translates that optical signal into a proportional electrical signal.

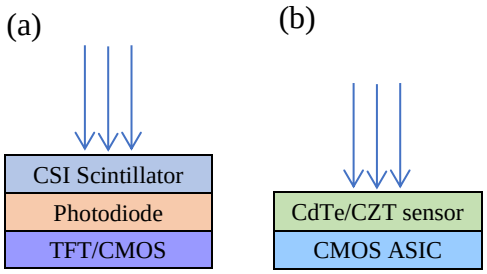

Figure 2.7: (a) Indirect conversion detector used in clinical multi-row CT and some cone-beam CT. (b) direct conversion detector used in some cone-beam CT (Sun, 2018).

Afterward, the signals are amplified and digitized to create images. Most of the cone-beam CT used these indirect conversion detectors for the measurement of x-rays, as shown in figure 2.7.

The Photon counting detectors convert x-rays to electronic signals through the direct conversion method. Moreover, it is very efficient and can detect every individual photon if the induced signal is above a threshold energy level. By comparing these pluses signal per pixel with threshold level noise can be easily filtered out. Each photon is assigned a discrete different energy bin according to its energy as illustrated in figure 2.8. The photon-counting detectors have several advantages over integrating detectors like enhanced spatial resolution, less radiation dose to the patient, better signal-to-noise ratio, are the capability of differentiating numerous contrast agents (Ji et al., 2009, Polster et al., 2016).

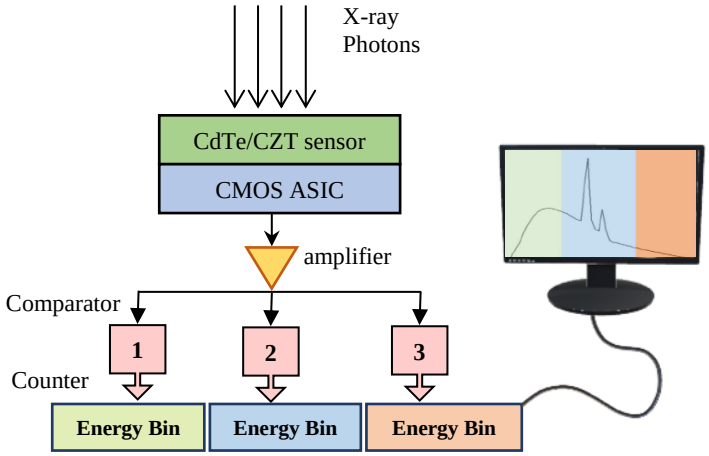

Figure 2.8: Photon counting detector output signals are grouped in different bins according to photon energies (Sun, 2018).

In modern CT scanners, two-dimensional CT detector arrays are used to acquire multiple slices simultaneously (Steve et al., 2004). The patient bed is shifted during the scan while the detector ring rotates around the patient to generate a helical route, ensuring comprehensive sampling for reconstruction. By keeping the detector size between 0.25 and 1.25 mm, high spatial resolution can be attained. The system could have 16, 32, 64, and so on rows of detectors. A number of slices equal to the number of detector rows can be acquired in a single rotation of the system. For typical x-ray energy (40-140 keV) used in CT scanners, the x-ray detectors have the maximum efficiency.

In CT reconstructed image each pixel value corresponds to the attenuation coefficient value of the tissue for that pixel. These attenuation coefficients are represented on a normalized scale in

terms of Hounsfield units (Cherry et al., 2012). This normalization generates a wide range of CT numbers -1000 to +3000, like air, water and bone have Hounsfield units of -1000, zero, and +1000 respectively. The soft tissue has CT numbers of -300 to -100 and dense bone and contrast-filled areas have a CT number of +3000. The Hounsfield units named after Sir Godfrey Hounsfield are simply scaled units of x-ray attenuation as calculated by CT.

$$\mathrm{CT}\,(x,y) = \frac{\mu(x,y) - \mu_w}{\mu_w} \times 1000 \qquad (2.5)$$

Where μ and μ_w are the attenuation coefficient of the pixel(x, y) and attenuation coefficient of water respectively.

2.6 CT history geometric expansion

2.6.1 The generations of CT scanners

The first generation was introduced by Godfrey Hounsfield (1971) for the first brain scan. It employed a pencil x-ray beam and two detectors to measure the x-ray transmission through the patient by parallel ray geometry. This geometry is very effective for scatter reduction, as the scatter deflected away from the pencil beam was not measured by detectors (Bushberg et al., 2012). The tube and detector had translated motion, the total scan time was 25-30 mins. For each angle, the x-ray tube and detector assembly translated and acquired data across the field of view and rotated to acquire for another angle, this process was repeated for all 180^o angles shown in the figure. 2.9 (a).

In the next generation (1976) narrow fan beam (10^o) and a linear array of 30 detectors were used, which significantly reduced the acquisition time. However, the procedure of data acquisition was yet based on translation and rotation movement. The x-ray source is inefficiently used in pencil beam geometry, yet it gives good rejection of x-ray scatter. In standard fan-beam scanners, scattered radiation contributes to about 5% of the signal.

The third generation of CT systems, detector array, and x-ray tube was mechanically joined, and the data acquisition was based on rotate/rotate configuration. A larger scanning area at one time was possible due to the increase in the number of detectors (more than 800) as well as fan beam angle. This configuration eliminates translation motion and offers a shorter acquisition time. The transmission measurement for two detectors can be written as (Cherry et al., 2012);

$$\ln\,(g_1 I_o / g_2 I_t) = \mu t \qquad (2.6)$$

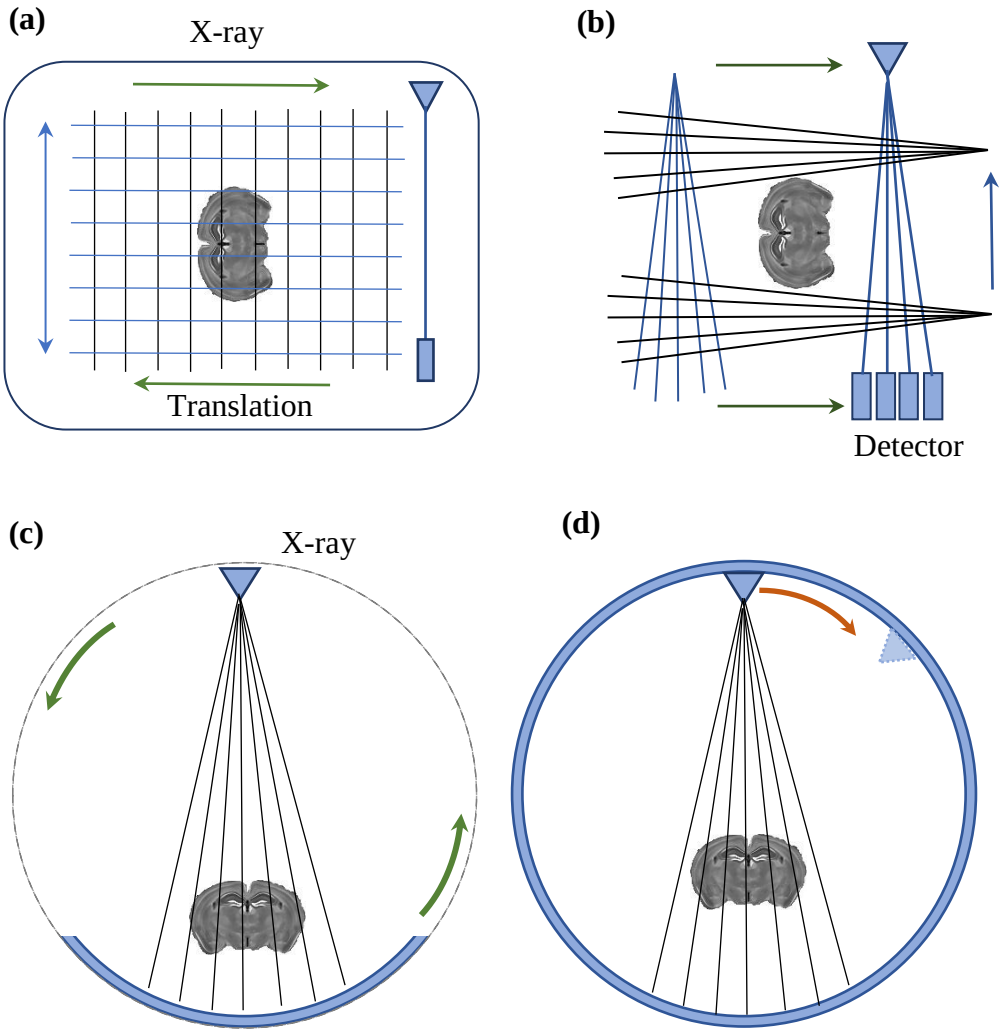

Figure 2.9: Schematic of four generations of CT scanner from a-d.

where g_1 and g_2 are the gain of two detectors if the gain of two detectors is not equal ($g_1 \neq g_2$) that affects μt and during back-projection generates ring artifacts. The ring artifact was a common problem in the third-generation scanner. To solve this problem the fourth-generation scanner was introduced.

The fourth-generation CT had a stationary/rotating configuration. In the complete circular array of stationary detectors, the x-ray tube revolves. In comparison to a third-generation CT scanner, this architecture necessitates approximately six times the number of individual detectors.

The ring artifacts were removed because each detector functions as its reference detector. Therefore, for fourth-generation scanners, equation 2.7 can be written as (Bushberg et al., 2012);

$$\ln(gI_o / gI_t) = \mu t \qquad (2.7)$$

The fifth-generation scanners were specially designed for cardiac. They were named cine CT or electron beam scanners. The cine CT had a unique design and was not using a conventional x-ray tube and detector configuration. The increase in computer storage capacity and advancement in detector technology also increased the matrix size from 80×80 to 1024×1024 for CT scans. For all generations of CT scanners mentioned above object remained stationary during 360^{o} rotation (one slice), subsequent slices were obtained by moving the table in steps. Kalender et al (1989) introduced the concept of helical CT scan after the development of slip ring technology. Slip rings are circular contact with sliding brushes that enabled the gantry to move continuously. In a helical scan, volumetric data is acquired when x-ray sources and detector rotate in a spiral path around the patient while the patient table moved at a fixed speed on the Z-axis throughout the scanning time as revealed in figure 2.10.

The clinical multi-row CT increased the axial coverage of the detector as well as the temporal resolution of CT systems by reducing CT acquisition time, hence reducing the possibility of motion artifacts. By resolving many slices, the multi-detector-row CT (MDCT) improves longitudinal resolution (slice thickness far below 1mm), achieving the goal of isotropic resolution (Cherry et al., 2015). Figure 2.11 shows how the number of detector rows increases over time and how this affects axial coverage.

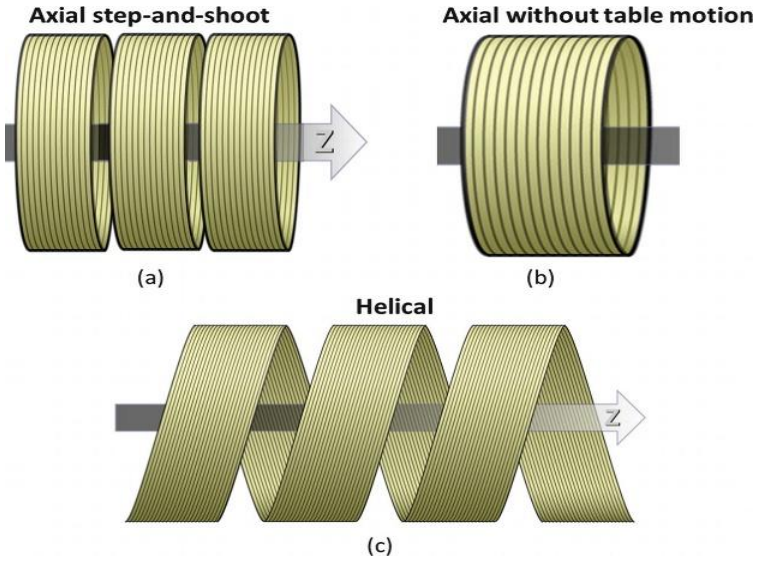

Figure 2.10: Axial & helical CT scanning.

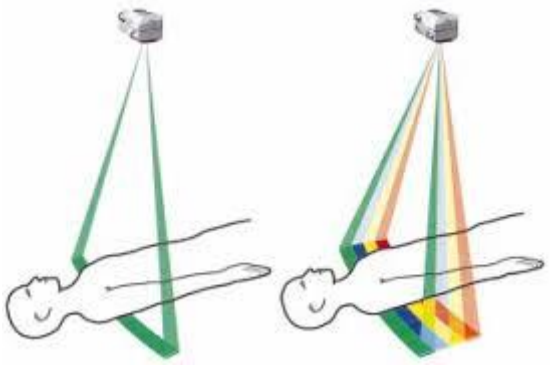

Figure 2.11: Single slice scanner and multi-slice scanner (Rydberg et al., 2000).

The detector size, not the collimator, determines the slice thickness in a multiple detector array. The pitch factor is the ratio of table distance traversed in one 360° gantry rotation by beam collimation. The effects of various pitches for a helical CT scan are shown in Figure 2.12.

A higher pitch offers faster table translation and greater volume covered per unit time, resulting in patient dose reduction but lower image quality due to sparse sampling. Single-slice CT scanners had a rotation time of 1 to 2 seconds and a nominal beam width of 5-10 mm (Yan et al., 2013).

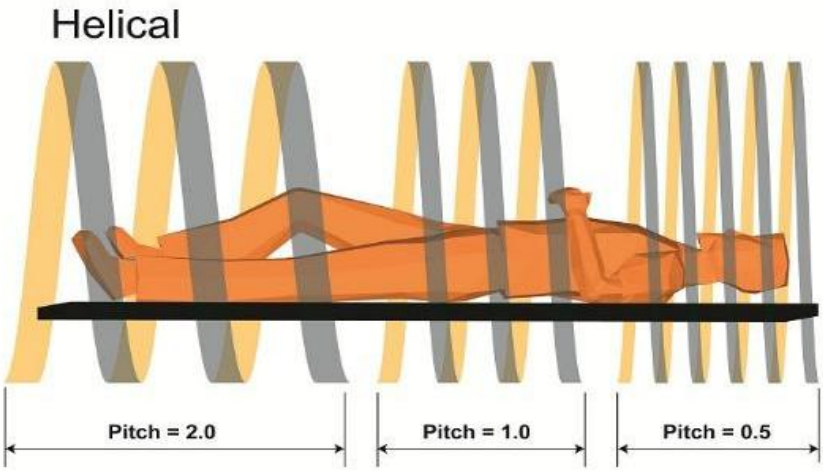

Figure 2.12: Effects of a different pitch for helical CT scan.

All C-arm CT and micro-CT scanners are using the cone-beam CT configuration. Figure 2.13 and figure 2.14 demonstrate the major difference between the cone beam and the fan beam.

The cone-beam CT uses flat-panel-based detectors, while clinical multi-row CT uses a dedicated curved detector.

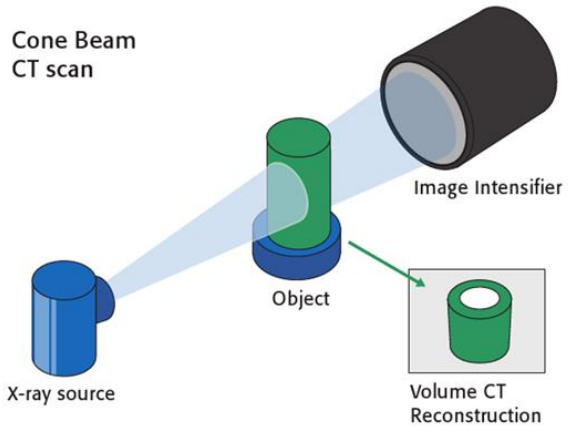

Figure 2.13: Schematic of cone-beam CT (Reiser et at., 2009).

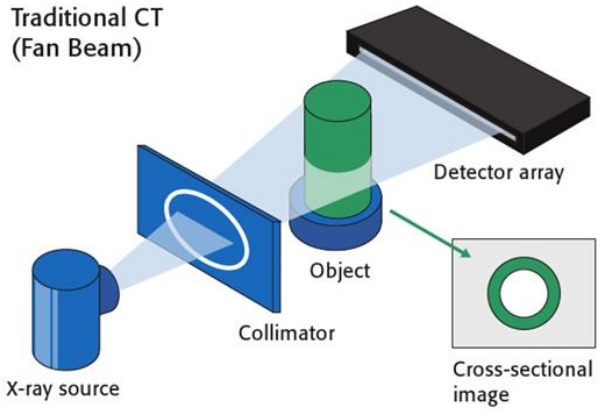

Figure 2.14: Schematic of fan-beam CT (Reiser et at., 2009).

Dual-source CT (DSCT) systems were introduced, which have two x-ray tubes and two detectors mounted on the same rotating gantry with a 90^{o} angular offset. Figure 2.15 depicts such a system. Cardiac imaging with a better temporal resolution is the key advantage of DSCT.

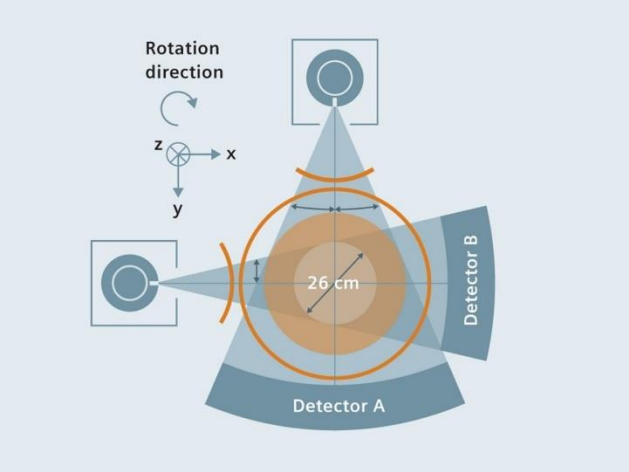

Figure 2.15: Dual-energy CT scan (courtesy Siemens).

The higher temporal resolution allows for a time-dependent heart function to be added to the morphological data derived from x-ray attenuation coefficients. The scanner also provides separate mA and kVp settings for both x-ray tubes, allowing for simultaneous dual-energy data capture to support tissue differentiation (Brodoefel et al. 2007).

2.7 Hybrid imaging

Positron emission tomography/computed tomography (PET/CT) is primarily a nuclear medicine procedure that combines a PET system and a CT system into a single gantry system. Therefore, images can be obtained sequentially on both scanners during the same session, and united into a single co-registered image (Saha et al., 2016). The first PET/CT scanner was developed in the late 1990s.

PET imaging is a three-dimensional molecular imaging technique that produces functional images of the body. Moreover, PET is significantly superior to CT in the recognition of malignant and benign lesions, the assessment of therapy response, and the detection of viable tumor cells after treatment. Therefore, in the past few years, the use of clinical hybrid PET/CT systems has increased rapidly, and such a development has directed to an increase in the use of CT-based attenuation correction (Bushberg et al., 2012). PET/CT is an essential cancer diagnosing and staging tool. It is beneficial in the entire spectrum of cancer care for example in diagnosis, evaluation of treatment responses, and treatment planning (Hausmann et al., 2012). PET/CT has transformed medical diagnosis in many fields by appending precision of anatomic localization to functional imaging, oncology, cardiology, neurological diagnostic imaging as well as surgical planning (Schoder et al., 2004).

2.7.1 Significance of hybrid imaging

Nuclear medicine imaging, PET, and SPECT are superior to conventional imaging such as CT and MRI in the detection of tumors (Schöder et al., 2004). Although there is anatomical information in some nuclear medicine tests, the spatial resolution is limited when compared to CT or MRI. As the clinical decision is not only based on the signal coming out of the body but also on the exact extent and the location of the site from where the signal being originated, for several decades low-resolution nuclear medicine images were compared with high-resolution CT or MRI images. Usually, in the early days, both images were acquired on separate systems at different time points. It was quite difficult to co-register these images. In image co-registration to obtain spatial correspondence on a one-to-one basis, parameters like matrix size, voxel intensity, and image orientation are adjusted between two sets of images (Hausmann et al., 2012). The process of image co-registration is also called image fusion. Patient position reproduction is essential for image co-registration; however, x-rays images and nuclear medicine images do not correspond properly and result in misregistration of the image leading to inaccurate determination of the disease localization (Rachel et al., 2013). To ensure accurate registration of two images combined systems were developed having two modalities physically attached in a single unit. Combined systems are known as PET/MRI and PET/CT hybrid scanners. In PET/CT hybrid system CT images are used for anatomical localization of activity and also CT data can be utilized to create an attenuation map for gamma rays as they transverse the body tissues to reach the detector (Hausmann et al., 2012).

2.8 PET/CT system

David Townsend, Ron Nutt, and colleagues have developed the first PET/CT scanner in the late 1990s. A single slice CT scanner and a partial ring PET scanner were both installed on a single gantry in this setup (Rachel et al., 2013). The tandem arrangement is a modern back-to-back PET/CT scanner where the PET and CT scanner's fields of view are separated axially by around 60 to 120 cm. PET and CT components are separate in these systems. The CT part of a PET/CT scanner is closer to the patient, and the CT scan is frequently acquired before the PET scan.

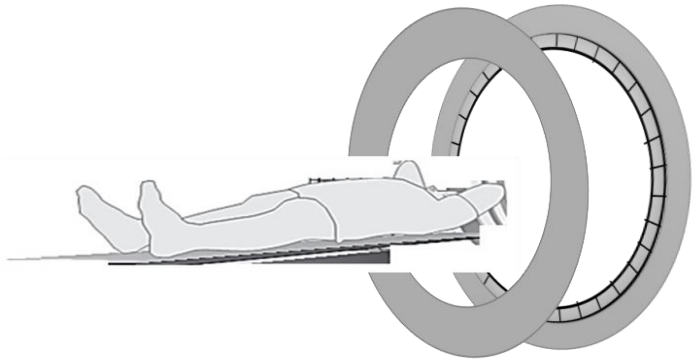

Figure 2.16: Schematic of PET/CT system

PET/CT system is primarily used for whole-body imaging, for example, using ^{18}F-FDG as a radiotracer, in cancer patients. CT component is used to provide precise anatomical localization of tracer uptake in the tumor or its metastatic sites. CT vbvdata is being used for an attenuation map for PET scans that can be generated using CT data.

Positron emission tomography detectors can detect the annihilation of photons (511 keV) resulting from the annihilation process after a positron-electron interaction. Annihilation photons can also be detected by SPECT detectors operating in conventional mode counting single-photons, but these detectors are designed for lower energy single-photon detection and have comparatively less efficiencies at annihilation photon energies. Data reconstruction is similar to SPECT with the exemption that attenuation correction is always performed in PET by CT data. PET provides a variety of benefits over typical gamma cameras, including sensitivity, high resolution, and the availability of positron emitters with low atomic numbers. The principal drawback of PET is equipment cost and the rapid decay of positron emitters. Since in PET oppositely directed 511 keV annihilation photons are detected simultaneously, to locate the position of annihilation reaction and direction of detected photons no collimator is required. This is known as annihilation coincidence detection. PET has higher sensitivity than traditional gamma cameras as PET cameras have 360° detector coverage. PET/CT has been an extensively used modality in nuclear medicine (Saha et al., 2016).

2.8.1 Basic principles of PET imaging

Two 511 keV photons are produced, when a positron mutually annihilates with an electron they travel directly opposite to each other. Depending on the energy of positron annihilation, photons are emitted within a few tenths of a millimeter to a few mm of the position of positron

emission. The origin of annihilation photons can be localized on a line between the two detectors by simultaneous detection. This mechanism of photon detection is called annihilation coincidence detection (Bailey et al., 2005), after a pair of photons is detected in a 6 to 12 ns coincidence window.

When two events occur within a given time range, coincidence detection generates an output. Generically, these events are known as prompt coincidences. Prompt coincidences may be of the following three types;

2.8.1.1 True coincidence events

PET has high resolution due to coincidence detection. If two annihilation photons are detected on two detectors located opposite each other, the annihilation event took place along a hypothetical line between the two detectors. The imaginary line is called the line of response as shown in figure 2.17. These simultaneously detected events are registered by a coincidence circuit. Events resulting from a single positron annihilation reaction are referred to as true coincidence events.

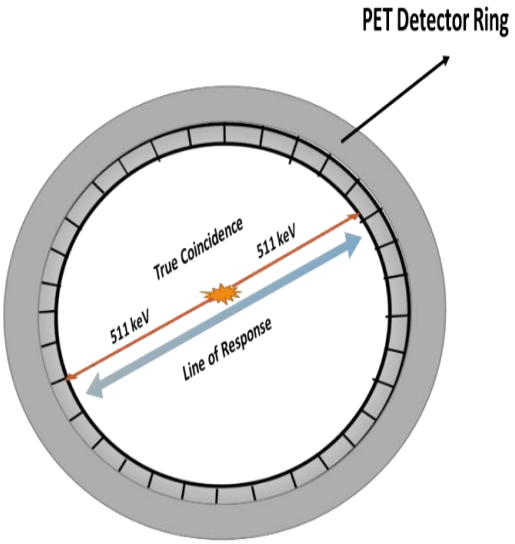

Figure 2.17: Line of response and true coincidence events.

2.8.1.2 Single events

A single event is reported when an unpaired photon from a non-annihilation event reaches the detector. In other words, unpaired photons detection is known as a single event shown in figure 2.18. In PET imaging impact of single events is rejected.

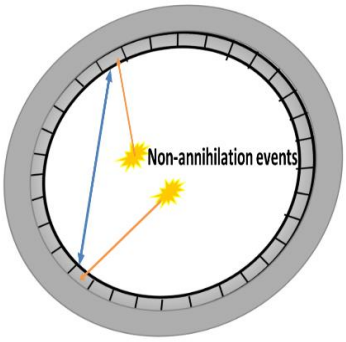

Figure 2.18: Single event due to non-annihilation events detected at two detectors with the timing and energy window of the system.

2.8.1.3 Time of flight measurement

The resolution of the system is improved with the use of time of flight measurement. The assumption used in time-of-flight measurements is that annihilation reaction can be localized along the line of response by measuring the timing difference between two photons arriving at opposing detectors. Photon arrival time difference is proportional to the difference in distance traveled by two photons along the line between pair of detectors (Saha et al., 2016, Rachel et al., 2013).

2.8.2 PET detectors

One of the important parameters of PET sensitivity and performance is its detection efficiency. Mostly PET systems use high-Z scintillation detectors, which are organized in rings of detector elements around the item being imaged (Bushberg et al., 2012). Usually, circular rings of detectors have diameters ranging from 70 to 90 cm and an axial length of 15 to 25 cm. In early systems, individual detectors have been used that consist of a scintillator crystal attached to a PMT. The early PET scanner was operated in 2-D mode, allowing only coincidence detection due to septa between detector rings. Today almost all scanners have no septa between rings providing 3-D acquisition. 3-D acquisition increases the scanner sensitivity but also made reconstruction and correction more complicated. Small crystals are arranged in a matrix form to make up a block. Block detectors are attached to PMT (Rachel et al., 2013). The block detector was designed by Cassy and Nutt (1980s), they used smaller crystals to improve spatial resolution and a smaller number of PMTs to control. Optical cross-talk between scintillator elements is decreased by filling the gaps between the elements with a reflecting substance. Block detectors are advantageous as they allow the decoding of many detector elements using only four PMTs. This improves the spatial resolution and decreases the cost per detector

element. 20 to 30 mm thick scintillator crystal is used to make a block detector with a sub-element width of 4 to 6 mm (Saha et al., 2016). The original block detector design is modified by making two modifications. In the first modification, proportionally larger PMTs are positioned in a way to overlap part of adjacent blocks. The new design allows each block to be monitored by four PMTs and the adjacent corner of four blocks is monitored by a single PMT. This approach is known as the quadrant sharing approach. This approach is useful in creating larger panel detectors for PET systems. With the advantage of cost reduction, the quadrant panel approach has the drawback of extended dead time, as each PMT is accumulating signal from a large scintillator volume. In the second modification single scintillation material is replaced by two different scintillation materials, the resulting combination is called phoswich. The decay time difference between two scintillators is utilized to locate events in the upper or lower scintillator layer. The disadvantages of this approach include manufacturing complications and differing stopping power and light output of two scintillator materials.

A whole-body PET system may use discrete element crystal or continuous detectors with a larger area. Discrete element detector design may be arranged in full ring modular block detector design.

2.8.2.1 Scintillator detector crystals

The energy of gamma photons is converted into the energy of light photons in crystals. The conversion of gamma energy to light photon energy is a complicated process. Compton or photoelectric interactions are used by gamma rays to interact with the crystal. Electrons produced as a result of these interactions pass on their energy to electrons in the crystal, causing them to become excited. Excess energy is emitted by these excited electrons as light photons, which return them to their original condition. Thallium-doped sodium iodide NaI(Tl) crystal is one of the earliest detector crystals used for PET systems. Due to its relatively low-density sodium iodide crystal is less effective at absorbing 511 keV photons. To overcome the low-density problem of sodium iodide, crystals having a high atomic number and high density have been developed, such as bismuth germinate $Bi_4Ge_3O_{12}$ (BGO), lutetium oxyorthosilicate Lu_2SiO_5 (LSO), gadolinium oxyorthosilicate Ga_2SiO_5 (GSO) and lutetium yttrium oxyorthosilicate (LYSO). For 511 keV annihilation photons, these detectors have comparatively high stopping power. In high Z crystal photon interaction per unit volume increase as the probability of photoelectric effect increase with Z number. Photoelectric interactions are preferred over Compton interactions, in detector design, as in photoelectric interactions most of the photon energy is imparted to photoelectrons, and electrons deposit

almost their total energy close to the location of photoelectric interaction. In the case of Compton scattering, only a slight amount of energy is shifted to the electron and most of the energy is carried by the interacting photon out of the crystal. Properties of detector crystals including density, decay time, light yield are given in table 2.1. LSO, LYSO, and GSO have shorter decay time and higher light yields as compared to BGO and NaI. The shorter decay time is advantageous because it is the time in which an excited atom returns to its ground state.

Table 2.1: Detector crystal properties

CRYSTAL	DENSITY(G/CM^3)	DECAY TIME (NS)	%AGE LIGHT YIELD (RELATIVE TO NAI)
NAI(TL)	3.67	230	100
BGO	7.13	300	14
GSO	6.71	60	41
LSO	7.40	40	75
LYSO	7.40	40-44	75

During decay time a second gamma-ray entering the crystal cannot be absorbed. The number of light photons per unit of energy absorbed is called light yield. For greater spatial resolution and better energy resolution higher light yield is required. Better energy resolution makes it possible to distinguish lower energy scattered or non-annihilation photons from annihilation photons.

Improved light output also improves spatial resolution, as with a larger number of photons it is easy to categorize exactly which detector crystal detected the annihilation of photons that in turn improves spatial resolution. LSO and LYSO are more suitable detector crystals due to their high density, low decay time, and high light output (Bailey et al., 2005, Townsend et al., 1993).

2.8.2.2 Data acquisition for PET

The basic concept of PET data acquisition is the detection of annihilation of photons coming out of the patient's body as a result of positron-electron annihilation. A coincident event is registered if two photons arrive at the detector within a short timing window (Bailey et al., 2005, Lewellen et al., 2004). This method of coincidence detection is known as electronic

collimation. Events detected within the timing window are known as prompts, prompts include all types of three coincidence events (true, random, scatter) (Tong et al., 2010).

2.8.2.3 2-D Data acquisition

Earlier PET scanners were developed with septa between detectors rings. Septa allow only those photons to reach the detector which was originated in direction of the detector ring. The mode of acquisition is called 2-D data acquisition. Scattered annihilation photons are rejected by septa. The acquired projection data is similar to data acquired by a gamma camera using a parallel hole collimator, as a single slice acquisition is possible for each detector ring. In the 2-D acquisition mode, those annihilation photons are rejected that are emitted at oblique angles. In this way, perhaps useful events annihilation photons are rejected by septa (Bailey et al., 2005) and consequently, the sensitivity of the scanner is reduced.

2.8.2.4 3-D Data acquisition

In the 3-D mode of data acquisition, no septa are used between the detector rings. Sensitivity is increased four to eight times as data are acquired for all normal and oblique lines of response. However, random and scatter coincidence detection is also increased in 3-D acquisition mode degrades the spatial resolution, and increases the memory required to store data (Saha et al., 2016). Although 3-D data acquisition requires large storage and high computational power, due to increased sensitivity, all commercial scanners offer 3-D acquisition mode as an option.

2.8.3 PET data corrections

The intensity of the reconstructed image must be proportionate to the activity concentration at the relevant place in the subject for an appropriate comparison of activity concentration in various organs or normal versus malignant tissues. The following corrections are applied to PET data during reconstruction (Saha et al., 2016);

2.8.3.1 Normalization

The number of detector elements in a common PET scanner range from 10,000 to 30,000. The detector element dimensions and scintillation light output may be subjected to small variations. Also, the effective thickness traveled by the photon varies for the varying angle of incident. These variations are adjusted by normalization correction. All detectors are exposed to the same radiation source and the number of counts recorded by every detector pair is recorded. Ideally, all detector pairs would record a similar number of counts but in practice, there is variation in detector efficiencies. Normalization factor is $f_{i,j}$ computed as:

$$f_{i,j} = \frac{n_{i,j}}{< n >} \quad (2.8)$$

<n> is the average of $n_{i,j}$ counts for coincident detector pairs. The number of counts recorded by every detector pair is corrected by normalization factor.

$$N_{norm_{i,j}} = \frac{N_{i,j}}{f_{i,j}} \quad (2.9)$$

$N_{i,j}$ is the recorded number of counts. This correction is applied before image reconstruction (Cherry et al., 2012, Brodoefel et al., 2007).

2.8.3.2 Random correction

Random coincidences cause image artifacts and suppress image contrast by adding a uniform background across the image. The delayed window method and singles method is used to estimate random coincidences. In the delayed window method coincident timing window is delayed at a time that is much longer than its width. In a delayed window no true counts are accepted and only counts with that much delay are accepted. The detected counts are subtracted from total coincident events. In a single method the estimate of random events is based on the following equation;

$$n_{random} = \Delta t \, n_{single,1} n_{single,2} \quad (2.10)$$

Δt is coincident timing window, $n_{single,\ 1}$ and $n_{single,\ 2}$ are count rates at opposite detectors of coincident pair (Wachtel et al., 2009, Lewellen et al., 2004).

2.8.3.3 Scatter correction

Scattered radiation causes an unclear background in the reconstructed image. Like random events scatter events also decrease image contrast and affect the relationship between perceived activities in the image to actual activity in the object. Two methods of scatter correction are currently used for PET. In the first approach original scattered contaminated and transmission images are used to estimate the scattered contribution. The estimated scattered contribution is deducted from projection data and reconstruction is done again. In the second approach, projection profiles are examined just outside the object. Interpolation of an analytic function is made from outside the object to the source inside the object. Scattered corrected data is obtained by subtraction of interpolated scattered counts from measured source counts.

2.8.3.4 Attenuation correction

The most significant correction is attenuation correction. For attenuation correction two basic approaches are being used. The first one is the use of a positron-emitting source for transmission scans. In this approach, two measurements are made, a blank scan without an object and a transmission scan with the object in the scanner. The attenuation correction factor for pair i,j of detectors is calculated as;

$$f_{att_{i,j}} = \frac{n_{blank,i,j}}{n_{trans,i,j}} \tag{2.11}$$

Here n_{blank} and n_{trans} represent counts recorded by the detector pair in the blank and transmission scan. In the second approach, CT transmission data is utilized for attenuation correction. However, linear attenuation coefficients measured by the CT systems are much different from the attenuation coefficient for 511 keV annihilation photons. To use CT information for PET data attenuation correction, the linear attenuation coefficient for 511 keV photons essentially be predicted from the linear attenuation coefficient measured by CT systems. One technique of determining the attenuation coefficient for 511 keV photons using the CT number methodology is to split the voxels into two groups. Soft tissue, fluids, or gases, or a mixture of them, are thought to be found in voxels with CT numbers less than a certain value, while bone minerals and soft tissue are thought to be found in voxels with CT numbers more than that value. The linear attenuation coefficient for 511 keV is derived using equation 2.12 for low CT number voxels,

$$\mu_{511} = (9.6 \times 10^{-5} cm^{-1})(CT\ no. + 1000) \tag{2.12}$$

For air CT no. = -1000 and μ_{511}= 0 and for water CT no.= 0 and μ_{511}= 9.6×10^{-5} cm^{-1}. For high CT number voxels linear attenuation coefficient for 511 keV photons is computed as given in equation 2.13.

$$\mu_{511} = m(CTno.) + b \tag{2.13}$$

Where m and b are constant, their values are determined empirically and differ from the kV used by the CT system (Bushberg et al., 2012).

2.8.3.5 Deadtime correction

The minimum time interval that two consecutive counts must be separated to be recorded as two different events is called a dead time of the system. With large counting rates, PET

detectors also exhibit dead time effects. A second event occurring during the dead time cannot be registered and ultimately the event will be lost. In PET systems, dead time loss is a severe issue. Using detector materials with less decay time and quicker electronics is one technique to reduce dead time. Empirical models are used for dead time corrections in which the range of object size and energy threshold is used to measure the count rate as a function of activity concentration. In another model, the true count rate is obtained by extrapolating low activity data to high activity data.

2.8.3.6 Decay correction

When using ^{18}F-FDG for the measurement of glucose metabolism decay correction is necessary because the half-life of ^{18}F is slightly longer than the scan duration. Decay correction is necessary for PET data during the data acquisition. The effective decay factor is given in equation 2.14;

$$f_{eff} = e^{-(\frac{ln\ 2 \times t}{T_{1/2}})} \times [(1 - e^{-x})/x] \tag{2.14}$$

Where $x = \ln 2 \times \Delta t / T_{1/2}$ (Dance et al., 2014).

2.9 CT based attenuation correction

In hybrid PET/CT scanners PET and CT are intrinsically co-registered. CT data can be utilized to adjust attenuation in PET. As a result, the PET system doesn't need separate transmission sources, and total scan times will be cut in half. In certain circumstances where the patient's radiation dose is of great importance, such as young children or volunteers engaging in clinical studies, the choice to incorporate a transmission source may be relevant. The CT scan reduces the overall PET scanning time in half and enhances the accuracy of the attenuation correction parameters (Tong et al., 2010).

When the CT scan is finished, the CT attenuation coefficients for various tissue types are mapped to their relevant PET energies (511 keV) to create a PET attenuation correction map. This process is currently carried out using a variety of conversion methods. (Kinahan et al., 1998) proposes a system that separates CT images into distinct tissue categories and then adjusts each tissue attenuation coefficient to its associated PET standards using predetermined scaling factors. Bilinear transformation, which may be thought of as a combination of segmentation and scaling approaches, is another method used by GE Healthcare.

It is important to remember that linear attenuation is energy-based while employing CT data for PET attenuation correction. PET uses monoenergetic 511 keV photons, whereas CT scans

use a range of x-rays ranging from 40 to 140 keV. As a result, the CT-derived attenuation must be scaled to the proper energy for PET. For annihilation of photon energies of 511 keV, Compton scattering is the main process. But, in the CT energy value, photoelectric absorption is the predominant source of attenuation in bone (Khalil et al., 2017). At 511 keV, there is no easy method for converting Hounsfield units to linear attenuation coefficients that are applicable for every material. The photoelectric and Compton contributions to attenuation can be extracted using a dual-energy CT scan, as suggested by (Kinahan et al., 2003). But, when other, simpler means of correction are available, this increases the patient doses unnecessarily. The segmentation method, for example, substitutes the CT number in the reconstructed image with a tissue-specific attenuation value of 511 keV.

The density of some tissue types varies significantly and cannot be effectively represented by a discrete value, which is one drawback of this technique. A scaling strategy is an alternative technique that involves multiplying the entire CT image by the ratio of water attenuation coefficients (representing soft tissues) at CT and PET photon energies (Bailey et al., 1998, Tong et al., 2010). The attenuation coefficients at different energies are assumed to have a constant ratio in this technique. A bilinear or hybrid technique can be used instead because this is an unsatisfactory approximation for bone. In the bilinear procedure, CT numbers are given a distinct scaling factor based on a threshold set between 0 and 100 Hounsfield units. All body materials are assumed to be linear mixtures of air and water or water and bone in this technique. By first calculating the attenuation map at 511 keV and then differentiating the tissue types based on CT number and using various scaling factors for bone and non-bone components, the hybrid technique includes both scaling and segmentation.

When applying CT-based attenuation correction in nuclear medicine, there are several potential sources for adding artifacts or biases. The spatial resolution of the CT image is often substantially higher than that of the PET or SPECT investigation. With PET/CT scanners, artifacts might arise if the resolutions are not matched.

A 511 keV attenuation map is generated from the CT image to compensate for the PET emission data for photon attenuation. The use of CT to obtain transmission images for PET emission data attenuation correction has four major advantages: CT data will have far less statistical noise than transmission data recorded with radioactive sources, especially for whole-body PET imaging. Second, a CT scan can be obtained significantly faster than a traditional PET transmission scan (Fessler et al., 2000). The capacity to gather uncontaminated post-injection transmission scans is the third factor, which is a significant practical consideration.

Emission photons contaminate radionuclide-based transmission scans until the transmission data is obtained before the PET agent is supplied to the patient. CT transmission scans, on the other hand, can be obtained at any moment after the PET tracer has been activated. Fourth, with x-ray transmission scanning there is no requirement for PET transmission hardware as well as the necessity for ^{68}Ge positron sources to be replaced regularly. The direct inclusion of anatomical data acquired from CT into the PET image reconstruction procedure is a potential benefit that has yet to be extensively explored.

Chapter 3. Tomographic Reconstruction Methods

3.1 Image reconstruction

The mathematical process of converting projection data into a cross-sectional image of an object is known as image reconstruction (Bushberg et al., 2012). When the pencil x-ray beam passes the plane, the linear attenuation of the x-ray via the object f (x, y) is provided as the line integral along the beam path L in equation 3.1;

$$\frac{I_t}{I_0} = exp^{-\int_L f(x,y)ds} \tag{3.1}$$

The line integral, on the other hand, provides the total attenuation p of a ray at location r on the projection at angle θ;

$$P(r,\theta) = \quad -\ln(\frac{I_t}{I_0}) = \int_{L\,(r,\theta)} f(x,y)ds \tag{3.2}$$

A density profile of the object at θ is given by the line integration of the object along all parallel lines;

$$\mathrm{p(r,\theta)} = \int_{-\infty}^{\infty}\int_{-\infty}^{\infty} f(x,y)\delta(xcos\theta + ysin\theta - r)dxdy \tag{3.3}$$

The line integral at θ in the coordinate system (r, s) can be expressed as;

$$\mathrm{p(r,\theta)} = \int_{-\infty}^{\infty} f(rcos\theta - \mathrm{s}\,sin\theta, rsin\theta + \mathrm{s}\,\mathrm{cos\theta})\,ds \tag{3.4}$$

3.1.1 Projection

A pencil beam transverse the 3D object as shown in figure 3.1. The line integral in x-ray CT represents the overall attenuation of the x-ray beam as it is transverse through the item in a straight line. An object's projection is consist of a set of line integrals at a given angle θ. A set of several such projections for various angles arranged in 2D is called a sinogram.

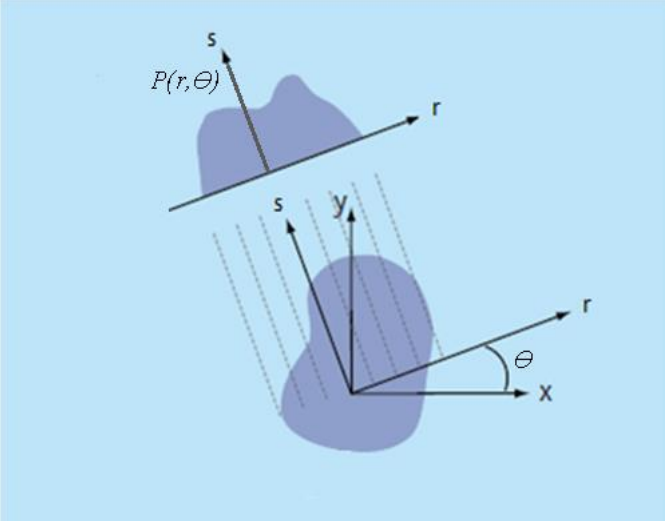

Figure 3.1: A pencil beam transverse the object and the line integral along the beam path provide one point of the profile P(r, θ).

In the image reconstruction f (x, y) is calculated from the series of measurements p(r, θ). The x-ray transform produces the set of all line integrals, while the Radon transform produces a set of integrals over all hyperplanes.

For reconstruction procedures usually, it is assumed that the x-ray is monochromatic. Therefore, $p(r, \theta)$ can be estimated:

$$p(r, \theta) = \ln[\frac{I_0(r, \theta)}{I(r, \theta)}] \tag{3.5}$$

Regarding the integral in the projection equation 3.4, it is assumed that a continuous detector as well as continuous reconstruction volume. An actual detector is discrete and the reconstruction volume is discretized in pixels. The discrete form of the projection is:

$$p_i = \sum_j a_{ij} f_j \tag{3.6}$$

Where *i* is the index for sinogram pixels (r, θ), *j* is the index for image voxels (x, y) and a_{ij} defines the intersection length of the projection line *i* with voxel *j*, and *f* is the real distribution of the attenuation.

3.1.2 Back projection

The back-projection is fundamental to all analytic tomographic reconstruction algorithms. The projection technique maps a two-dimensional object f(x, y) into a sinogram p(r, s), which contains all line integrals through the object (Saha et al., 2016). The back-projection is the adjoint operation of projection, which is defined as:

$$\hat{f}(x,y) = \int_0^{\pi} p(x\cos\theta + y\sin\theta, \theta)\, d\theta \tag{3.7}$$

$$= \int_0^{\pi} p(r, \theta)\, d\theta \tag{3.8}$$

In the parallel-beam geometry, all projection values back to the volume along the same projection lines are used to produce the sinogram. The back-projection gives a blurred version of the object. The discrete version of equation 3.8 is

$$b_j = \sum_i a_{ij} p_i \tag{3.9}$$

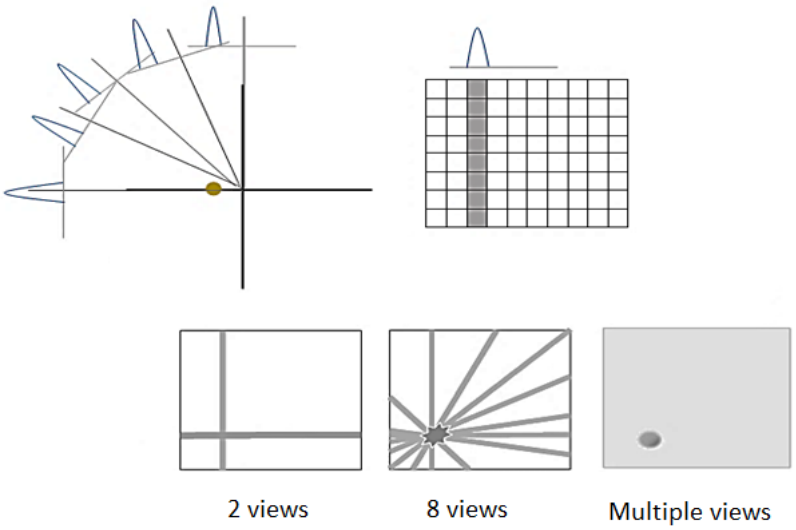

Figure 3.2: Back Projection.

3.2 Reconstruction algorithms

In the process of 3D reconstructing an object from its projections, practical reconstruction algorithms have been formulated. The mathematics of the Radon transform, the geometry of the data, statistical knowledge of the data scanning procedure, and the imaging system are all used to create these methods.

3.2.1 Analytic reconstruction

An analytical reconstruction algorithm is based on the continuous representation of the object and the sinogram (discretization is only used to implement the algorithm), it is a mathematical inversion, and provides a one-stop solution.

3.2.1.1 Direct Fourier reconstruction

The Fourier slice theorem explains the mathematical relationship between an image and its projections. It provides theoretical support for the exact inverse operation to avoid blurring from simple back-projection (Cherry et al., 2012, Saha et al., 2016).

The Fourier transform of a 2D object is:

$$F(\theta,\omega) = \int_{-\infty}^{\infty} p(r,\theta)\, e^{-j2\pi\omega r} dr \tag{3.10}$$

$$F(\theta,\omega) = p_\theta(\omega) \tag{3.11}$$

The object could theoretically be exactly reconstructed by applying a 2D inverse Fourier transform (equation 3.10) for the 1D Fourier transform of the projections. If an indefinite number of projections are measured, $F(\theta,\omega)$ would be known at all positions in the frequency domain.

The reconstruction process includes the following steps

1. Compute, $F(\theta,\omega)$ from the 1D Fourier transforms of the projections at all angles
$$F(\theta,\omega) = FT\{p(r,\theta)\}$$
2. Convert $F(\theta,\omega)$ from polar coordinate into a Cartesian coordinate in the Fourier domain, grid interpolation
3. Apply the 2-Dimensional inverse Fourier transform to obtain the reconstructed image.

3.2.1.2 Filtered back projection

In the filtered back-projection method, the raw data is mathematically filtered before being back-projected onto the image matrix. The filtering step mathematically reverses the image blurring, restoring the image to an accurate representation of the scanned object. The mathematical filtering step involves convolving the projection data with a convolution kernel. Many convolution kernels exist, and different kernels are used for varying clinical applications such as soft tissue imaging or bone imaging (Tong et al., 2010).

$$f(x,y) = \int_0^{\pi} p'(r,\theta)\, d\theta \tag{3.12}$$

The mathematical filtering operation (convolution) is the difference between filtered back projection and simple back projection. The Fourier transform (FT) converts a function defined in the spatial domain (millimeters) to the frequency domain (cycles per millimeter), and the inverse Fourier transform (FT^{-I}) converts it back.

$$P'(r, \theta) = P(r, \theta) \otimes k(r) \tag{3.13}$$

Where the filtered data in the spatial domain is p' (r, θ), p(r, θ) is the projection data (in the spatial domain) at a specified angle, and convolution is represented by the symbol $\otimes$.

$$k(r) = W\frac{\sin(2\pi Wr)}{\pi r} - \frac{sin^2(\pi Wr)}{\pi r^2}$$

k(r) represents the spatial domain kernel and W is the cutoff frequency typically chosen to be the Nyquist frequency. Ramp filtering or convolution can be further combined with low pass filtering, e.g. Hann filtering, to remove the undesired noise in the measured data.

$$P'(r, \theta) = FT^{-1}\{FT\,[P(r, \theta) \times K(f)\} \tag{3.14}$$

Where K(f) = FT[k(r)], is the kernel in the frequency domain. According to equation 3.14, the convolution operation is achieved by Fourier transforming the projection data, multiplying (not convolving) it by the frequency domain kernel K(f), and then applying the inverse Fourier transform to the result to obtain the filtered data to be back-projected.

3.2.2 Iterative reconstruction

An iterative algorithm commences from a discrete sinogram as well as an object, based on the numerical inversion, and iteratively updates the image. Iterative algorithms use several iteration stages to find the proper solution, allowing for an improved reconstruction by a longer calculation time.

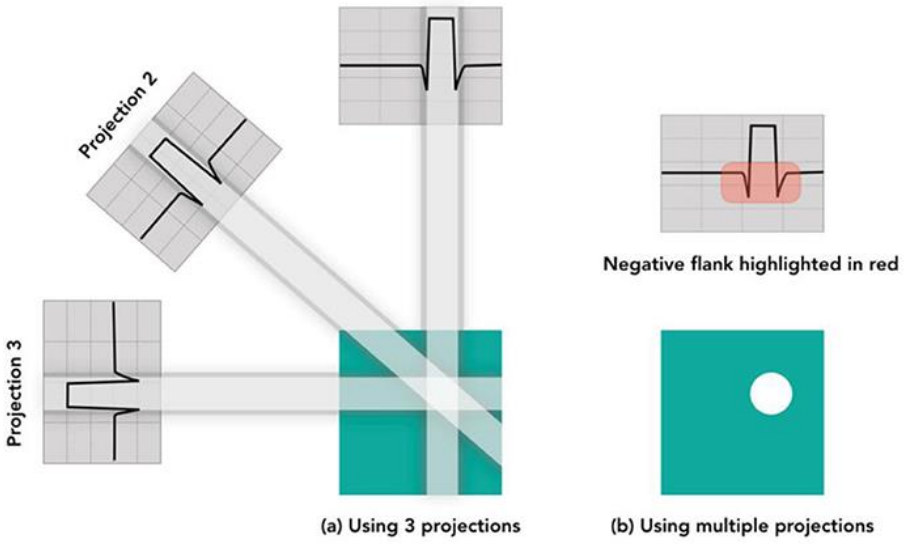

Figure 3.3: Reconstruction with filtered back projection (Gonzalez et al., 2018).

The first image at the initial iteration is often an image having uniform numbers in each voxel. Forward projection of the CT image approximation provides a series of estimated angular projection images by modeling the acquisition of the projection data by integrating along the different ray paths (Cherry et al., 2015). The iterative reconstruction algorithm image estimate goes through the forward model and the residual errors in the projection domain are back-propagated via the transpose of the forward model. Every iteration initiates with an approximation of the CT image to be reconstructed.

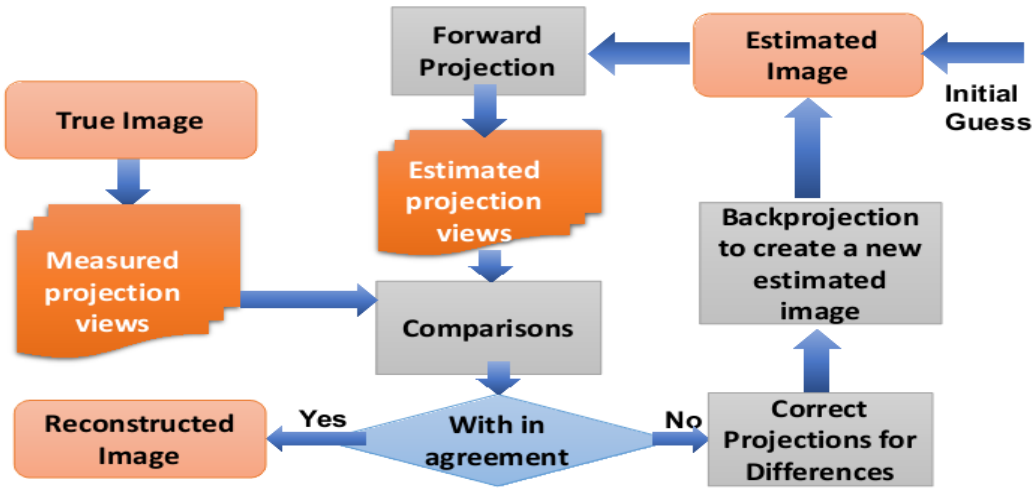

Figure 3.4: Schematic of an iterative reconstruction method.

The computed projections are then compared with the actual measured projections and the discrepancies are computed as a cost function, that is utilized to update the next estimate of the CT image by a back-projection. Iterative reconstruction aims to gradually decrease the cost function till the disparities among the approximated and actual projections have converged to the expected phase.

The method that uses the ratio of two projection views, computed projection views, and measured projection views, to generate a correction factor is known as Maximum Likelihood Expectation Maximization (MLEM), the Additive Simultaneous Iterative Reconstruction technique (ADIR) is using the difference between two projection views. Mathematically iterative reconstruction can be described by the equation;

$$p_i = \sum_{j=1}^{m} a_{i,j} q_j \tag{3.15}$$

$$q_j^{k+1} = \frac{q_j^k}{\sum_i^n a_{i,j}} \sum_i^n \frac{a_{i,j} p_i}{\sum_j^m a_{i,j} q_j^k}$$

Iteration number is represented by k and the number of bins by n. $s^{k+1}{}_j$ updated estimate and $s^k{}_j$ is the initial estimate (Saha et al., 2016). The iterative reconstruction method has the disadvantage of a large number of iterations to achieve an acceptable image estimate. A large number of iterations requires extended computation time to reconstruct the image (Khalil et al., 2017).

The problem of computational time in iterative reconstruction is solved by the introduction of the Ordered Subset Expectation Maximization (OSEM) algorithm. OSEM is a modification of MLEM, in that groups of projection views are generated called subsets, and MLEM approach is used on these subsets. MLEM is applied to one subset at a time the resulting correction is used for the next subset. When all subsets in the set of projection views are processed an iteration is said to be completed. The convergence of the estimate to the measured image is accelerated by the number of the subset in OSEM approach. If there are n subsets in OSEM approach and 2 iterations, MLEM would reach the results of OSEM by 2n iterations of all projection views. Image variance increases with the number of subsets, so an optimized number of subsets is necessary for optimum image quality and acceptable computational time.

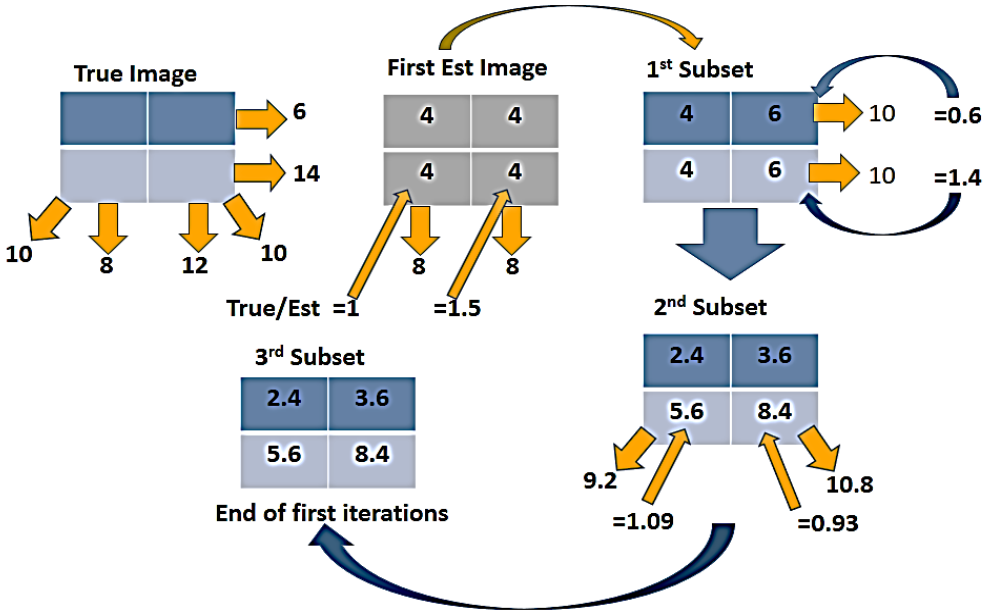

Figure 3.5: Schematic of OSEM reconstruction method (Saha et al., 2016).

The forward projection step during the iterative reconstruction technique uses accurate and realistic physical models. These models include the x-ray spectrum, detector responses, focal spot size, and photon statistics. The more accurate modeling of the acquisition procedure in the iterative reconstruction approaches offers a significant dose decrease without compromising the image quality, that is an important benefit of iterative reconstruction algorithms in CT (Beister et al., 2012).

3.3 Image artifacts in CT

The distortion of signal that obscures the interpretation of a study or irregularity that appears in an image not exist in the object but is produced by some external action is called artifact in CT. Physics-based artifacts appeared due to the acquisition of CT data. Patient movement or metallic implants in the patient's body cause patient-based artifacts. CT system artifacts result from a defective scanner and the image reconstruction method. Artifacts in clinical CT may render images that are not interpretable (Barrett et al., 2004) or reduce the diagnostic value of the images (Hsieh et al., 2009) by hiding underlying pathology.

The categories of the artifact that can be encountered are outlined:

1. Patient motion: voluntary and involuntary patient motion are very common causes of image artifacts in CT imaging. Small blurring is caused by little motion, and larger physical dislocations appear as image ghosting.

2. Noise: Statistical error of low photon counts is Poisson noise, which generates random thin dark and bright streaks.
3. Beam hardening: It generates dark strips between two high attenuation objects (such as bone or metal), with adjacent bright strips.
4. Rings artifacts: Generally, appears as a result of errors in individual detector calibration.
5. Metal artifacts: Metal objects in the scan field can cause significant streaking artifacts.
6. Partial volume averaging: The CT number in every pixel is proportional to the mean μ in the corresponding voxel. Partial volume averaging is especially noticeable when voxels in the image contain a variety of different tissues, such as softly rounded structures that are almost parallel to the CT slice.

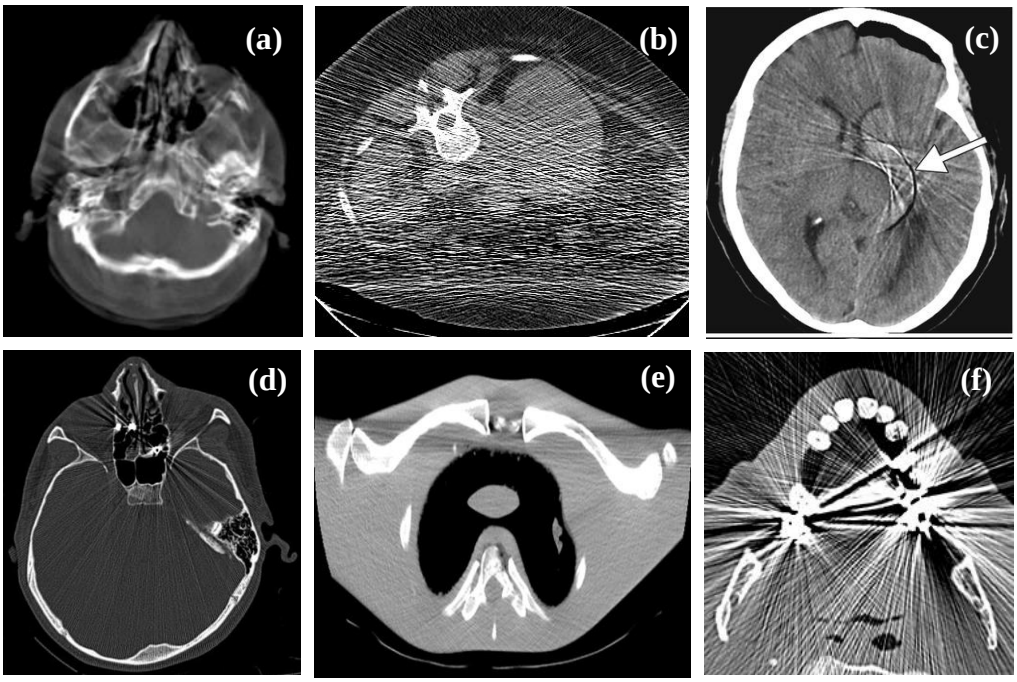

Figure 3.6: Artifacts in CT (a) patient motion, (b) Noise, (c) ring artifact, (d) streak artifact, (e) streak artifact due to photon starvation, (f) metal artifact (Boas et al., 2012).

To optimize image quality, it is essential to understand why artifacts occur and how to avoid them. Iterative reconstruction can help to eliminate the noise artifacts. Iterative reconstruction can also reduce metal artifacts, resulting in a more accurate diagnosis. CT scans with dual and multi-energy (photon counting) energy can help to reduce beam hardening and improve tissue contrast. Increased tube current can solve the problem of photon deficiency parallel to the CT slice.

3.4 Motion estimation

Patient motion can be categorized into either rigid motion (head and extremities) or non-rigid motion (heart, lung, and other internal organs).

The first group requires motion information and consists of motion acquisition and motion compensation processes. Motion acquisition derives the motion from reference images, surrogate signals, or the data themselves. Motion compensation compensates the artifacts during a reconstruction process. The second group corrects the motion artifacts using ways of image-processing techniques, without knowing the motion information.

3.4.1 Non-rigid motion estimation

The direct measurement of lung or heart movement is hard during scanning. usually, all approaches estimate a movement vector field subsequently with the acquired CT data. These methods are based on model-based techniques or feature-based techniques.

The model-based method computed the time-varying motion field by considering the distortions as a collection of parameters and fitting the model to the obtained data. The motion information is obtained from the captured projection data using the feature-based technique, which tracks recognized features.

For the non-rigid motion of the internal organs, external tracking can only provide surrogate signals but not the actual motion. Cardiac and respiratory surrogate signals are measured with the help of dedicated devices in diagnostic imaging, image-guided surgery, and radiation therapy (Li et al., 2010, Gendrin et al., 2012).

To estimate internal motion fiducial markers are used to track the movement of internal organs, this practice is stated as internal tracking. Accurate beam delivery is crucial in radiotherapy; therefore, internal tracking is frequently used in radiotherapy (Gendrin et al., 2012).

3.4.2 Rigid motion estimation

Numerous methods have been recently developed for rigid motion estimation. Rigid transformations can be indicated with three translations (Tx, Ty, and Tz) and three rotations (Rx, Ry, and Rz) parameters about the x, y, z-axes, respectively.

3.4.2.1 Reference images

When the prior motion-free scan of the same patient is available the motion information can be computed. The researcher derives motion from the reference scan by 2D/3D registration that estimates the motion of the reference volume that fits best to the motion-contaminated

projections. Both rigid and non-rigid motion among projections can be computed with such a technique

3.4.2.2 External tracking devices

The motion can be estimated by using external or internal tracking devices. These devices are commercially available and work with acoustic, mechanical, and optical tracking techniques. Optical tracking systems are very common as they offer wireless measurement, have a fast-sampling rate, and are compact. Kim J. et al., applied a marker-based optical tracking scheme to monitor the movement of the head of a patient during helical CT scans (Kim et al., 2015).
In several medical imaging modalities, a marker-based optical tracking system has been utilized to monitor patient motion, e.g. CT (Fulton et al., 2002), PET (Herzog et al., 2005, Zaitsev et al., 2006), and MRI (Fulton et al., 1994), SPECT (Kyme et al., 2014), and also in preclinical microPET application. Markerless optical tracking techniques have been also applied in tracking head movement in positron emission tomography (PET) and CT scans (Kim et al., 2015).

3.4.2.3 Data-driven approach

The data-driven method does not need any additional measurement and is purely based on acquired raw data. The data-driven motion estimation technique is based on data consistency. Data consistency is the foundation of the data-driven motion estimate approach. Data consistency in a CT scan refers to the data redundancy resulting from several scanning positions of the same object. When motion happens, the consistency conditions in the measured data are no longer satisfied. Therefore, the motion can be estimated by forcing the data to satisfy the consistency conditions. The Helgason-Ludwig consistency condition (HLCC) is a condition describing the relationship between the Radon transform of parallel projections and the imaged object (Ludwig et al., 1966, Helgason et al., 1999). For example, in parallel-beam geometry, the zero-order HLCC describes that the summation of all projections is a constant independent of the view. HLCC was extended into fan-beam (Leng et al., 2007, Yu et al., 2006) and cone-beam geometries (Clackdoyle et al., 2013), and showed promising results when applied to motion estimation. Other consistency conditions can also be used for motion estimation including the Epipolar consistency condition (Aichert et al., 2015), Fourier consistency condition (Berger et al., 2017), and John's equation-based consistency condition (Levine et al., 2010). Nearly all the above methods were only verified in simulation studies. One probable explanation is that all consistency conditions are derived based on ideal

assumptions like continuous image and detector models, the monochromatic x-ray source, and no truncation. But a real scan cannot match all these assumptions. Therefore, artifacts from these all sources may affect the accuracy of the motion estimation, as several other factors also contribute to the violation of the data consistency.

3.5 Motion compensation

An analytical reconstruction algorithm can be used to accomplish the motion compensation. Both parallel-beam and fan-beam geometries can be reconstructed using accurate filtered back projection (FBP) in two dimensions with known affine motion (Desbat et al., 2007, Roux et al., 2004). In 3D, a generalized back-projection filtration (BPF) technique is presented to precisely reconstruct non-truncated data recorded using an arbitrary source trajectory, which is effectively a motion-corrected trajectory when motion is present (Ye et al., 2005). Others employ approximation methods to do motion compensation instead of accurate algorithms due to the difficulty of implementing an exact algorithm. Feldkamp, Davis, and Kress's (FDK) approach, for example, corrects motion in the back-projection step while neglecting ramp filtering and weighting adjustments (Feldkamp et al.). The reconstructed image quality is often acceptable when the motion is small.

It is feasible to implement motion compensation in an iterative reconstruction process in addition to an analytical algorithm. Kim et al corrected the rigid motion for an arbitrary coordinate system fixed to the object (Kim et al., 2015). During both forward and backward projections, they re-oriented the ray trajectories by altering the source-detector pairings. An iterative reconstruction algorithm does not use ramp filtering or pre-weighting like an FBP-type algorithm. This permits for compensating larger motions but often with long computation times due to the repetitive nature of the iterative algorithm.

3.5.1 Joint motion estimation and compensation

When the motion is known, the motion-compensated reconstruction is quite simple to execute. Another method for removing artifacts is to use a joint motion estimation and compensation procedure. Rohkohl et al. and Hahn et al. calculated non-rigid motion in a cardiac ROI and used an FDK reconstruction to adjust for it (Rohkohl et al., 2013, Hahn et al., 2017). The process was repeated for several iterations until a satisfying image was obtained.

3.6 Image-processing based methods

When the motion is unknown, an image-processing procedure can be used to fix it, directly targeting artifact-contaminated projections or images. Under the assumption of a simple motion

model, Lu et al. correct the observed data from a respiratory motion-contaminated scan (Lu et al., 2002).

The restored projections can then be reconstructed to an artifact-reduced image. Schretter et al. attempted to segment an artifacts-only image, by comparing the forward projections of an initial reconstructed image and the actual measured projections and reconstructing the differential projections (Schretter et al., 2009). The artifacts-only image can then be subtracted from the initial reconstructed image and the above procedure can be repeated multiple times. Marchant et al. tried to register the measured projections to the forward projections of the initial reconstructed image non-rigidly (Marchant et al., 2011). The registered projections were utilized to create an initial compensated image, which could then be iterated until a final compensated image was obtained. Due to the lack of precise motion information, all of the preceding image-processing algorithms frequently yield images with residual artifacts.

Chapter 4. 3D Iterative Data-Driven Motion Correction Algorithm

4.1 Motion estimation and compensation method

A c helical CT scanner typically has a cylindrical detector surface, having a radius equal to the source-detector distance. Here c is a world coordinate scheme and c = (x, y, z) ϵ R3 as in figure 4.1.

Which is fixed to the scanner and the z-axis coincides with the scanner's rotation axis.. c′ = (u, v, z) ϵ R3 where c′ represents the detector coordinate system, v is orthogonal to the detector and u is tangent. The origin of c′ moves along the z-axis while the system moves, and it is fixed to the rotating source-detector system. The rigid motion transforms (Sun et al., 2015) for one projection view in the coordinate system c can be defined as;

$$S_{world} = (\varphi_x, \varphi_y, \varphi_z, t_x, t_y, t_z)^T \quad (4.1)$$

Where three rotations are $\varphi_x, \varphi_y, \varphi_z$, while three translation parameters are t_x, t_y, t_z. The motion can be mapped in a detector coordinate system c′

$$S_{detector} = (\varphi_u, \varphi_v, \varphi_z, t_u, t_v, t_z)^T \quad (4.2)$$

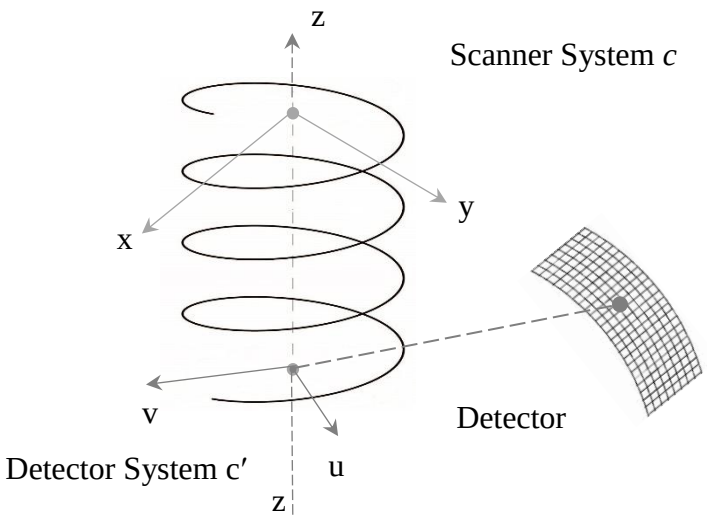

Figure 4.1: The scanner and detector scheme used for motion estimation and compensation (Sun et al., 2016).

A small magnification of the projection is created by a slight motion perpendicular to the detector in the t_v direction, which is supposed to be negligible (Gullberg et al., 1987). In the detector coordinate system for every projection, we take t_v as zero and estimate only five parameters. Equation 4.2 can be written as;

$$S_{detector} = (\varphi_u, \varphi_v, \varphi_z, t_u, t_z)^T \quad (4.3)$$

4.2 Motion correction method

A 3D registration of the object to each 2D view was accomplished individually to estimate the posture of the object for each acquired CT view. The initial rough estimate of the 3D subject is attained with a preliminary reconstruction without incorporating motion compensation. Therefore, motion artifacts in the initial image will have a significant impact on the accuracy of the posture estimates for each projection.

However, this 2D-3D registration process can still estimate the part of the real motion and enhance the reconstruction. This first rough motion estimation is used to create a motion-corrected image during the first iteration. Afterward, the iterative algorithm reiterates the process of reconstruction, generates more accurate motion estimates for each view, and alternatively compensates for the motion for each view, and the iteration process stopped when the reconstructed image is converged.

The algorithm is divided into two parts: the first portion grasps joint image and motion estimation (JIM), and the second part does the final reconstruction using motion compensation. A motion update and an image update are computed for each JIM iteration, with the image update obtained by using several iterations of the OSEM method (Sun et al., 2016).

For an iterative algorithm, computed projections are produced by employing a forward acquisition model on the current image estimate. This algorithm tries to consider the true interpretation of the object by imposing the data consistency among the computed projections and measured data numerically. Consequently, the image update is improved at every iteration. In contrast, in FBP a single step inversion is applied to images. To model physical processes during acquisition (noise, scattering, motion, etc.) the forward acquisition model algorithm is superior to an analytical inverse acquisition model. Therefore, motion-corrected CT reconstruction will be executed from motion-contaminated raw data by using OSEM iterative reconstruction (Hudson et al., 1994).

$$\mu_j^{k+1} = \frac{\mu_j^k}{\sum_{i \in Sb} a_{ij}} \sum_{i \in Sb} a_{ij} \frac{l_i}{\sum_h a_{ih}\mu_h^k} \quad (4.4)$$

In equation 4.4, Sb represents one subset (comprising b views) and l indicates the log converted sinogram. A modified version of conventional OSEM was used to enable motion correction (Sun et al., 2016):

$$T_{\theta}^{n+1} = invert(T_{\theta}^{n+1})$$

$$\mu_j^{n+1} = \frac{\mu_j^n}{\sum_i T_i^{n+1}(a_{ij})} \sum_i T_i^{n+1}(a_{ij}) \frac{m_i}{\sum_k T_i^{n+1}(a_{ij})\,\mu_j^n} \quad (4.5)$$

Thus, the execution includes four steps:

1. **A motion update**: this is a 2D-3D image registration that updates the pose estimation for every view in the present JIM iteration.
2. **An image update:** At the current JIM iteration, the new motion estimate was incorporated into the system matrix through an iterative reconstruction technique.
3. A multi-resolution scheme updates alternatively both image and motion.
4. The final reconstruction uses a system matrix derived from the final motion estimate.

4.2.1 Motion update

The posture of the object was estimated by the 3D registration of the object for every 2D projection. In the present JIM iteration, 2D-3D image registration was utilized to update the pose estimate for every view. The initial estimate of the 3D object was achieved by a preliminary reconstruction with no motion compensation. This 2D-3D registration detected a part of the real motion, and this motion estimate was helpful in the improvement of the further reconstruction process. The algorithm is executed in two parts, motion estimation, and motion compensation (Sun et al., 2016).

To develop the forward projection of the estimated image μ, we integrate along the projection line *i* at the current JIM iteration:

$$f_i = \sum_j a_{ij}\,\mu_j \quad (4.6)$$

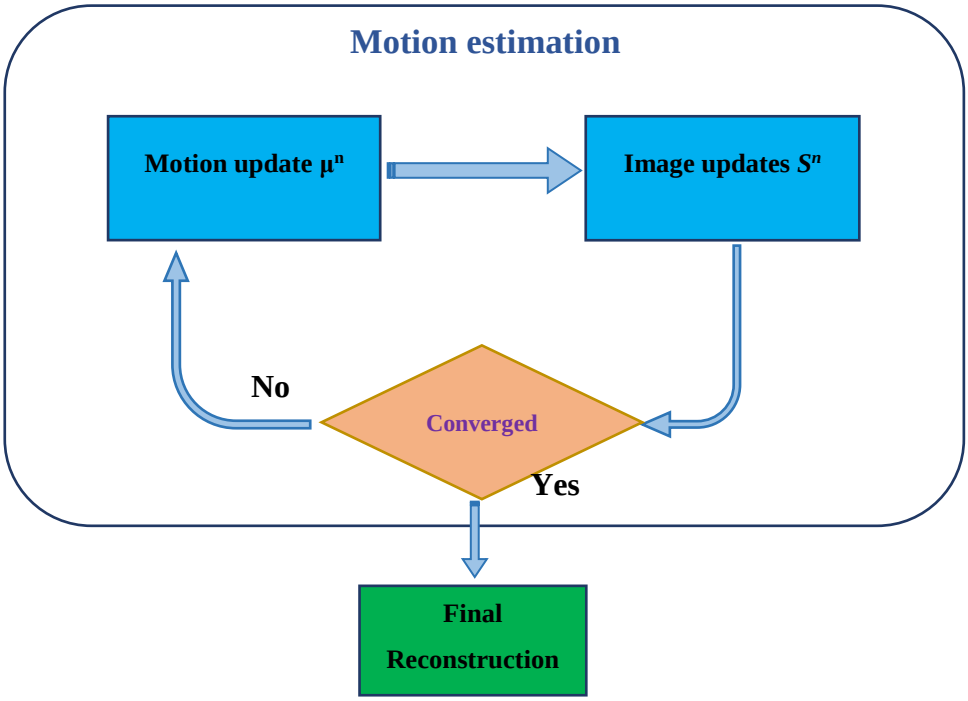

Figure 4.2: Schematic of motion estimation technique. μ is the update of the attenuation image, s is the update of the rigid transform, n is the iteration number (Sun et al., 2015).

In equation (4.6) i represents the projection line index and j the voxel index while a_{ij} is the effective intersection length of line i with voxel j. In helical CT, the line integrals are organized into views, with each view θ including all line integrals related to a single source position;

$$f_\theta = \{f_i\} \qquad (4.7)$$

Figure 4.2 depicts the general motion estimate and compensation technique. Let us suppose the motion correction is at the JIM-iteration n, therefore the present equation (4.3) motion estimate is s^n for θ view, the current pose estimate is s_θ^n and the 5 motion parameters are estimated one by one. Let s be one of these parameters (translation or rotation) be estimated. If the change in the pose parameter described by $\hat{s}$ is small, the derivative of projection f regarding $\hat{s}$ can be estimated as a finite variation of the intensities as;

$$\frac{\partial f_\theta}{\partial s} \approx \frac{f_\theta(\hat{s}) - f_\theta(s^n)}{\hat{s}} \qquad (4.8)$$

where $f_\theta(s^n)$ is the calculated re-projection by employing the current estimates of the image and motion, $f_\theta(\hat{s})$ is the measured projection for view θ. Therefore, to measure $\hat{s}$ the equation (4.8) can be written as (Sun et al., 2016);

$$\frac{\partial f_\theta}{\partial s} \approx \frac{f_\theta(\Delta s) - f_\theta(s^n)}{\Delta s} \qquad (4.9)$$

Where Δs is a small increment of the parameter to be approximated, if Δs is the translation parameter then $f_\theta(\Delta s)$ can be estimated as a simple translation of the current re-projection $f_\theta(s^n)$. If Δs is in-plane rotation, then $f_\theta(\Delta s)$ can be estimated as a simple rotation of the re-projection f_θ. For the two out-of-plane rotations, $f_\theta(\Delta s)$ computed with a forward projection utilizing a system matrix according to Δs (Sun et al., 2016).

We assume in equations (4.8) and (4.9) that a slight change in one degree of freedom of rigid movement only gives a linear change in the projection intensities. At the current JIM-iteration n, this leads to the least-squares minimization problem for view θ (Sun et al., 2015);

$$s^n_{incre} = \underbrace{\arg\min}_{\hat{s}} \|\Delta s \cdot [f_\theta(s^n + \hat{s}) - f_\theta(s^n)] - \hat{s} \cdot [f_\theta(s^n + \Delta s) - f_\theta(s^n)]\| \qquad (4.10)$$

To find s^n_{incre} the equation (4.10) is solved analytically by defining;

$$P_\theta = f_\theta(s^n + \hat{s}) - f_\theta(s^n) \qquad (4.11)$$

$$Q_\theta = f_\theta(s^n + \Delta s) - f_\theta(s^n) \qquad (4.12)$$

The derivative of the right-hand side of equation 4.10 with relation to $\hat{s}$ to zero;

$$s^n_{incre} = \frac{\sum_N P_{\theta.} \sum_N Q_\theta}{\|\sum_N Q_\theta^2\|} \Delta s \qquad (4.13)$$

The total number of voxels in the projection θ view is N. This method explains the estimation of one parameter in a single projection view. For all θ views, all five parameters are estimated by using this procedure in equation 4.3. The sequence of the estimation was a translation, then rotation. The recently estimated parameter values were employed instantly for estimating the value of the next parameter. As shown in figure 4.2, this sequential estimation of five motion parameters for all projection views accomplished the update of the rigid motion at the present JIM iteration (Sun et al., 2016).

In the detector coordinate system, the rigid motion parameters for every projection view were then translated into a homogeneous matrix. Because the reconstruction involves a

transformation in the world coordinate system, the estimated motion in the detector coordinate system was transformed into the motion in the world coordinate system (Sun et al., 2016):

$$S_{dectector} \rightarrow T_{detector}$$

$$T_{world} = R.\ T_{detector}$$

The homogenous matrix representation of the transform is the 4×4 matrix T, transformation matrix that maps the detector coordinate system to the world coordinate system is the 4×4 matrix *R*.

$$\{S_\theta^{n,inc} \rightarrow \Delta T_\theta^n\} \tag{4.14}$$

$$T_\theta^{n+1} = T_\theta^n \cdot \Delta T_\theta^n \tag{4.15}$$

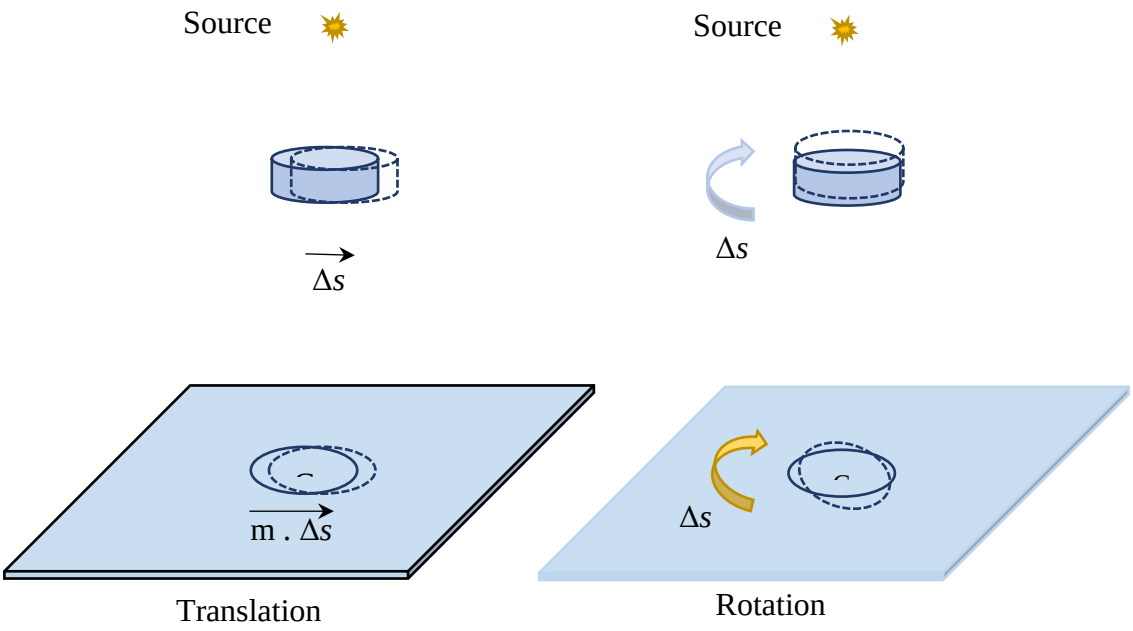

Figure 4.3: The impact of object rotation and translation parallel to the detector can be better approximated in the detector coordinate system as translation and rotation of the projection. m is the magnification factor from the object to the detector. For simplification, the curvature of the detector is omitted (Sun et al., 2015).

The transformation matrix attained in the n^{th} JIM-iteration was later utilized to update the prior motion estimate for each view, which was employed in the subsequent JIM-iteration (n + 1). Iterative reconstruction can be used to update the image representing the attenuation coefficients after the motion has been found.

4.2.2 Image update

A modified version of standard OSEM was used to enable motion correction (Sun et al., 2016):

$$T_i^{n+1} = invert(T_i^{n+1}) \tag{4.16}$$

$$\mu_j^{n+1} = \frac{\mu_j^n}{\sum_i T_i^{n+1}(a_{ij})} \sum_i T_i^{n+1}(a_{ij}) \frac{m_i}{\sum_k T_i^{n+1}(a_{ij})\, \mu_j^n} \tag{4.37}$$

Where *aij* is the effective intersection length of line *i* with voxel *j*, *i* is the projection line index, *j* is the voxel index, *Sb* is one subset consisting of b projections and T_i is the 4×4 transformation matrix applied to the projection line *I*, and m is the log converted sinogram. The above equation will be comparable to standard OSEM if T_i is the identity matrix for all projection lines. For the helical CT, T_i is constant for all projection lines in one projection view, hence the inversion is done for every single view. The motion within a single view is insignificant due to the rapid rotation speed and a vast number of views.

4.2.3 Multi-resolution alternate update scheme

The problem of error propagation is mitigated since the image and motion parameters are estimated from the measured data jointly. A multi-resolution system was utilized to accelerate the convergence of the joint estimation of the motion and image update (Sun et al., 2015). The algorithm proceeded from a coarse to a fine image representation. The initial image resolution level is 8 ×8 × 8, i.e. which means that an eight-fold down-sampling factor was used in all directions **(**Sun et al., 2015). Early JIM-iterations reconstructed image updates at a coarse resolution, with the resolution increasing as the number of iterations amplified. The number of OSEM-iterations performed for the image update was similar within one resolution level.

4.2.4 Final reconstruction

From the last motion estimate, a final iterative reconstruction was completed. Due to the large volume of the raw data set, a motion was assessed at each 8th projection to speed up both motion and image updates. To get rid of outliers, a Savitzky-Golay filter was used to smooth motion updates (Savitzky et al., 1964). It was not clear where to stop iteration during estimating the movement at every resolution level. For all projects, the sum of projection errors (PE) between re-projected and measured data was calculated. It was decided that the iterations would be halted when the PE did not exceed 0.2 % for each resolution level.

The appropriate smoothing kernel size is determined by the axial detector extent as well as the view sampling rate of the measured data. The axial extent varies depending on the scan configuration. A final diagnostic quality reconstruction must be generated after the motion estimate has converged. To accelerate reconstruction, the final reconstruction from an approximate helical FDK reconstruction (motion correction was enabled in the back-projection step), provided the image is not affected much by the motion artifacts. The forward and backward projection operations were applied in OpenCL (Sun et al., 2016) and executed on a GPU to further speed up the final reconstructions (NIVIDIA Tesla C2075).

4.2.5 Data-sufficiency

A precondition for an exact reconstruction is the data-sufficiency condition. Before designing a reconstruction algorithm for a specific imaging application, it is useful to determine whether the available data are sufficient for the exact reconstruction of the attenuating object. Here, exact reconstruction means that the reconstruction problem has a unique solution, and a stable estimate of that solution can be computed from noisy data. In parallel-beam tomography, Orlov developed a data-sufficiency criterion (Orlov et al., 1975). In cone-beam tomography, Tuy expanded it to a data-sufficiency condition (Tuy et al., 1983). Later, Metzler et al. described the geometrical equivalence between Orlov's and Tuy's sufficiency conditions (Metzler et al., 2003). Note that the above conditions assume that all projections at all source positions are not truncated, i.e. all projection lines that intersect the object also intersect the detector.

Chapter 5. Validation of 3D iterative data-driven motion correction algorithm

5.1 Introduction

Patient motion, is a primary source of artifacts in clinical x-ray computed tomography because it generates inconsistencies in the acquired projection data. Head motion during head CT imaging can have severe effects on image resolution and originate distortion and other related artifacts (Rachel et al., 2013).

Motion artifacts come out as dark or bright shadowing and shape distortion that sometimes looks like a disease. There are two types of motion-related artifacts like voluntary motion and involuntary motion (Barrett et al., 2004). The voluntary motion included external body movement, respiration, and swallowing. The beating heart, coughing, and peristalsis, sneezing are involuntary movements.

In 1995, G. Wang published a study on helical CT methods for patient motion estimation and compensation (Wang et al., 1995). In 1998, different possibilities were considered Ritchie et al. studied scan speed to reduce motion artifacts, but they concluded an ultrafast scan time cannot reduce the motion artifacts. Therefore, they suggested the need for the development of other techniques to minimize motion artifacts.

When imaging children, as well as patients suffering dementia or head trauma a method of compensating for head motion in helical CT, would be of substantial benefit. To compensate for head motion, several retrospective motion correction algorithms have been developed (Schäfer et al., 2004, Wang et al., 2007). All of these use the information about the motion of the head in the CT coordinate system in the CT scan. Several studies have also proposed approaches for motion estimation from the acquired projection data (Yu et al., 2007). The existing motion estimation methods (Bodensteiner et al., 2007, Bhowmik et al., 2012), can offer 6 degrees of freedom (d.o.f.) motion estimates in CT coordinates. The method proposed by Wagner did not evaluate the quantitative accuracy of derived motion estimates. His technique might potentially be adapted to provide estimates directly in CT coordinates, using the information of bed position, and is a possible alternative to the technique explained here (Wagner et al., 2003).

The object dislocations of roughly 1-pixel width can originate in considerable image artifacts (Jacobson et al., 2008). These estimates are dependent on several factors, like the geometry of the scanner, the number of projection angles employed in the image reconstruction, the track of motion, the extent and attenuation of the entity, and the application of motion-decline reconstruction algorithms. In this work, they studied the degree of motion artifacts on test phantoms by varying velocities.

Bhowmik used radio-opaque markers in each projection to compute motion estimates in cone-beam CT (Bhowmik et al., 2012). In a similar study, Bodensteiner et al. evaluated artifacts caused by positioning errors in CT images acquired by mobile C-arm systems. They suggested 2D/3D registration technique to compensate for projection data discrepancies and an iterative 3D-reconstruction technique. This algorithm with 3D reconstructions decreases the small motion artifacts.

Feldkamp-Davis-Kress (FDK) supported 3D cone-beam brain imaging technique, using markers to curtail motion artifacts (Hengyong et al., 2007). Motion-related artifacts could also be alleviated by using a customized form of the FDK algorithm (Westermann et al., 2000).

Another interesting method (Katsevich et al., 2011) uses an empirical measure of image clutter called edge entropy to assess local motion in cardiac imaging. As local motion estimation is a more difficult problem than rigid motion estimation, it is probable to adapt this technique to rigid motion.

Our goal is to validate the data-driven rigid head motion correction method in CT. The validation of a data-driven 3D iterative motion correction algorithm will be performed on brain phantom as well as patient scans.

5.2 Phantom studies

A tissue-equivalent material to mimic the human body is known as a phantom. Phantoms are used to do experimentation for research as a human being cannot be used in the experiment. The Hoffman 3D brain phantom provides a quantitative and qualitative study of the three-dimensional effects of scatter and attenuation similar to the human brain. Nineteen independent plates stack within the cylindrical phantom for easy disassembly and assembly. This phantom represents a whole brain, both white and gray matter. It consists of a single fillable chamber.

Figure 5.1: Hoffman brain phantom.

5.3 Hoffman brain phantom

Acquisition of Hoffman brain phantoms on CT

Hoffman's brain phantom was scanned on a Siemens Biograph mCT scanner with a 128 slice CT system (Siemens Medical Solutions USA, Inc., Malvern, PA) using routine head CT. The acquisition and reconstruction parameters of the phantom scan are listed in table 4.1. The 3D Hoffman brain phantom in CT imaging experiments was filled with water.

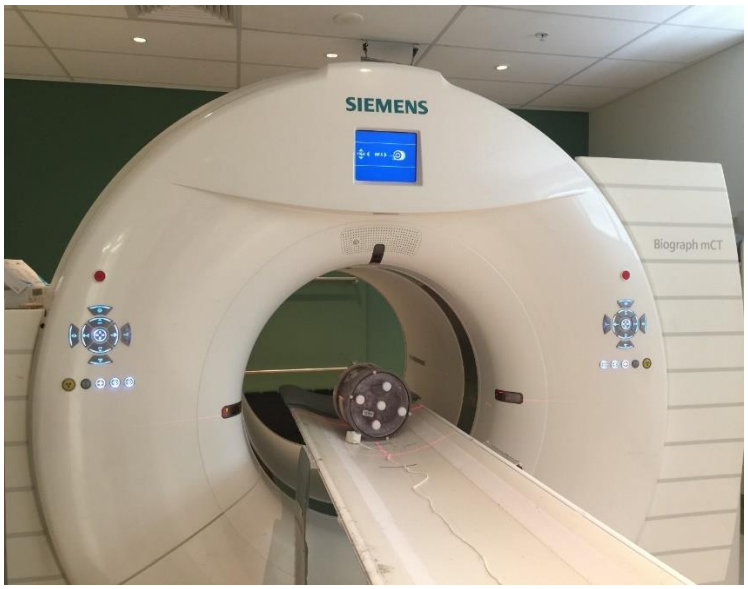

Figure 5.2: Hoffman brain phantom acquisition on Biograph mCT.

Table 5.1: Acquisition and reconstruction protocol for Hoffman brain phantom

Parameters	**Values**
Detectors rows	128
kVp	120
mAs	44
Pitch	0.5
Collimation	128 × 0.6
Slice thickness	2 mm
Rotation time	0.5 sec
Rebinned projection	1600

The phantom was placed on the patient's couch, elevated on the curved surface of the bed, and supported by a wedge. The phantom was scanned with a reference stationary helical CT scan. Afterward, a series of CT scans were acquired with a variety of motions, without moving the phantom. The variety of motion was generated when a string was pulled from outside the room. The following phantom scans were acquired;

a. Stationary
b. Slight motion (SM)
c. Moderate motion (MM)
d. Fast motion (FM)

Stationary phantom scan: The Hoffman phantom was positioned using a LASER marker at the center and the phantom was supported by a wedge. A reference stationary scan was acquired using routine head CT acquisition as listed in table 4.1.

Moving phantom scans: Without changing the position of the phantom as well as acquisition parameters the phantom scans were acquired with a variety of motion b-d as mentioned above.

Phantom analysis: The effect of motion correction on phantom CT scans was evaluated by separately comparing the gold standard stationary phantom images with corresponding uncorrected and motion-corrected images as illustrated in figure 5.3.

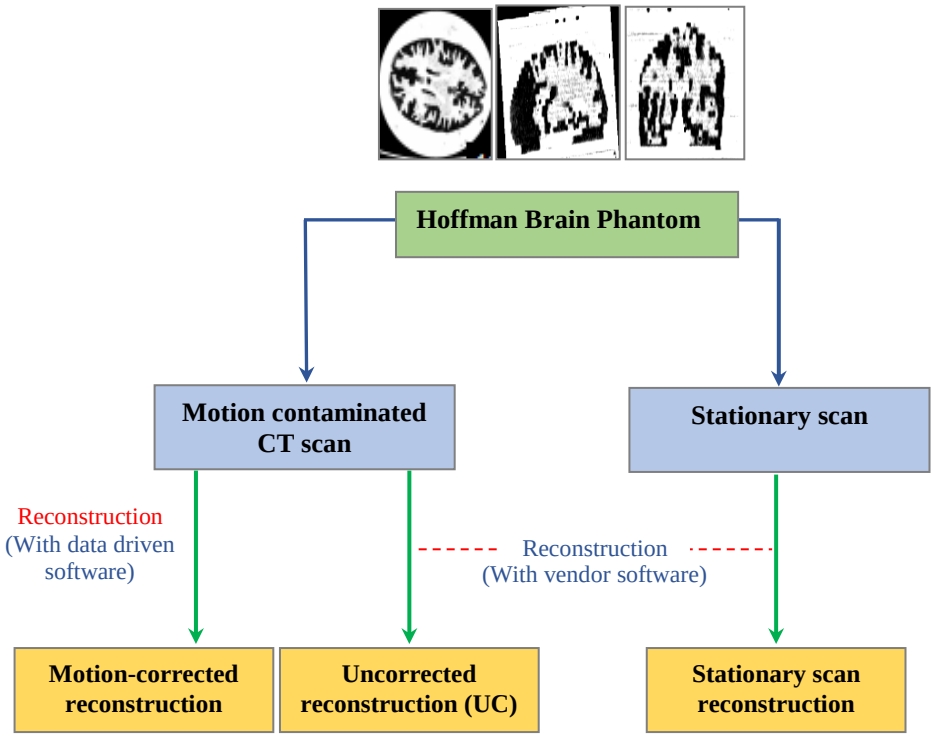

Figure 5.3: Hoffman brain phantom analysis (Kim et al., 2016). The motion-induced phantom scans were reconstructed with and without a motion correction and compared with a reconstructed stationary phantom scan.

5.4 Clinical studies

For clinical studies, 3D iterative data-driven motion correction algorithm will be used to reduce motion artifacts in diagnostic helical CT by estimating motion from raw x-ray projection from the human head. During the image reconstruction process, the planned motion estimation and compensation technique using only the measured x-ray raw data to iteratively estimate and compensate the human head movement. Our next objective is to evaluate this approach in inpatient studies and to improve it for more robust applications.

5.4.1 Data collection

The raw data of fifteen patients presenting head movement during CT acquisition has been acquired at the radiology department at children hospital Westmead and Westmead hospital, Sydney, Australia. The study had been started with the authorization of the human research ethics committees of the Western Sydney health district. CT studies of the head were acquired for a range of clinical indications on a Siemens Sensation 64 system, Siemens Definition AS,

and Siemens Somatom Force scanners at these institutions (Siemens Medical Solutions USA, Inc., Malvern, PA).

5.4.2 Motion estimation and compensation scheme

CT image reconstruction is a mathematical procedure that creates tomographic images from x-ray projection data acquired from a variety of angles around the patient. Iterative reconstruction has the potential to improve image quality while also lowering radiation exposure. Images from iterative reconstruction (IR) may have a different appearance (e.g., noise texture) than those from FBP reconstruction due to the inherent differences in data handling between FBP and IR. More crucially, due to the non-linear regularization term and other factors during the optimization process, the spatial resolution in a local region of IR-reconstructed images is highly dependent on the contrast and noise of the surrounding structures.

With advancements in computing technology, IR has become a common alternative in everyday CT practice due to its several advantages over traditional FBP procedures. When compared to FBP, important physical characteristics like focus spot and detector geometry, photon statistics, x-ray beam spectrum, and scattering may be more precisely included in IR, resulting in lower image noise and improved spatial resolution. In addition, image artifacts like beam hardening, windmill, and metal artifacts can be reduced using IR.

For an iterative algorithm, computed projections are produced by employing a forward acquisition model on the current image estimate. The iterative algorithm tries to consider the true interpretation of the object by imposing the data consistency among the computed projections and measured data numerically. Consequently, the image update is improved at every iteration. In contrast, in FBP a single step inversion is applied to images. To model physical phenomena during acquisition (noise, scattering, motion, etc.) the forward model algorithm is superior to an analytical inverse model. Therefore, motion-corrected CT reconstruction will be executed from motion-contaminated raw data by using OSEM iterative reconstruction (Hudson et al., 1994).

$$\mu_j^{k+1} = \frac{\mu_j^k}{\sum_{i \in Sb} a_{ij}} \quad \sum_{i \in Sb} a_{ij} \quad \frac{l_i}{\sum_h a_{ih} \mu_h^k} \tag{5.1}$$

In equation 5.1, Sb represents one subset (comprising b views) and l indicates the log converted sinogram. Motion correction was enabled by using a customized version of standard OSEM (Sun et al., 2016);

$$T_{\theta}^{n+1} = invert(T_{\theta}^{n+1})$$

$$\mu_j^{n+1} = \frac{\mu_j^n}{\sum_i T_i^{n+1}(a_{ij})} \sum_i T_i^{n+1}\left(a_{ij}\right) \frac{m_i}{\sum_k T_i^{n+1}(a_{ij})\,\mu_j^n} \tag{5.2}$$

In the first step of reconstruction, a 3D object estimation is achieved by initial reconstruction, not including motion compensation. In the motion correction method, it is assumed that all in the CT system field of view moved rigidly except the patient headrest and couch. Therefore, patient headrest and couch segments were deleted from the raw data preceding reconstruction after the completion of the first step (Fig. 1). In the second step, a new set of projections was generated through forward projection from this new segmented data. These new projections were then deducted from the measured projections prior to the motion estimation and compensation was implemented.

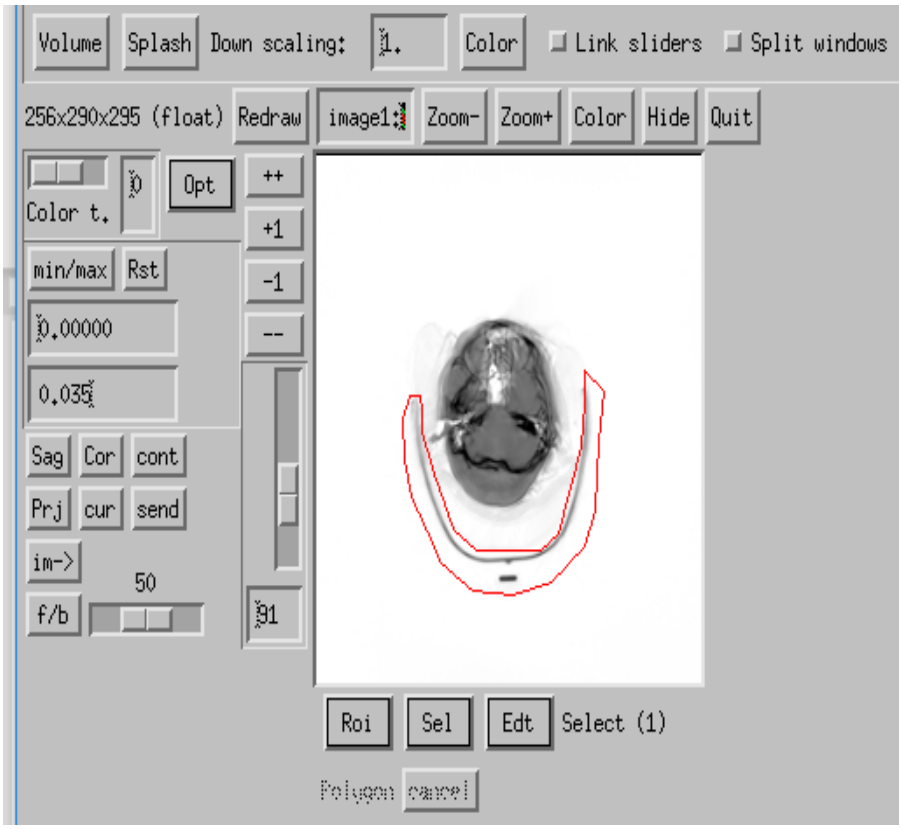

Figure 5.4: ROI for removal of patient headrest and couch from raw data before motion estimation.

It is assumed that the pose of the measured object might be unique for every projection. As a result, a rigid transformation inferring the object posture is calculated for each projection and used to update the system matrix. The whole framework was executed in four parts, a multi-resolution approach was utilized to accelerate the convergence of the joint estimation of the motion and image update (Sun et al., 2016). Using the most current motion estimate, a final iterative reconstruction was completed. Due to the large volume of the raw data set, the motion was assessed at each 8th projection to speed up both motion and image updates. To get rid of outliers, a Savitzky-Golay filter was used to smooth motion updates (Savitzky et al., 1964). It was not clear where to stop iteration during estimating the motion at every resolution level. The sum of projection errors (PE) between the re-projected and measured data for all projections was calculated. It was decided that the iterations would be halted when the PE did not surpass 0.2 % for each resolution level.

5.4.3 Scoring of images

All the patient scans were reconstructed with standard algorithm configuration. After reconstruction images were analyzed for removal of motion artifacts by comparing

reconstructions with and without motion correction. The image data sets were independently assessed by two blinded radiologists and scored on a 4-point scale, (dramatically better = 3, much better = 2, negligible better = 1, and no improvement = 0). The scoring criteria were designed according to the European Commission guidelines on quality criteria for CT images (Bongartz et al., 1999, Zue et al., 2012).

5.5 Results

The phantom scans were acquired with a 128 detector row CT system, but the patient studies were scanned with a 64-row, 96-row, and 128-row CT. The data-driven motion estimation and compensation worked effectively for data from systems having different numbers of detector rows. The performance of the algorithm was improved with a large number of detector rows, as the broader detector delivers more data in a single projection view. To reduce the noise of the predicted movement, stronger smoothing was required for data from a system with a narrower detector.

The degree of motion was arbitrarily classified into six parameters three rotation parameters Rx, Ry, Rz, and three translational parameters Tx, Ty, and Tz. Although the motion is complex and always affects two or more of the six parameters concurrently in different manners, the weighting between rotation and translation is not unrealistic as a technique of expressing the degree of motion with a single parameter, because rotation may happen around any place between the center and a margin of the brain.

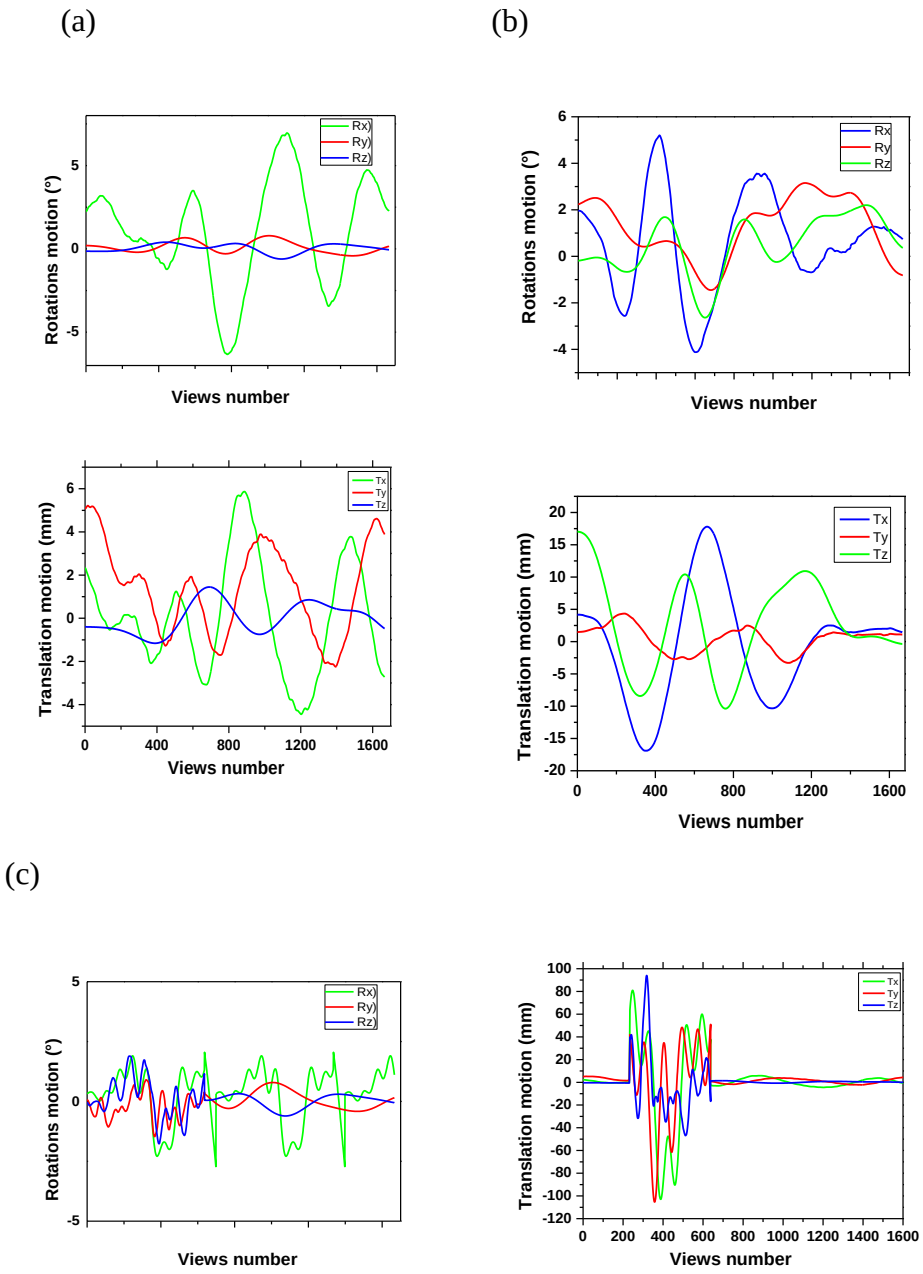

Figure 5.5: Motion of Hoffman brain phantom rotation motion (°) and translation motion (mm) of the phantom in CT isocentre coordinates, concerning its pose at the start of the scan. This figure explains the nature of the motion, which is intricate motion in all six DoF, (a) slight motion, (b) moderate motion, (c) fast motion.

Wagner et al. recorded motion in 20 patients during helical CT scans, with rotations of up to 2.3° and translations of up to 5 mm, which was substantially larger than what is generally expected in patients (Shefer et al., 2013). However, we expected that some individuals would experience the motion of the magnitude tested here. Fahmi et al., for example, recorded translations of more than 60 mm during helical CT perfusion scans in patients with acute ischemic stroke (Fahmi et al., 2013).

The phantom scans with SM and MM were reconstructed without artifacts, but with FM some residual artifacts were seen after motion correction had been executed. It has been seen that these artifacts were due to data insufficiency, A fast-rolling motion of a cylindrical phantom can produce artifacts that motion correction cannot completely remove, as demonstrated in figure 5.6. These massive motions are not clinically expected in human scans. This leads to the important question of whether the approach would produce similar residual artifacts when used in clinical scanning.

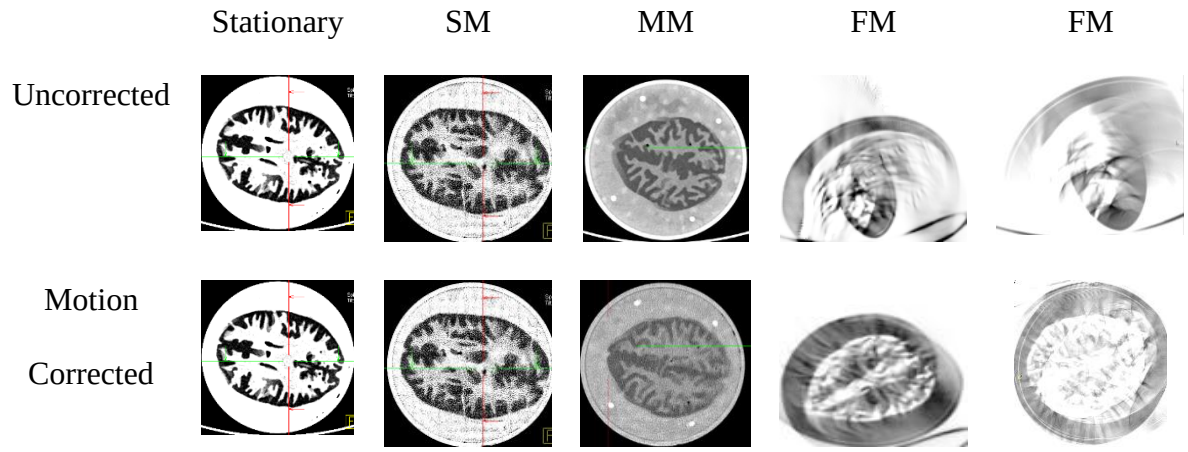

Figure 5.6: Comparison of axial reconstructed slices from the moving phantom uncorrected and motion-corrected, (a) stationary phantom, (b) slight motion, (c) moderate motion, (d-e) fast motion.

5.6 Discussion

The overall resolution of the Hoffman brain phantom image was deprived. One possible explanation is that the proposed method is based on 2D to 3D image registration, which is likely to be less effective when the object contrast is low. The high contrast between the skull and soft tissue was determined to give sufficient information for calculating motion in CT brain imaging. But the Hoffman brain phantom did not have skull bones so due to low contrast the quality of the image is poor. Preprocessing to improve the contrast of the raw projection data may be required for situations where the contrast is poor.

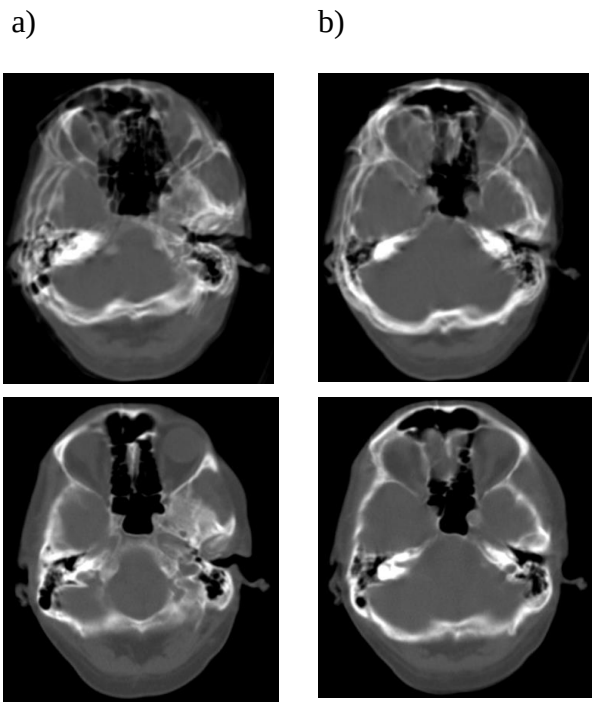

Figure 5.7: A 58-year-old man's head CT scan, two different CT scan slices are shown, (a-b) the top row is original scan slices with motion, bottom row is motion-corrected.

Clinical scans with a significantly large number of CT views imposed a computational problem. It takes around 2 hours to estimate motion for a single patient scan, and about 12 hours to complete the final iterative reconstruction (a good number of updates is essential to obtain a quality similar to the vendor images). The multi-resolution technique accelerated the motion estimation. Excessive blurring can obscure critical high-frequency features, hence using a coarse beginning resolution should be discouraged.

Among the six co-registration parameters, Z-axis translation, Y-axis translation, and X-axis rotation (and sometimes Z-axis rotation) tended to present larger values than the other parameters. Axial translation (creeping up or down) and flexion-extension are the major types of motion (nodding or looking up). In the six registration parameters, these major kinds of motion tend to accompany Y-axis translation. The most head holds and fixation techniques do not prevent these forms of movements from occurring due to tension and relaxation of cervical muscles. The shaking head (Z-axis rotation) motion is likewise difficult to control and may occur when the individual is distressed. Motion correction has a quantitative effect that is dependent on the region and amount of motion.

As presented in figure 5.7, the proposed technique performed well even when the patient's motion was relatively large. With data-driven motion estimation and correction, 65% of the patient scans became dramatically better, 14% of the scans much better, 11% negligibly better and 5% of the scans demonstrated no improvement. It was determined that the method worked better when the rotation amplitude was less than 10^{o} and the translation amplitude was less than 30 mm, which we believe are unlikely to be surpassed in most clinical scans. However, in circumstances of extreme motion, such as that seen in figure 5.6 e, it did not produce motion-free images. Optical motion tracking systems have already been proved to be successful, even for very severe motion, by our group (Kim et al., 2016, Sun et al., 2016).

a) Uncorrected b) Motion corrected

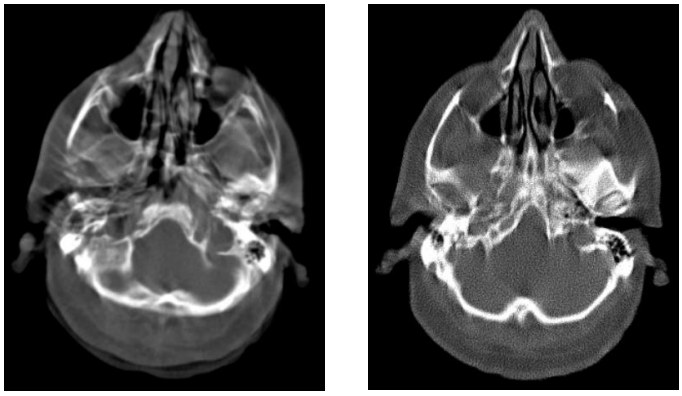

Figure 5.8: A male patient sneeze during a CT scan a) uncorrected axial slices and b) motion-corrected slices reveal the improvement in image quality.

Finally, by reducing the need for repeated scans in the event of motion, an effective and usable motion correction solution could expedite clinical procedures. The majority of diagnostic CT scans of the head are done at a low pitch (e.g. 0.5), which reduces the risk of artifacts.

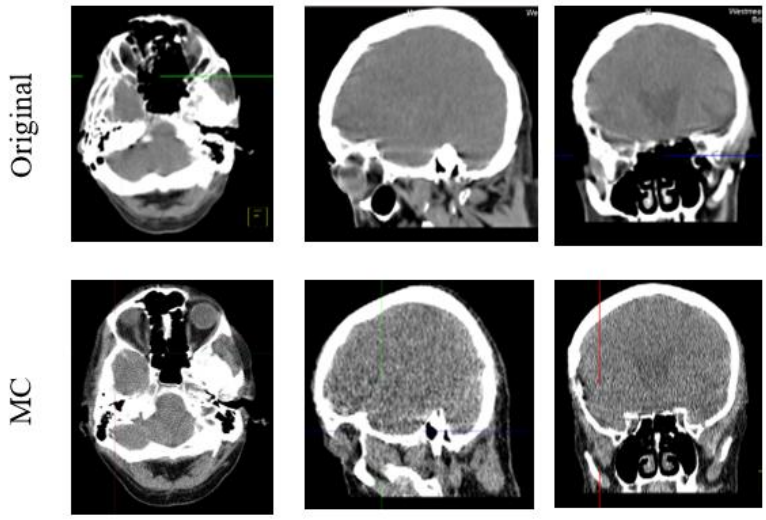

Figure 5.9: Selected transaxial, sagittal, and coronal planes, with and without compensation for residual motion. Top: original image; bottom: motion-corrected image

With most types of head motion expected to be encountered in CT imaging, our approach can give accurate and artifact-free MC images. The sole input required for the data-driven motion estimate and compensation method for helical x-ray CT of the head is measured raw data; no supplementary measurements are necessary. Therefore, it can be employed retrospectively to standard helical CT data. It will become a significant clinical tool and reduce the number of repeat scans if it is sufficiently accelerated.

Chapter 6. Optimization

In this chapter, we will optimize the data-driven 3D iterative motion estimation (ME) and motion compensation (MC) algorithm for its robust application in patient scan with head movements during computed tomography (CT).

6.1 Introduction

CT is an essential diagnostic technique in medicine. Computed Tomography (CT) scanning is commonly available, cost-effective, and provides higher sensitivity for the evaluation of skull fracture, calcification, and acute hemorrhage (Raj at el., 2014). Generally, CT motion artifacts are due to voluntary and involuntary actions like head motion, cardiac motion, and respiratory motion (Yazdi et al., 2008). In CT brain perfusion imaging of acute ischemic stroke patients, head motion is also highly common (Barrett et al., 2004). Furthermore, during scanning, seriously injured patients or small children frequently move, resulting in motion artifacts (Barrett et al., 2004). Children must often be anesthetized, which is accompanied by some risk, if the patient moves during the scan the motion artifacts can cause false diagnosis or severe movement deliver distorted images that are inappropriate for diagnosis. For these patients, scanning needs to be repeated resulting high undesirable radiation burden to the patient (Boone et al., 2012). The ability to compensate for head motion would reduce the need for repeated scans and deliver artifact-free images in CT, SPECT/CT, and PET/CT images. Motion artifacts might also be reduced by faster scanning and employing immobilization devices (Beyer et al., 2005).

Motion correction methods can be classified into two categories. The first group requires the motion acquisition data, such as surrogate signals or reference images to derive motion information, and motion is compensated during the reconstruction process. The second method compensates for motion without prior information about the motion using image-processing techniques. Rigid motion correction in helical CT scan is complicated as the object is continually truncated from the axial side which provides limited data to restore the consistency in projections. A comparatively, small number of studies already performed motion correction in helical CT scanning, and a few of these studies need supplementary measurement to acquire the motion information (Kyme et al., 2014, Sun et al., 2016).

In the current study, a data-driven fully 3D automatic reconstruction approach will be used to eliminate MA in helical CT imaging. This technique only needs the measured raw data and during the iterative reconstruction procedure estimate and compensates the motion. The

standard data-driven 3D iterative motion estimation and compensation technique effectively removed head MA in various scans. But in a few patient scans after MC, it was observed that some scans still have residual motion artifacts. To make motion correction robust, it is intended to investigate each shortfall that has a significant impact on ME and MC. It was identified that SK length, PT threshold, and AR can affect the performance of the algorithm. Therefore, we decided to optimize the SK length, PT threshold, and AR to eliminate residual artifacts in head CT scans using a data-driven motion correction approach.

6.2 Material and methods

The raw data of fifteen anonymized patients presenting head movement during CT acquisition at the Radiology department at children hospital Westmead and Westmead hospital, Sydney, Australia were collected. The study had been started with the approval of the human research ethics committees of the Western Sydney health district. CT studies of the head were acquired for a range of clinical indications on a Siemens Sensation 64 scanner, Siemens Definition AS, and Siemens Somatom Force scanners at these institutions (Siemens Medical Solutions USA, Inc., Malvern, PA).

The data of each patient was reconstructed by fully automated data-driven 3D iterative image reconstruction with motion compensation with various smoothing kernel (SK) lengths, projection tolerance (PT), and angle rebin (AR) to remove residual motion artifacts (MA) in the head CT. All reconstructed MC images were scored.

6.3 Smoothing kernel (SK)

The scans with residual artifacts were reconstructed by using four different SK values SK 60, SK 120, SK 230, and SK 320. Motion estimation and projection error were plotted against each projection angle for all SK values to analyze their impact on motion correction.

6.4 Projection tolerance (PT)

The change in the summation of PE among the re-projected and measured data for all views at every resolution level from each iteration to the next was computed. Projection tolerance is a stopping criterion**,** when the percentage change in PE among two consecutive iterations is less than the PT, the algorithm stops iterating at the current resolution level and selects the next resolution level. When estimating the motion at each resolution level, it was not clear when to stop iteration, as no motion-free image was available for these clinical studies. To analyze the impact of the number of iterations for each patient study was reconstructed with a fixed value of smoothing kernel SK 60 and changing projection tolerance PT 0.001, PT 0.0015, PT 0.0018,

PT 0.0025, and PT 0.005. Motion estimation was plotted against each projection angle for all PT values.

6.5 Angle rebin (AR)

Head scans have a large number of views approximately between 45,000 to 50,000. Projections were rebinnd by summing groups of 8, 16, and 32 consecutive projections to speed up reconstruction.

6.6 Scoring of images

All the patient scans were reconstructed with standard algorithm configuration. After reconstruction images were analyzed for removal of motion artifacts by comparing reconstructions with and without motion correction. The image data sets were independently assessed by two blinded radiologists and scored on a 5-point scale (best (no MA in entire scan) = 4, more than average (one MA) = 3, average (two MA) = 2, fair (partial motion correction) = 1 and worst (no motion correction) = 0). The scoring criteria were designed according to the European regulations on quality criteria for CT images (Bongartz et al., 1999, Zue et al., 2012). The scans with residual artifacts and receiving scores between 0-3 were reconstructed again by employing different SK, PT, and AR values and scored again.

6.6.1 Statistical analysis

The statistical analysis was done by using SPSS version 23.0 (SPSS, Inc., Chicago, IL). The quantitative mean scoring of reconstruction was evaluated using Wilcoxon sign-rank test and the differences were considered significant at $P < 0.05$. The Wilcoxon sign-rank test checks whether the mean values of two dependent groups differ significantly from each other. The Wilcoxon test is non-parametric, and it is utilized to evaluate mean scores when the dependent variable is not normally distributed.

6.7 Results

The accumulative head movement was quantified with a mean rotation angle up to ± 4.0° with a maximum 13.0° and mean translation up to ±21 mm with a maximum 54.4 mm. The most common motion was observed in the T_Z translation direction. The standard data-driven 3D iterative motion estimation and compensation scheme effectively removed head MA in various scans. But in a few patient scans after MC, it was observed that some scans still have residual motion artifacts. Figure 6.1 represents a patient scan reconstructed by the data-driven fully 3D iterative algorithm and compared with the real image without motion correction with the manufacturer´s reconstruction, figure 6.1b images improved after MC but presented a small

residual error. To eliminate these residual artifacts scans were reconstructed by using different smoothing kernel lengths, projection tolerance, and angle rebin.

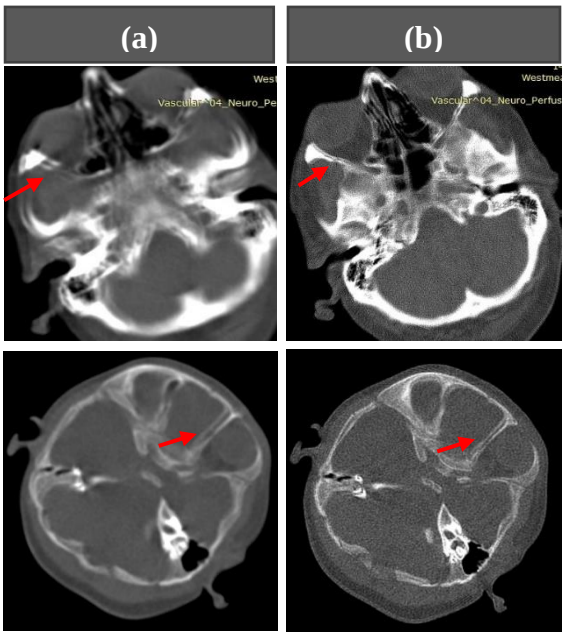

Figure 6.1: (a) Image reconstructed with Siemens software without motion correction, the arrow pointing ghosting, (b) image reconstructed with 3D iterative data-driven motion correction approach.

6.7.1 Smoothing kernel

The mean scoring was calculated for all patient scans reconstructed employing different SK values. Generally, the images reconstructed by SK 60 have got the highest mean score and offer more promising results, and are acceptable for reporting. Furthermore, in some cases, it has been observed that the SK 120 also offers comparable results to SK 60 and the images reconstructed with SK 320 and higher did not produce significant motion correction in the images. Figure 6.2, figure 6.3, and figure 6.4 indicate patient scans reconstructed by the data-driven iterative algorithm using SK 60, SK 120, SK 230, SK 320 and compared with real images reconstructed by using manufacturer software without motion correction. It is clear from figure 6.2b, figure 6.3b, and figure 6.4b ghosting in the images was successfully removed by using SK60.

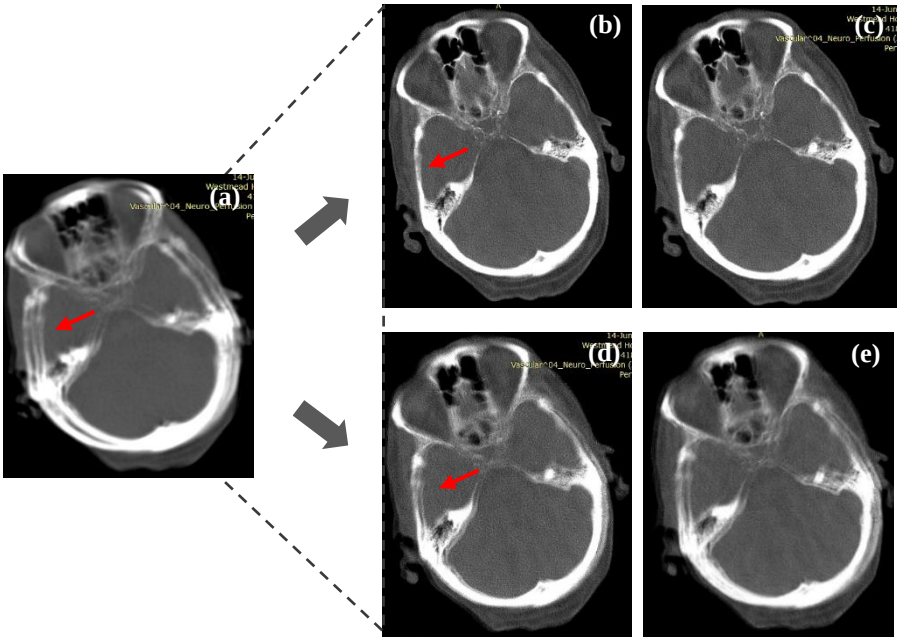

Figure 6.2: (a) Real image reconstructed with Siemens software without motion correction, the arrow pointing ghosting (skull to appear in 3 locations), (b) iterative image reconstruction with data-driven motion correction using smoothing kernel 60, (c-e) iterative image reconstruction with data-driven using SK120, SK 230, and SK 320, respectively. Ghosting was almost completely corrected in (b), but the correction was less complete in (c-e).

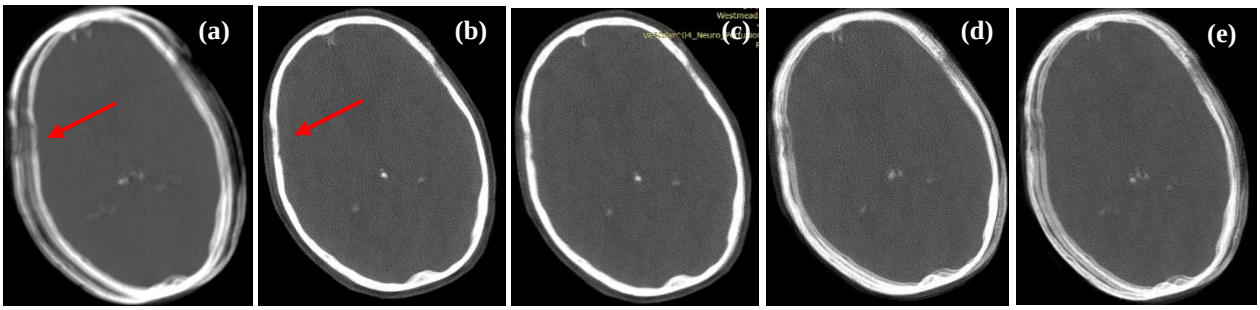

Figure 6.3: (a) Real image reconstructed with Siemens software without motion-correction, the arrow pointing ghosting (skull to appear in multiple locations), (b) iterative image reconstruction with data-driven motion correction using smoothing kernel 60, (c-e) iterative image reconstruction with data-driven using SK 120, SK 230, and SK 320, respectively. MA was almost completely corrected in (b), but the correction was less complete in (c-e).

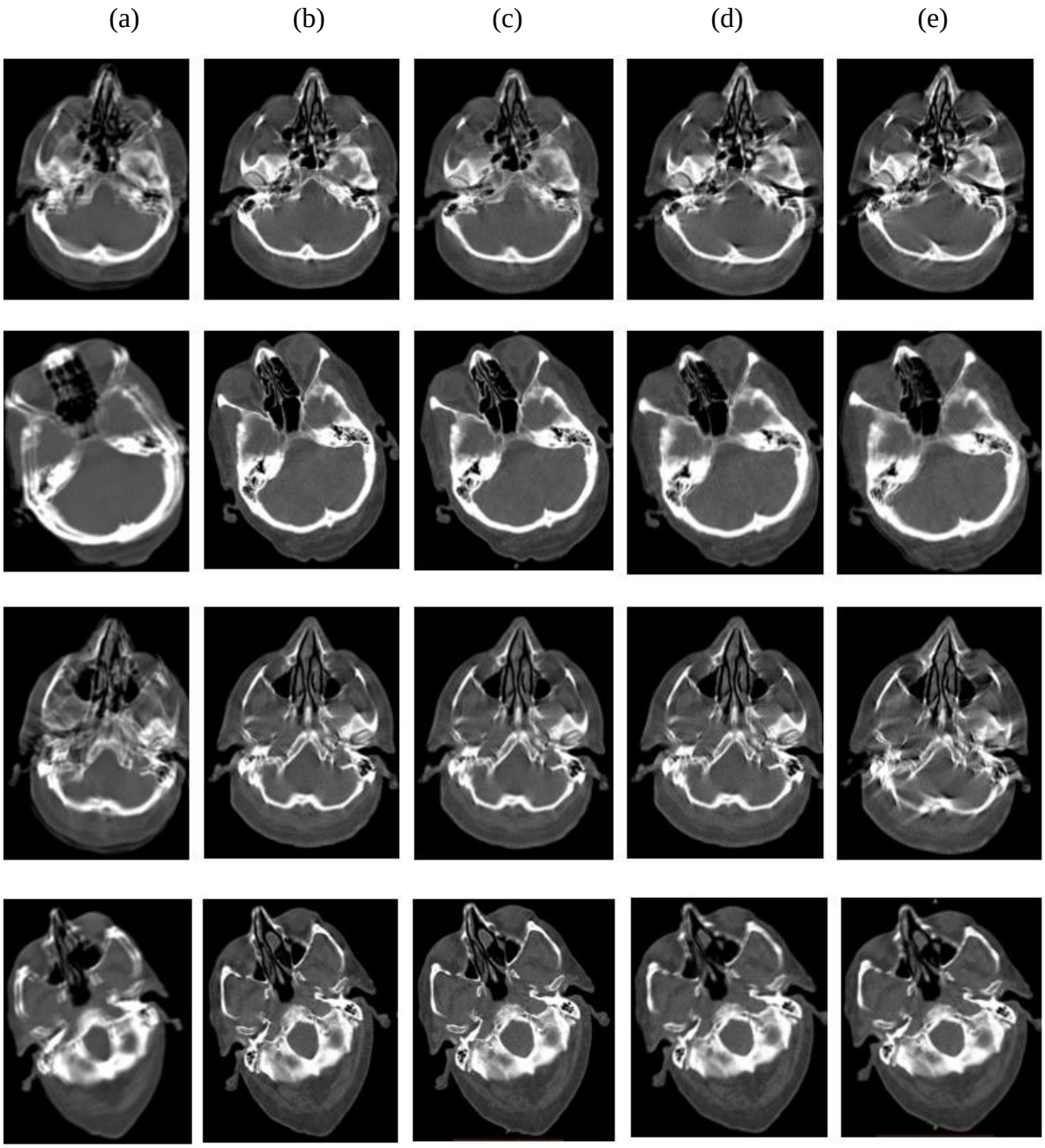

Figure 6.4: Column (a) various patient scans demonstrating MA with vendor reconstruction without motion correction, column (b-e) iterative image reconstruction with data-driven motion correction SK 60, SK 120, SK 230, and SK 320 respectively, MA was nearly completely corrected in column (b).

The degree of motion was determined for the 6 motion parameters, three rotation parameters Rx, Ry, Rz, and three translation parameters Tx, Ty, Tz. Certainly, precise motion estimation is crucial for motion compensation. Thus, it is very important to select the suitable length of the smoothing kernel. Our experiment reveals that SK 60 generates more satisfactory images, as the value of SK increases the motion estimation becomes smoother as shown in figure 6.5.

It is evident that motion estimation with different lengths of smoothing kernel is considerably different. PE drop with the increase in the number of iterations for different smoothing kernel lengths as presented in figure 6.6.

6.7.2 Projection tolerance

After the optimization of the smoothing kernel, we observed that in a few patient scans, the residual artifact is still present after motion compensation. To enhance the performance of the algorithm we analyzed the impact of projection tolerance by keeping the smoothing kernel length constant as SK 60 and only changing projection tolerance. For each value of projection tolerance, we also calculated the number of iterations and total time consumed for complete reconstruction. Figure 6.7 illustrates a comparison between scans reconstructed with manufacturer software without motion correction along with motion-corrected with SK 60 but various projection tolerance thresholds. Image reconstruction with applying SK 60 and PT 0.001 completely corrected MA. Conversely, images reconstructed by employing PT 0.005, PT 0.0012, PT 0.0015, PT 0.0018, and PT 0.0025 still indicate residual motion artifact. From figure 6.8 b similar conclusion can be drawn that SK 60 and PT 0.001 nearly corrected MA. Figure 6.9 corresponds to the graph between projection angle and motion estimation with different PT values. It is obvious that motion estimation with different PT values is not considerably different. Figure 6.10 indicates that PT values have a very small impact on motion estimation but while reducing the value of PT the number of iterations increases at each resolution level. Consequently, total reconstruction time increases with the smaller value of PT.

To evaluate the effect of extended iteration the projection tolerance was reduced to a very small value of 0.0001 with a constant value of SK 60. Various images were reconstructed and compared with standard non-motion-corrected images to analyze the impact of the increased number of iterations. Figure 6.11b represents the image with the smallest PT 0.0001 and having more iterations. This image is not superior to figure 6.11c and figure 6.11d with PT 0.001 and PT 0.0015, respectively.

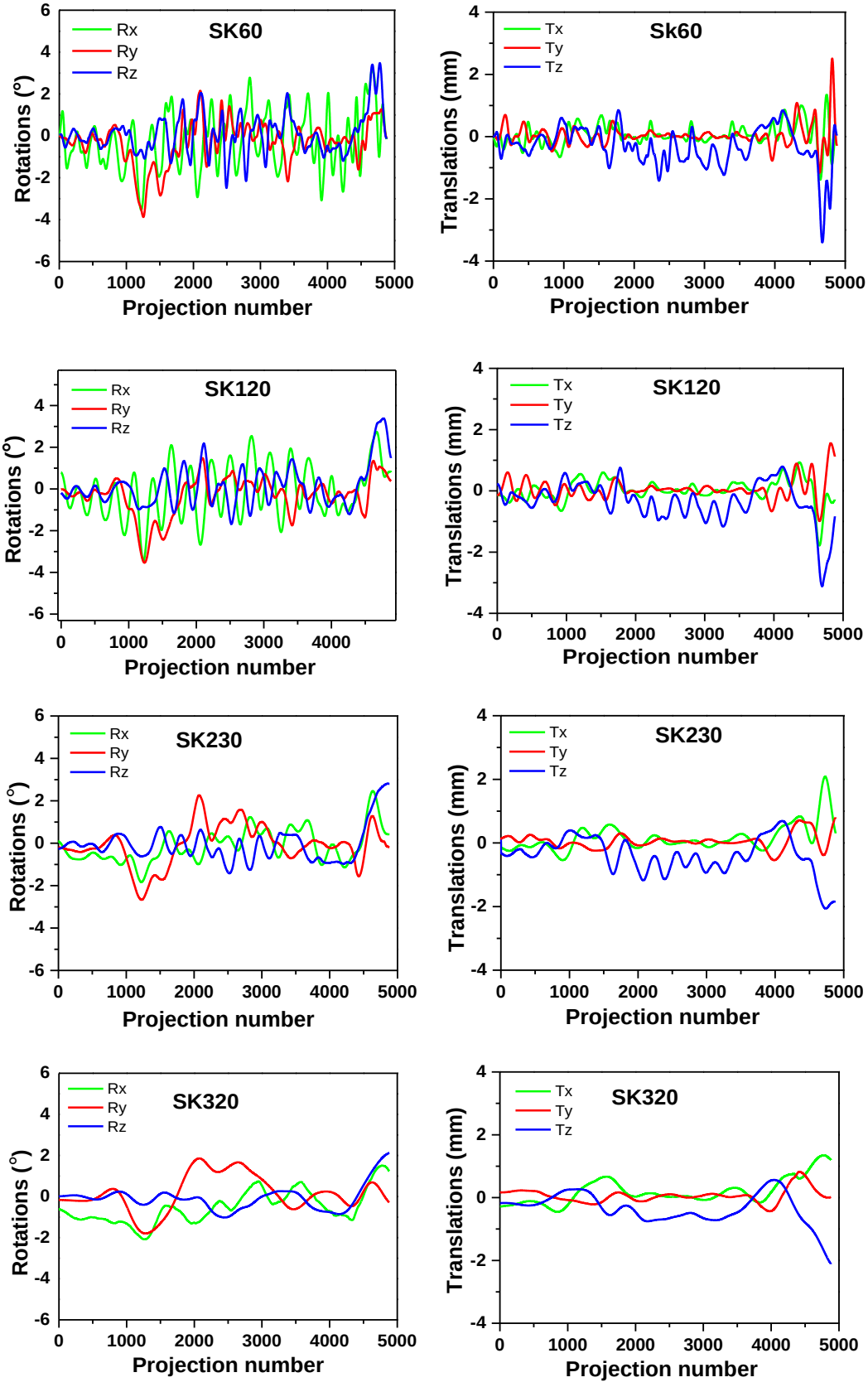

Figure 6.5: Comparison of different smoothing kernels for three rotation parameters (Rx, Ry, Rz) and three translation parameters (Tx, Ty, Tz).

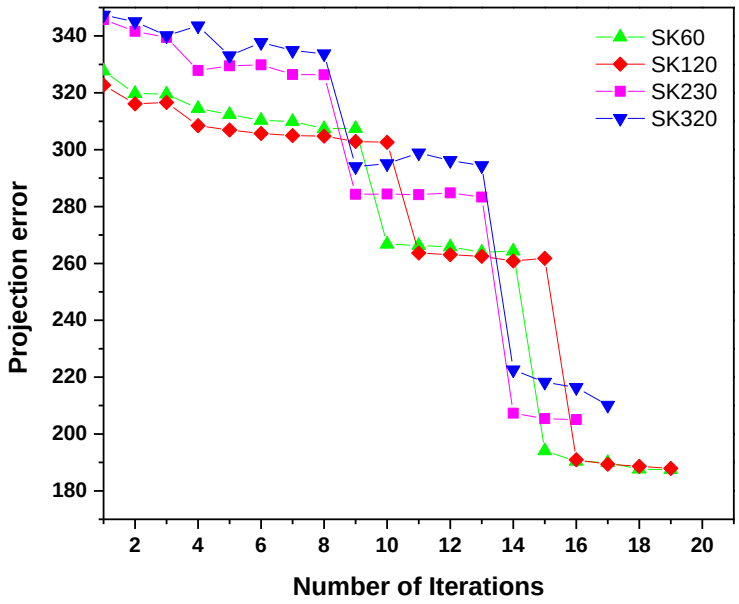

Figure 6.6: Number of iterations and projection error for different SK values, PE drops as the number of iterations increases.

In our trials, we noticed that the motion estimate hardly improved during the computation by escalating the number of iterations. As these computations (if incorporated) are the priciest ones in terms of computation time, therefore, it was decided that PT 0.001 could be sufficient for eliminating residual motion error. The mean number of iterations for different PT values is listed in Table 6.1.

Table 6.1: Mean number of iterations for different PT values at each resolution level

Resolution Level	**Mean number of iteration**						
	PT (0.0001)	**PT (0.0010)**	**PT (0.0012)**	**PT (0.0015)**	**PT (0.0018)**	**PT (0.0025)**	**PT (0.005)**
Resolution 441	18	11	10	9	8	7	7
Resolution 221	9	7	6	5	4	4	3
Resolution 111	8	7	7	6	5	5	4

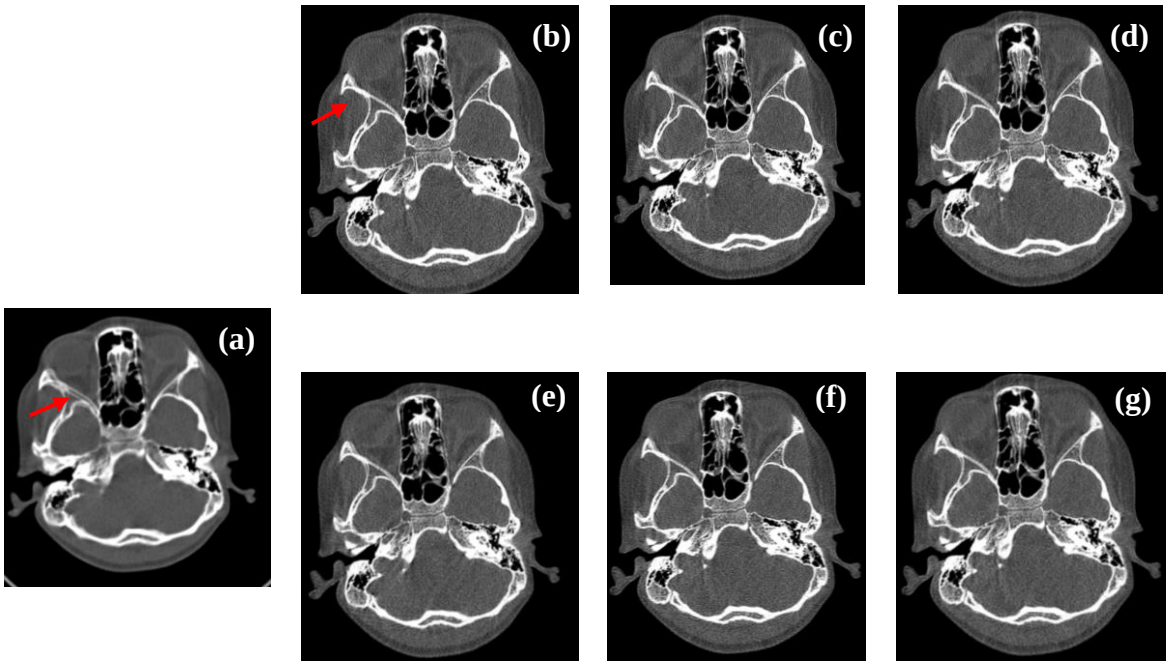

Figure 6.7: (a) Image reconstruction obtained using Siemens software without motion correction, the arrow pointing to MA, (b-g) image reconstruction with data-driven using smoothing kernel 60 and PT set to 0.001, 0.005, 0.0012, 0.0015, 0.0018, and PT 0.0025, respectively. MA was completely corrected in (b), but the correction was less complete in (c-g).

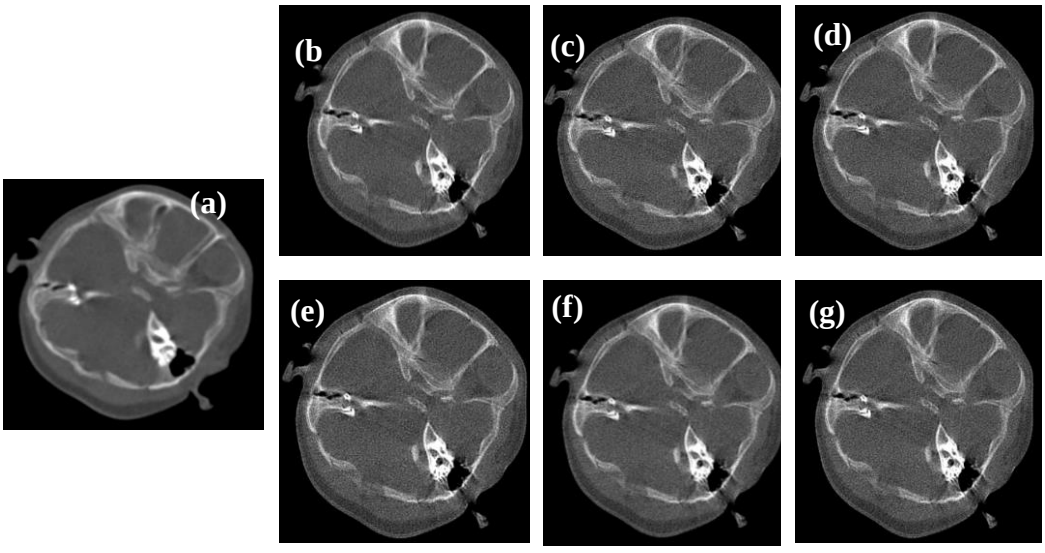

Figure 6.8: (a) Image reconstruction by using Siemens software without motion correction, (b) image reconstruction with data-driven using SK 60 and PT 0.001 completely corrected MA, (c-g) image reconstruction with data-driven using SK 60 and PT 0.005, PT 0.0012, PT 0.0015, PT 0.0018, and PT 0.0025 respectively.

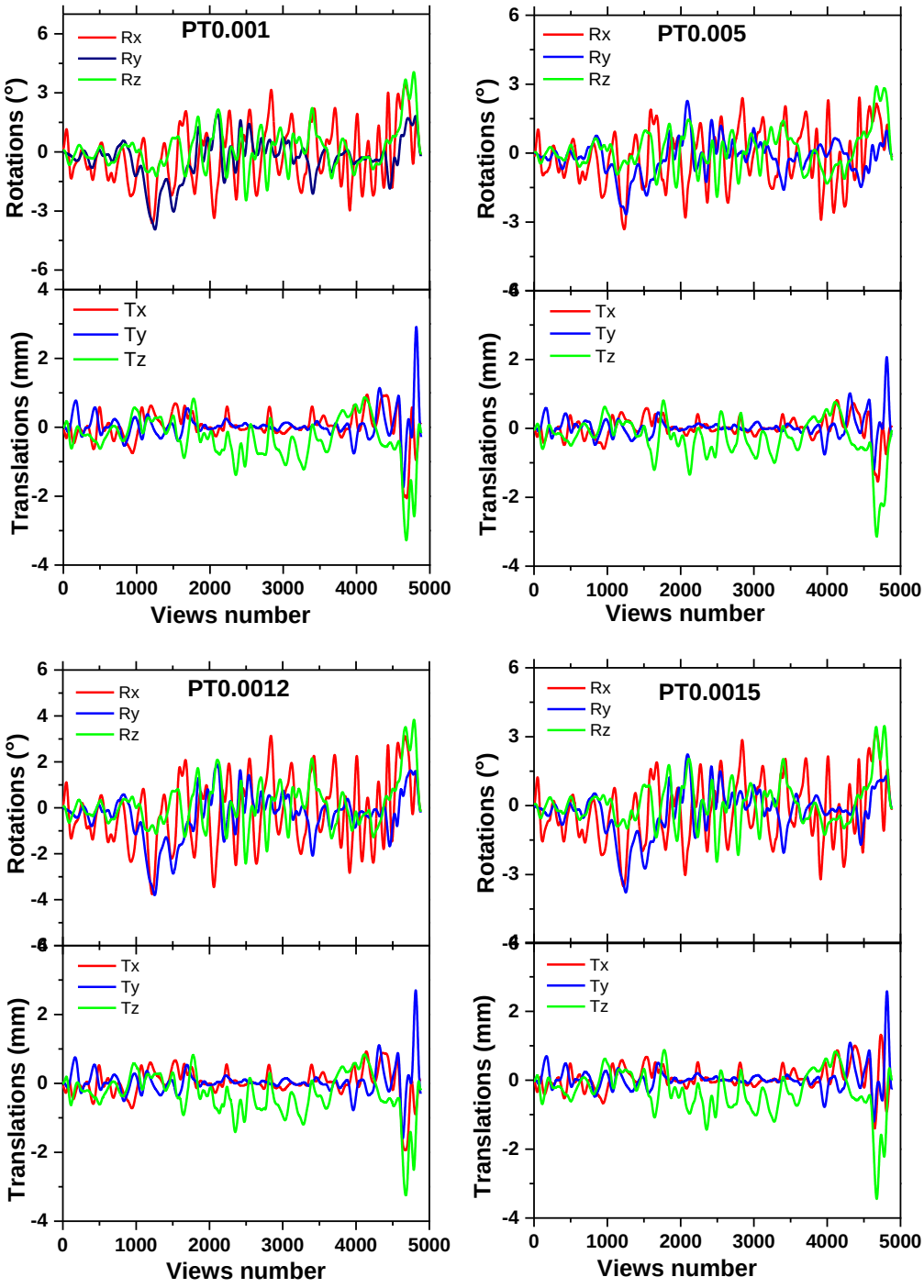
PT0.001
PT0.005
PT0.0012
PT0.0015
Rx
Ry
Rz
Tx
Ty
Tz
Rotations (°)
Translations (mm)
Views number

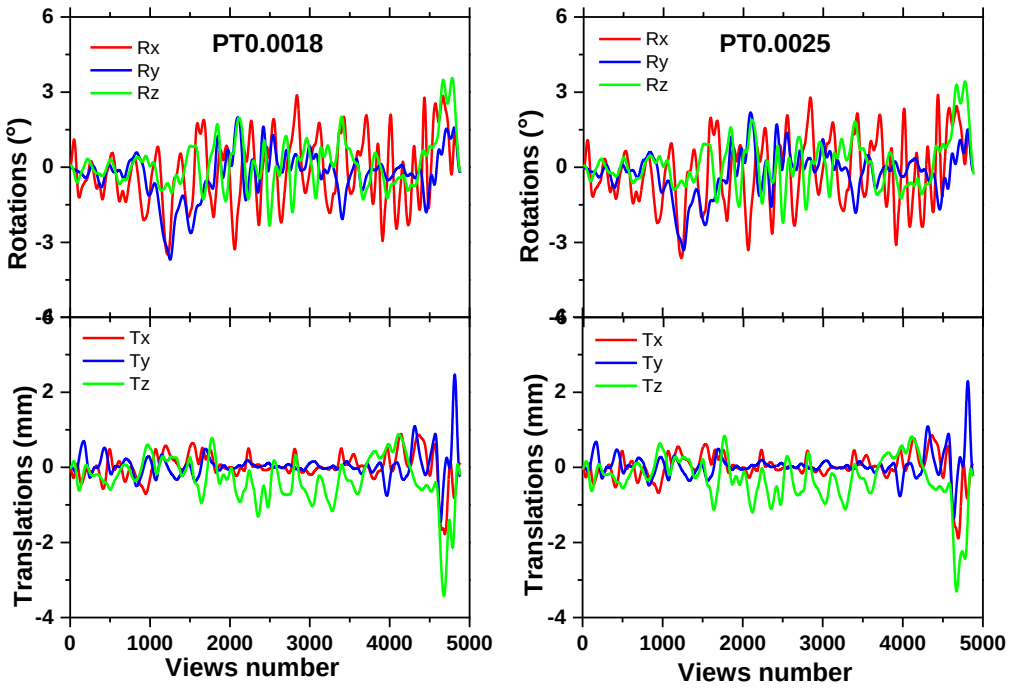

Figure 6.9: Comparison of three rotation parameters (Rx, Ry, Rz) and three translation parameters (Tx, Ty, Tz) for different projection tolerance.

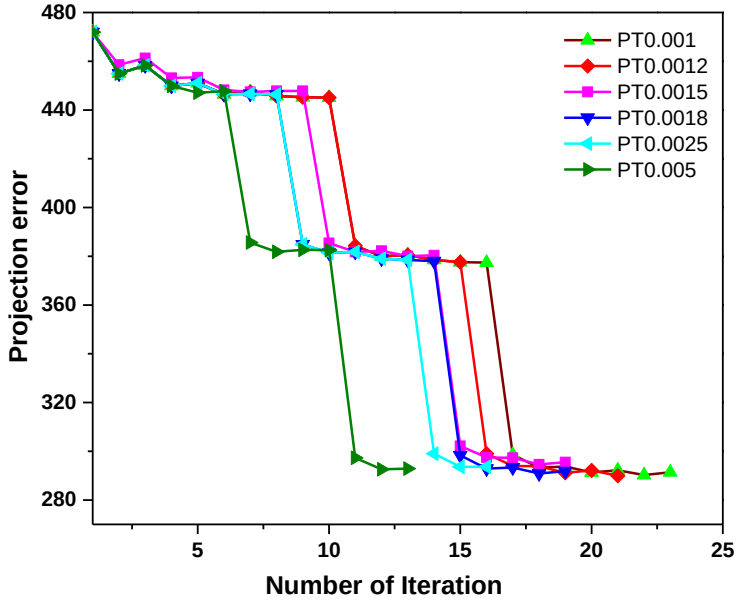

Figure 6.10: Number of iterations and projection error for different projection tolerance.

6.7.3 Angle rebin

To study the role of AR the projections were rebinned by summing groups of 8, 16, 32 consecutive projections. Figure 6.12 column b demonstrates iterative image reconstruction with data-driven using SK 60/PT0.001/AR 8 removed MA, while in SK 60/PT 0.001/AR 16 (column c) and SK 60/PT 0.001/AR 32 (column d) respectively still have the residual artifact. Due to a large number of views in the scan, it is necessary to speed up the reconstruction process, using AR 8 significantly reduces computation time.

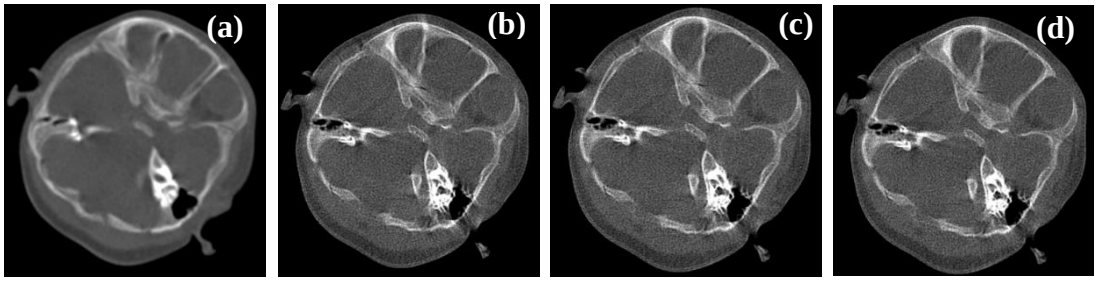

Figure 6.11: Impact of extended iteration with constant smoothing kernel, (a) real image without motion correction, (b) SK 60/0.0001, (c) SK 60/0.001, (d) SK 60/0.0015.

MRS for SK 60, AR 8 were found statistically significantly ($p < 0.05$) as compared with SK 120, SK 230, and SK 320 and AR 16, AR 32, respectively. Although, MRS for PT 0.001 not providing statistically significant differences ($p > 0.05$) from PT 0.0015, PT 0.0018, PT 0.0025, and PT 0.005 respectively. The reconstructed scans were considered diagnostically appropriate and decreased the possibility of repeat scanning.

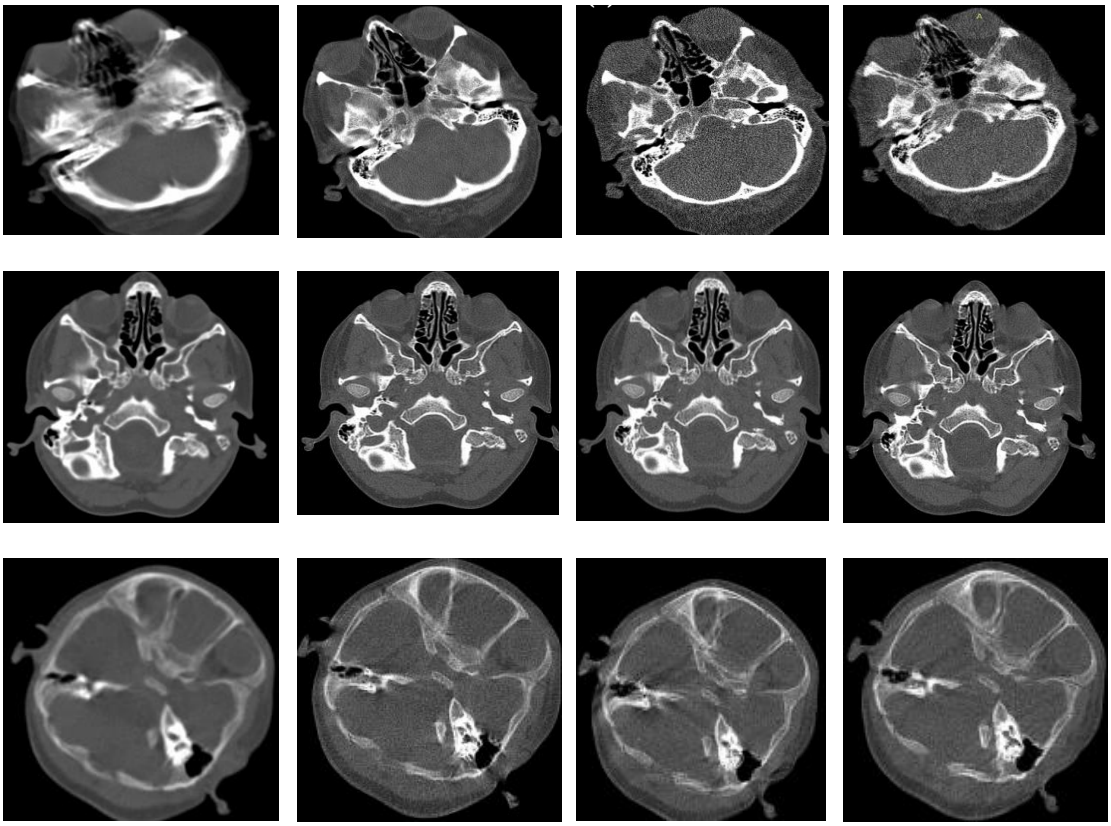

Figure 6.12: Column (a) Real image reconstruction with Siemens software without motion correction, column (b) iterative image reconstruction with data-driven using smoothing kernel SK60 / PT 0.001 / AR 8 removed ghosting, column (c, d) SK 60 / PT 0.001 / AR 16 and SK 60 / PT 0.001 / AR 32 respectively still have the residual artifact.

6.8 Discussion

Patient head movement during CT scanning causes a reduction in the quantitative and qualitative accuracy of the image. Sometimes a repeat scan is indispensable to acquire an artifact-free image that entails a detrimental radiation burden to the patient. In almost 25% of patients with acute ischemic stroke, moderate to the severe head movement was detected in CT perfusion scans (Allmendinger et al., 2012). Furthermore, motion correction in head CT scanning is a common concern as CT attenuation correction is also critical for an accurate evaluation of the distribution of brain radioactivity in PET/CT and SPECT/CT (Brady et al., 2008). MC methods based on motion tracking systems were reported for neurological PET (Bloomfield et al., 2003, et al., 2002). Nevertheless, the MC in the helical CT part of hybrid imaging was envisaged before. Using a CT MC approach with PET MC methods would facilitate motion correction in hybrid PET/CT images. As the patient's motion during helical CT scanning may considerably affect image quality, it is necessary to limit patient movement

in the CT scan. But, the possibility of complete motionlessness is unrealistic in routine clinical application. It was reported that patient movement was significantly more prominent at the beginning of the scan when sound and vibrations were probably a major source of irritation to the patient (Hanzelka et al., 2013).

The performance of the data-driven motion correction was validated for several CT scanner models with considerably different numbers of detector rows. It was observed that the MC method could be easily implementable on most clinical helical CT scanners presently in routine use if access to the raw data is available. For the six motion parameters, three rotation parameters Rx, Ry, Rz, and three translation parameters Tx, Ty, Tz, the degree of motion was determined (Kim et al., 2016, Sun et al., 2016). A translation motion < 1.5 mm in 16 from 19 healthy volunteers, and 4 mm in only 3 volunteers were previously reported (Li et al., 2010). In another study of 20 patients, CT mean rotational motion of 1.06 mm and mean translational motion of 2.5 mm respectively was observed (Wagner et al., 2003). Moreover, a study of 103 suspected acute ischemic stroke patients with head motion reported similar rotational and translational excursion (Sun et al., 2017). Hence, the translational and rotational movement in our patient data was found to be comparable in magnitude to values formerly reported by (Allmendinger et al., 2012, Li et al., 2010, Wagner et al., 2003).

Extreme head motion generating insufficient data for reconstruction is the only constraint on the accuracy of the MC approach. Certainly, it was not a limitation of the technique but the inadequacy of the data accessible for reconstruction due to enormous motion. Our group formerly proposed a method to measure data sufficiency in helical CT scans by Tuy map (Sun et al., 2017). In the clinical framework, the Tuy map could be a precise way of predicting the data-insufficiency artifacts. We have validated that significant motion correction can be achieved with data-driven motion correction for a variety of human head movements in clinical helical CT scanning if the data sufficiency condition is not violated.

Reconstruction kernels define the sharpness and smoothness of CT images. Sharper kernels block low-frequency and utilize high-pass filter content to offer better spatial resolution at the cost of more noise. In contrast, smoothing kernels block high-frequency and preserve low-frequency content to offer better low-contrast resolution with less noise in the final CT images. The SK length, PT, and AR have a significant impact on ME as well as motion compensation. The SK 60, PT 0.001, and AR 8 generate satisfactory artifact-free images. Overall, the images reconstructed by SK 60 offer more promising results. As the value of SK increases the motion

estimation becomes smoother, not demonstrating a true motion estimation. The best size of the smoothing kernel varies with the number of views per rotation and the axial extent of the detector. The axial extent depends on various scan configurations (slice collimation). The number of kernel points is directly related to the number of projections per rotation. With the increase in the number of views per rotation the size of kernel points increased.

Due to a large number of projections data, it was necessary to accelerate the reconstruction process. The projections were rebinned by accumulating groups of 8 consecutive projections, which significantly accelerates convergence. Moreover, a fast convergence might be obtained by reducing iteration at a low-resolution level or by using an analytic method of reconstruction. Another approach could be the use of different projection models in different segments of the reconstruction volume to accelerate the convergence (Slambrouck et al., 2012). In clinical helical CT scanning, the MC images were superior to the uncorrected images in nearly all patient scans with a variety of head movements. The amount of movements (slight to severe), the interval of motion, and the timing of the start of motion can affect the compensation. The technique could facilitate the evaluation of patient scans that otherwise was not possible with conventional reconstruction approaches. The MC application alleviates the requirement for repeat CT scans and reduces the radiation burden on the patient. Certainly, it would be significant to implement data-driven motion correction to a big sample of motion-affected scans and accomplish a thorough assessment of the impact of MC on clinical diagnosis.

Chapter 7. The Effect of Head Movement During CT on Hybrid PET/CT Brain Scan

7.1 Introduction:

PET/CT scans are commonly used in the clinic for oncological cardiologic and neurologic applications (Brady et al., 2008). The CT image of the PET/CT scan not only delivers anatomical information but is also used in computing attenuation correction and scatter correction (Kinahan et al.,1998, Watson et al., 2004) to substitute for the transmission scan. In stand-alone PET scans, the effects of head movements on attenuation correction and scatter correction have previously been examined (Wardak et al., 2010, Anton-Rodriguez et al., 2010). Due to the mismatch between the CT and PET images, head motions during CT scans might cause artifacts in attenuation correction and scatter correction.

The PET/CT system is a hybrid imaging system that incorporates CT for anatomical information, localization of lesions on PET, and also for attenuation correction of the PET data (Kinahan et al.,1998). Head movement during CT imaging results in a mismatch between CT and PET images. It can cause artifacts in CT-based attenuation corrected PET images, thus affecting both the qualitative and quantitative aspects of the PET images. A motion correction method could change diagnostic accuracy in the event of motion. The data-driven iterative reconstruction method could be advantageous for patient groups in hybrid imaging using SPECT/CT and PET/CT as well as standalone CT. This would be helpful to the patients prone to motion who are at risk of getting an unnecessary radiation dose from repeat scans. The problem is especially serious for children and patients with movement disorders.

In PET-only scanners, a lot of effort has gone into reducing motion artifacts. To realign the transmission image to each emission frame for more accurate attenuation and scatter correction, two general approaches have been investigated: using a motion tracking system (Keller et al., 2012, Bloomfield et al., 2003) or using image-based realignment (Costes et al., 2009, Mourik et al., 2013). For phantom scans, movement correction (MC) using motion tracking devices like the Polaris system is very accurate. But, image-based motion correction was found to outperform the other approaches in a majority of situations due to fixation issues in human scans (Mourik et al., 2013).

Our group and many others have used the Polaris motion tracking system to apply MC algorithms for neurological PET, e.g. (Fulton et al., 2002, Bloomfield et al., 2003, Mourik et al., 2013, Suchorska et al., 2014). However, the possibility of also correcting for motion through the CT phase of hybrid imaging scans does not seem to have been envisaged before. Combining a CT MC method with existing PET MC methods would enable MC to be applied to both the CT and PET part of PET/CT. The objective of this work is to evaluate the impact of a 3D iterative data-driven motion compensation technique to compensate for head movement during a CT scan of brain PET/CT and investigate its significance for final image reconstruction.

7.2 Materials and methods

A series of PET/CT scans of Hoffman brain phantom filled with fluorodeoxyglucose (^{18}F-FDG) was acquired on Siemens Biograph mCT scanners with 128 slice CT scanner (Siemens Medical Solutions USA, Inc., Malvern, PA) using routine head CT (ref. mAs 250 tube current, rotation time 0.5 s, tube voltage 120 kVp, pitch = 0.8, 40 x 0.6 mm slice collimation). The phantom was acquired with a movement during the CT part of the acquisition, to simulate patient movement, but the phantom remained stationary during the PET scan.

Subsequently, the data-driven motion compensation approach was also implemented on the patient presenting head movement during the CT part of the brain PET/CT scan. The patient was acquired on Siemens biograph mCT PET/CT scanner having 128 slice CT.

CT acquisition: 120 kVp, 1 second rotation time, pitch 0.8, regular-dose mode, 250 ref. mAs tube current, 100 kVp tube voltage, 40 x 0.6 mm slice collimation, pitch = 0.8) and patient acquired using Care Dose 4D to minimize radiation doses.

PET acquisition: With 103 MBq activity, a whole-body CT was done (from the base of the head to the proximal thighs).

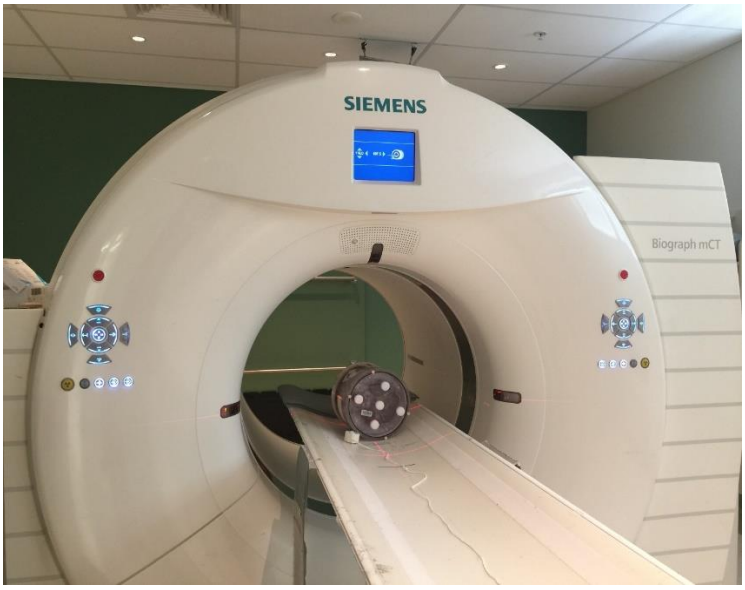

Figure 7.1: Hoffman brain phantom acquisition on Biograph mCT.

1. Each motion corrupted CT scan was reconstructed using fully automated 3D iterative data-driven image reconstruction with motion compensation (MC) to remove motion artifacts. Motion corrected CT was reconstructed by using the data-driven algorithm described in chapter 5.
2. An offline attenuation and scatter map was generated from these motion-corrected CT scans.
3. The raw data of the PET scan was reconstructed offline using the JSrecon algorithm with attenuation and scatter map generated from motion-corrected CT.
4. The images were compared with the PET scan reconstructed with an attenuation map from motion corrupted CT.
5. For qualitative analysis, all reconstructed images were scored, absolute differences, 3D-standard surface projection (3D-SSP) analysis, and Scenium analysis were obtained for quantitative analysis.
6. In the motion correction method, it is assumed that all in the CT scanner field of view moved rigidly except the couch. So, couch segments were deleted from the raw data preceding reconstruction after the accomplishment of the first step (Figure 7.2).

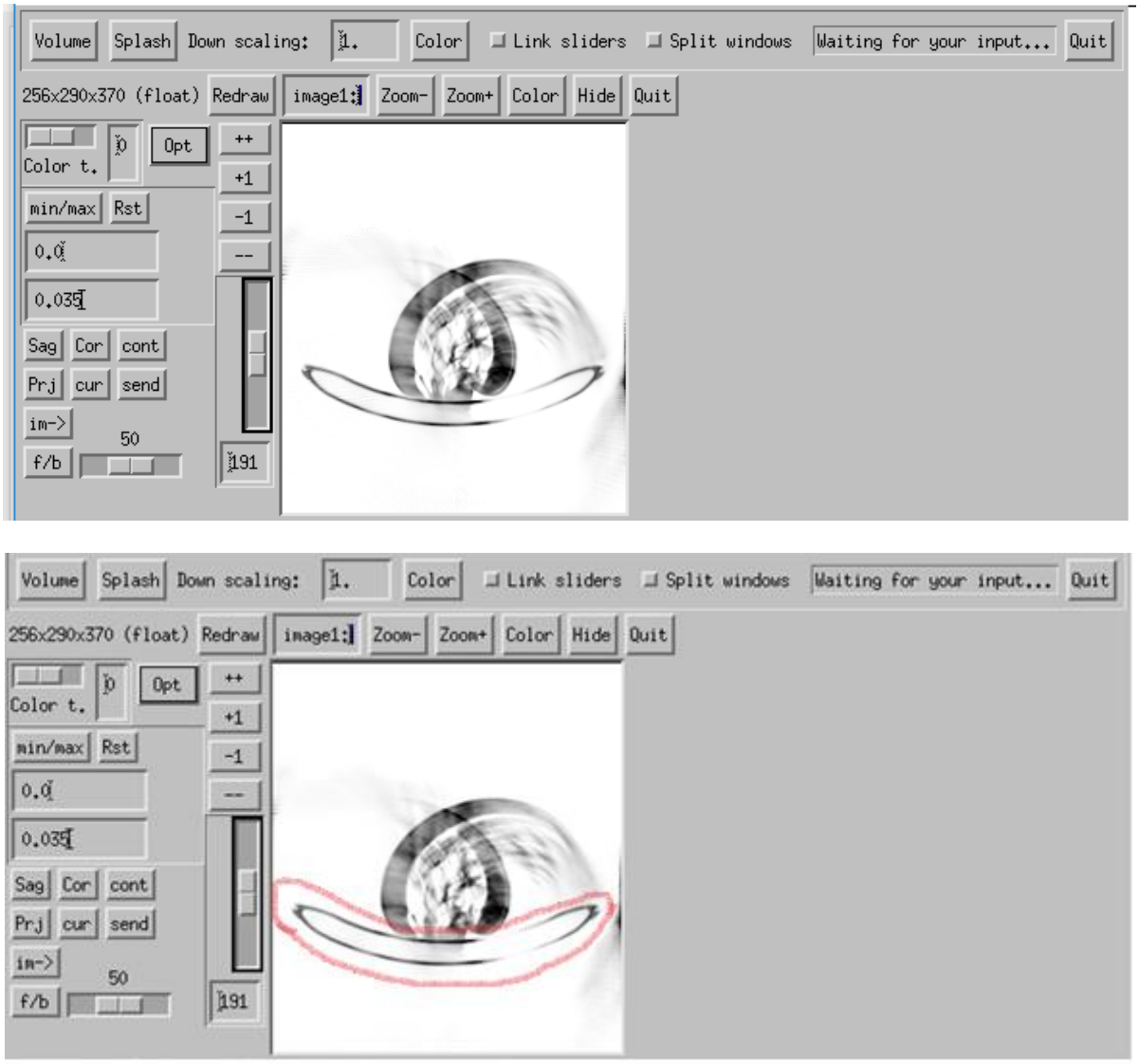

Figure 7.2: Top: phantom scan with couch segment, bottom: couch segments were deleted from the raw data before reconstruction.

7.3 Results

3D iterative data-driven motion estimation and correction were used for the reconstruction of Hoffman's brain phantom, and the approach worked well as shown in figure 7.3.

Figure 7.3: CT scan of a) stationary phantom, b) moving phantom, c) motion-corrected.

Figure 7.4 is a comparison of an axial view of the ^{18}F-FDG-PET scan of static Hoffman brain phantom with phantom scan reconstructed using a CT image with motion artifacts (nMC image) and reconstructed using a motion-corrected CT image for scatter and attenuation correction (MC image). Reconstructed CT and PET images are shown in figures 7.3 and 7.4, a significant decrease in movement artifacts is evident in both CT and PET images with motion correction.

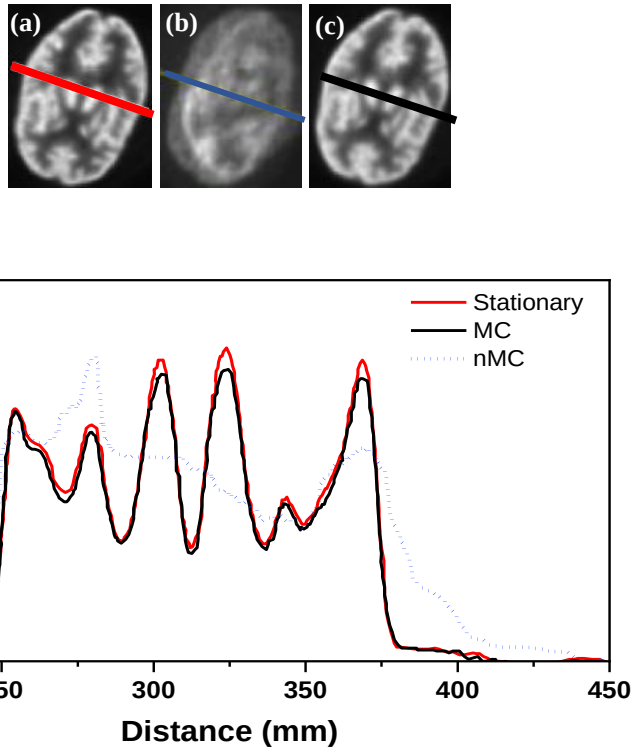

Figure 7.4: Axial view of an ^{18}F-FDG-PET scan of (a) stationary phantom, (b) reconstructed using a CT image with motion artifacts (nMC), (c) reconstructed using a motion-corrected CT image for attenuation and scatter correction (MC), **(**d) The profile along the lines for stationary, nMC and MC PET images.

When motion-corrected CT data were utilized for attenuation correction of acquired PET data, profile comparison revealed that whether the motion-corrected CT attenuation map or the motion-

free CT attenuation map was used for attenuation correction, equivalent results were achieved, as shown in figure 7.4. (d).

7.4 Patient scan

The ^{18}F-FDG PET/CT brain scans were acquired on individuals after fasting 4 hrs before scanning. ^{18}F-FDG was administered 45 min before scanning based on the weight of the patient. FDG-PET/CT images were acquired for 3-5 min bed position using a Siemens biograph mCT PET/CT scanner having 128 slice CT. The patient was included in the study having movement during the CT part of the acquisition, but they remained stationary during the PET scan.

Each motion corrupted CT scan was reconstructed by 3D iterative data-driven image reconstruction with motion compensation. CT image reconstructed by vendor software without motion correction and CT image with motion corrected reconstruction with data-driven algorithm demonstrated in figure 7.5 and ghost artifact removed after motion correction.

An offline attenuation and scatter map was created from these MC CT scans. The PET scan was reconstructed offline using raw data by JSrecon algorithm with attenuation and scatter map generated from MC CT, an example is shown in figure 7.6. Attenuation-corrected PET images were also iteratively reconstructed by standard vendor-provided software with an attenuation map from motion corrupted CT (nMC). Both images nMC and MC were visually inspected by qualified nuclear medicine physicians and a substantial difference in image quality was noticed.

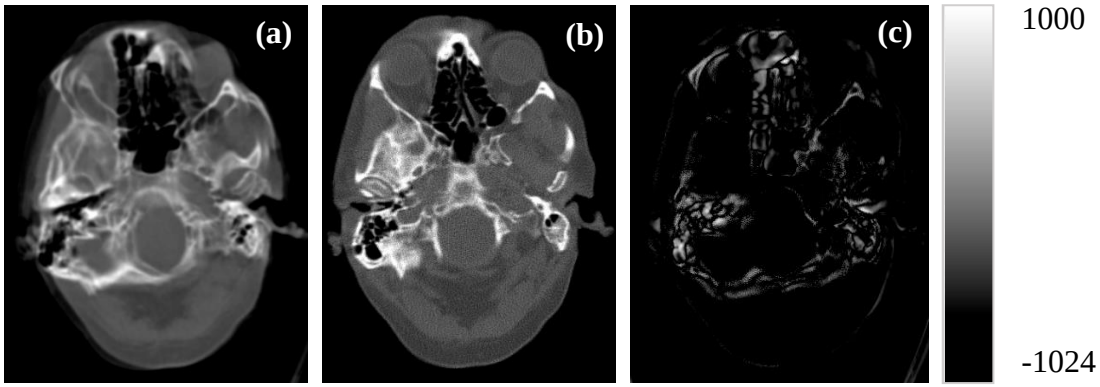

Figure 7.5: (a) CT image reconstructed by vendor software without motion-correction, (b) motion corrected reconstruction and ghost artifact removed after motion-correction, (c) absolute difference between a and b image.

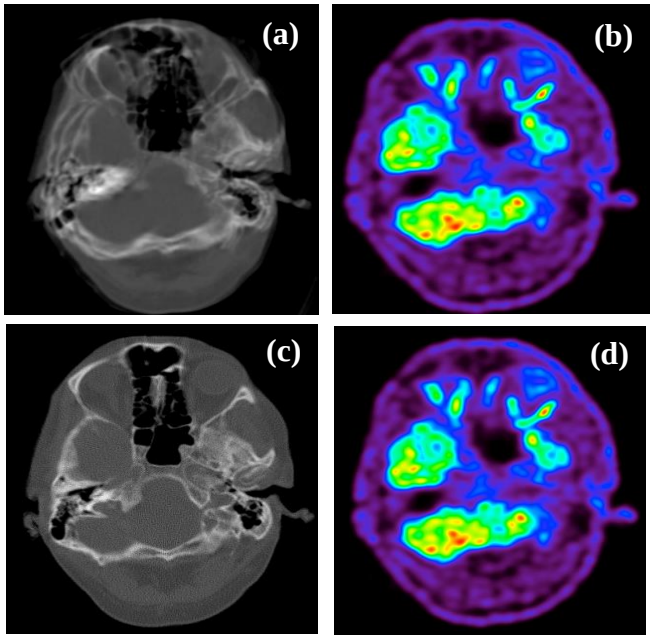

Figure: 7.6 (a) CT image reconstructed by vendor software without motion-correction, (b) PET image reconstructed using a CT image with motion artifacts (nMC), (c) CT image with motion-corrected reconstruction and artifact removed after motion-correction, (d) image reconstructed using a motion-corrected CT image for attenuation and scatter correction.

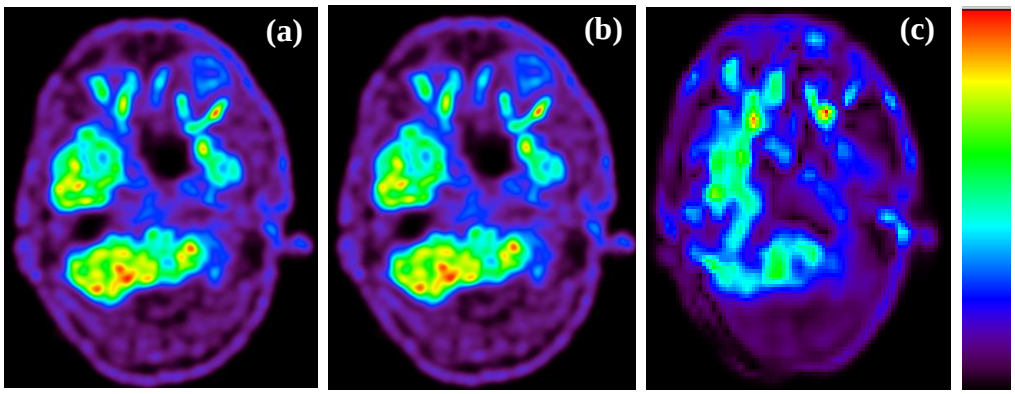

Figure 7.7: (a) PET image using a CT image with motion artifacts (nMC), (b) PET image reconstructed using a motion-corrected CT image for attenuation and scatter correction (MC), (c) |Difference| bewteen a and b image.

The image in the middle of Figure 7.7 has been reconstructed using a motion-corrected CT image for scatter and attenuation correction, whereas the one on left was reconstructed using a CT image with motion artifacts. Although the images appear identical, there are quantitative differences

between them as exhibited in (c). Whether these differences are large enough to be clinically significant would require a larger study with more cases having a variety of emotions as well as different diagnostic scans.

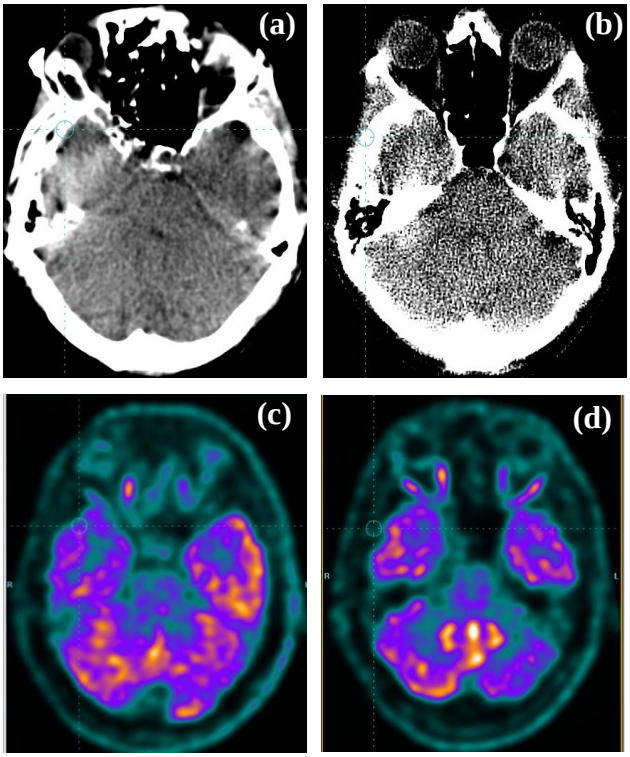

Figure 7.8 (a) CT image reconstructed by vendor software without motion-correction, (b) PET image reconstructed using a CT image with motion artifacts (nMC), (c) CT image with motion corrected reconstruction and artifact removed after motion correction, (d) image reconstructed using a motion corrected CT image for attenuation and scatter correction (MC).

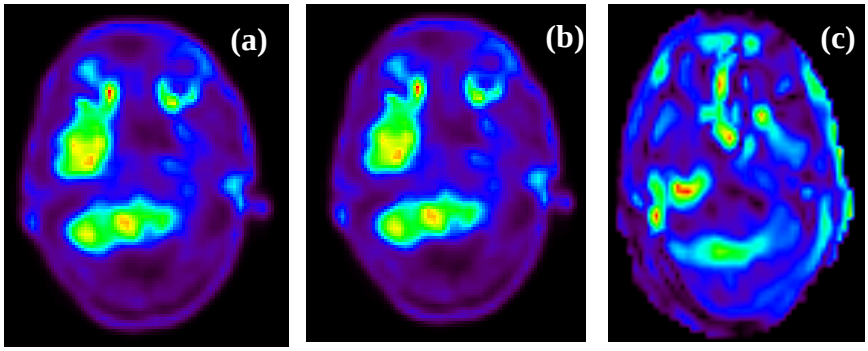

Figure7.9: (a) PET (nMC), (b) corrected PET for attenuation and scatter correction (MC), (c) "|Difference|".

7.5 Quantitative Scenium analysis

Scenium is a completely automated, FDA-approved software that is often used in clinical settings (Syngo.Via.v11 platform, Siemens). It is an advanced neural assessment tool designed for voxel-wise evaluation. It can automatically draw 10 basic brain regions and calculate the SUVmean using the template, avoiding human error. As a result, it may be used to compare different brain imaging modalities quantitatively, improving the accuracy and reliability of the results. The voxel-wise analysis produces statistical parametric maps highlighting regions on a patient's scan with significantly different metabolism.

The axial, coronal, and sagittal PET views with attenuation map obtained with nMC-CT attenuation correction and with PET views reconstructed with MC-CT are illustrated in figure 7.10. The scenium analysis of MC-PET and nMC-PET are presented in figure 7.11 and arrows point to the differences.

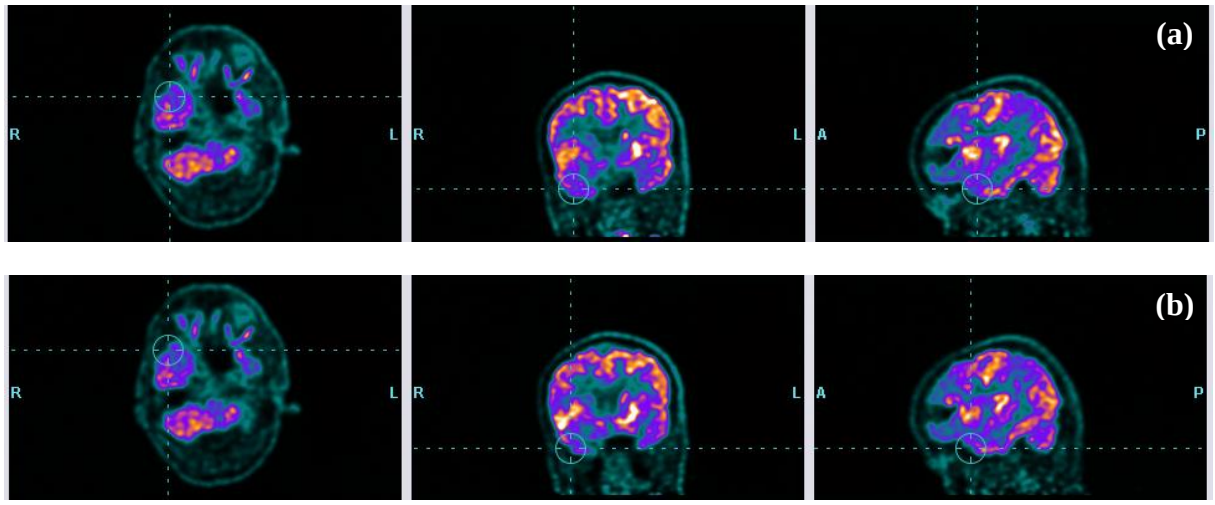

Figure 7.10: (a) Axial, coronal and sagital PET (nMC), (b) axial, coronal and sagital PET (MC).

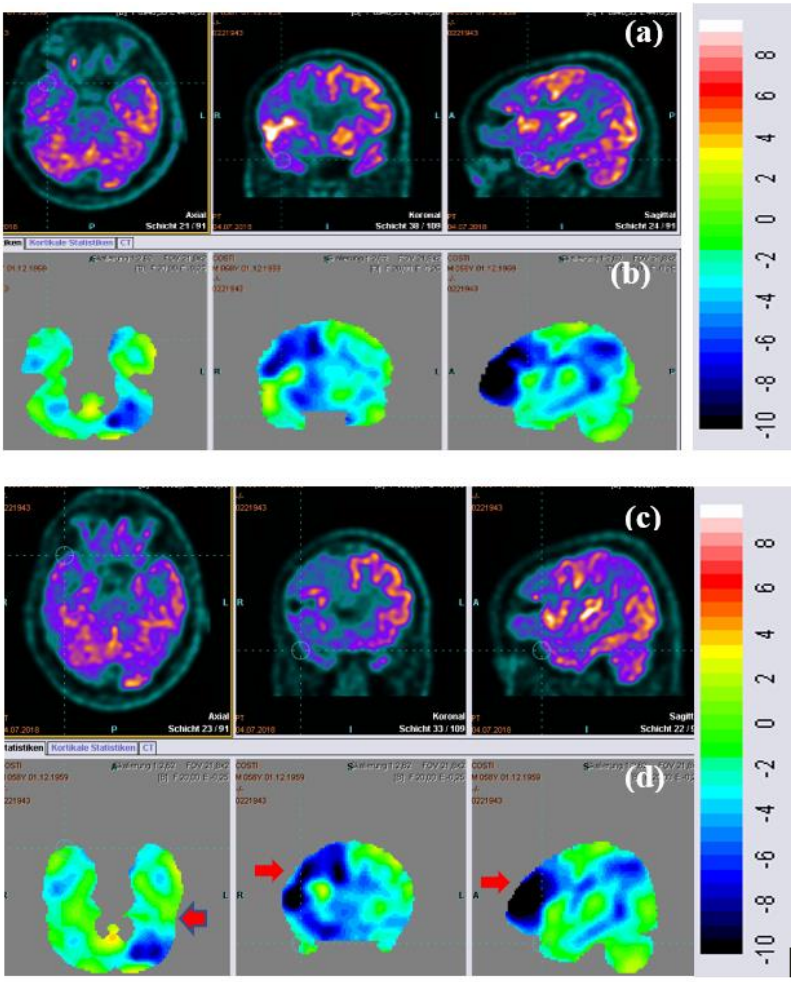

Figure 7.11: (a) Axial, coronal, and sagittal PET views with attenuation map obtained with nMC-CT attenuation correction, (b) scenium analysis nMC-PET, (c) axial, coronal, and sagittal PET views reconstructed with MC-CT, (d) scenium analysis MC-PET (arrows pointing the differences).

Tables 7.1 and 7.2 offered the details of Scenium analysis nMC-PET and Scenium analysis MC-PET. The reconstructed PET images of both nMC-PET and MC-PET were evaluated and the results depicted that the SUVmean of all brain areas in nMC-PET was significantly higher in comparison to MC-PET.

Table 7.1: Scenium analysis nMC-PET

ROI	Site	SUV Min.	SUV Avg.	SUV Max.	Standard deviation
Basal ganglia	L	1.12	5.67	11.92	-0.5
Basal ganglia	R	0.88	3.99	8.00	-5.4
Central region	L	0.28	6.31	11.13	1.2
Central region	R	0.16	5.38	9.69	-2.2
Cerebellum	L	0.10	5.22	10.91	-5.6
Cerebellum	R	0.12	5.46	9.65	-0.2
Cingulate and paracingulate gyri	L	0.87	4.78	9.16	-3.2
Cingulate and paracingulate gyri	R	0.59	3.88	8.97	-5.2
Frontal lobe	L	0.42	5.30	10.28	-3.4
Frontal lobe	R	0.14	3.70	10.89	-10.2
Mesial temporal lobe	L	0.95	4.20	9.49	-3.2
Mesial temporal lobe	R	1.51	4.26	7.13	-2.6
Occipital lobe	L	0.08	6.19	10.73	-1.1
Occipital lobe	R	0.77	5.83	10.80	-2.0
Parietal lobe	L	0.57	5.95	11.08	-1.4
Parietal lobe	R	0.30	4.78	8.68	-5.2
Temporal lobe	L	1.02	6.00	11.55	-0.8
Temporal lobe	R	0.05	5.03	11.43	-3.9

Table 7.2: Scenium analysis MC-PET

ROI	Site	SUV Min.	SUV Avg.	SUV Max.	Standard deviation
Basal ganglia	L	1.25	5.80	11.44	0.7
Basal ganglia	R	0.96	3.97	7.68	-4.9
Central region	L	0..49	6.33	11.05	2.7
Central region	R	0.22	5.32	9.76	-1.1
Cerebellum	L	0.16	4.79	10.12	-7.3
Cerebellum	R	0.13	5.25	9.32	0.6
Cingulate and paracingulate gyri	L	0.70	4.73	9.05	-2.6
Cingulate and paracingulate gyri	R	0.49	3.85	8.97	-4.6
Frontal lobe	L	0.50	5.28	10.24	-2.2
Frontal lobe	R	0.10	3.63	10.22	-9.6
Mesial temporal lobe	L	1.00	4.08	8.42	-2.6
Mesial temporal lobe	R	1.59	4.11	6.97	-2.3
Occipital lobe	L	0.16	6.14	10.49	-0.0
Occipital lobe	R	0.67	5.72	10.31	-1.2
Parietal lobe	L	0.67	6.01	11.02	0.0
Parietal lobe	R	0.38	4.75	8.80	-4.2
Temporal lobe	L	0.96	5.77	10.88	-0.4
Temporal lobe	R	0.07	4.98	11.07	-3.0

7.6 Discussion

Generally, the most common use of brain PET scanning is in tumor diagnosis (Marcus et al., 2014), Alzheimer's disease diagnosis (Roberts et al., 2014), and cognitive function research (Zaidi et al., 2007). Photon attenuation in tissues has long been thought to be the most important physical element affecting image quality and quantitative accuracy. In the qualitative and quantitative analysis of brain PET imaging, attenuation correction is a critical step. Therefore, a correct attenuation map is essential for quantitative PET image reconstruction, to compensate for attenuation.

The attenuation correction (AC) method, which uses transmission scanning, produces the least amount of bias and is regarded as the "gold standard" of brain PET imaging (Zaidi et al., 2004, Kinahan et al., 2003). In PET/CT scans, CT AC is widely used because it is fast, has low noise, and has good data statistics (Quinn et al., 2016). However, CT AC has disadvantages, including increased subject radiation exposure (Brink et al., 2010), overestimation of SUV of high-density materials (Huang et al., 1979, Herzog et al., 2005), and the possibility of image artifacts due to patient movement between sequential scans (Rahmim et al., 2007).

The head motion correction has received less attention in x-ray helical CT than in other imaging modalities. A retrospective motion compensation method for helical CT, on the other hand, would be extremely useful in clinical practice. Even with the latest, state-of-the-art CT scanners, patient motion artifacts are still observed in CT images. Patient movements in head CT imaging are assumed to be rigid, in contrast to cardiac and respiratory motions. Several head restraints are currently used which include neoprene caps, thermoplastic masks that reduce the amount of movement but do not eliminate it (Hoffman et al., 1990). Depending on the type of mask and the scan duration, typical translations of 5 to 20 mm and rotations of 1 to 4 degrees are recorded even with head restraints.

In PET/CT motion can occur during the CT part of the scan or PET or both. Motion in CT could potentially affect the diagnosis of a PET/CT scan. We studied these effects in phantom studies and patient studies where PET/CT scan was affected by CT motion. A 3D Hoffman brain phantom was used to simulate the activity distributions present in the human brain in the cerebral blood flow. The phantom consists of a single chamber and thin layers of lucite to give relative concentration for ventricles, white matter, grey matter respectively in the brain.

Motion in CT scan affects PET scan in a variety of ways

1. Attenuation correction
2. Scatter correction
3. Quantification
4. Potential alignment in localization
5. Distort image

Image reconstruction has an important influence on image quality and consequently on radiation exposure. It is necessary to reconstruct images with the minimal amount of noise possible for a given dose without compromising image quality or spatial resolution (Logan et al., 1996). Image quality can be improved without increasing radiation dose by using a smart image reconstruction algorithm.

Siemens SMART neuro attenuation correction (SNAC) is a new type of CAC procedure. It can be used to model tissue and bone structures in the lack of anatomical information by employing attenuation and scatter uncorrected PET data within the attenuation map (Peyrat et al., 2012). The method is similar to the automatic contour detection method described previously for attenuation map modeling (Zaidi et al., 2003). SNAC, on the other hand, uses the image domain to identify contours rather than the sinogram domain. Transmission-less attenuation correction reduces radiation dose and significantly reduces acquisition time, allowing for increased patient throughput (Herzog et al., 2005).

By establishing a large number of points on a spatially normalized brain surface, the 3D-standard surface projection (3D-SSP) method analyzes the data of an individual with the database of healthy controls. The findings can be utilized to identify cortical areas with statistically significant impairments. Because of the underlying statistical calculations, these deficiency maps are also known as Z-score maps (or simply Z-maps). They help readers recognize patterns and make differential diagnosis easier. Despite the quantitative results, motion correction had only a little impact on the Z score image of the 3D-SSP study in a qualitative sense (Ikari et al., 2012, Wong et al., 2010). As shown in figures 7.12 and 7.13, if ^{18}F-FDG PET images are employed qualitatively as in visual interpretation, a little head motion will not impact the diagnostic outcome.

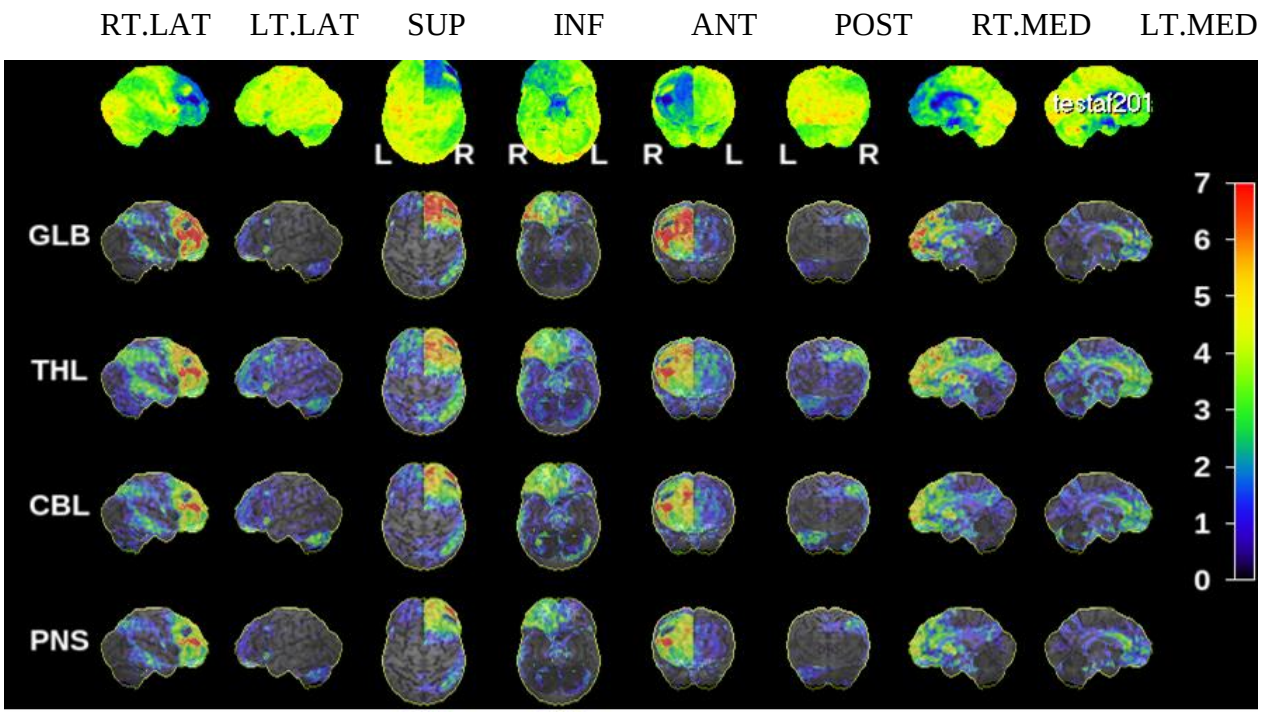

Figure 7.12: Z score image of 3D-SSP analysis global normalization nMC-PET.

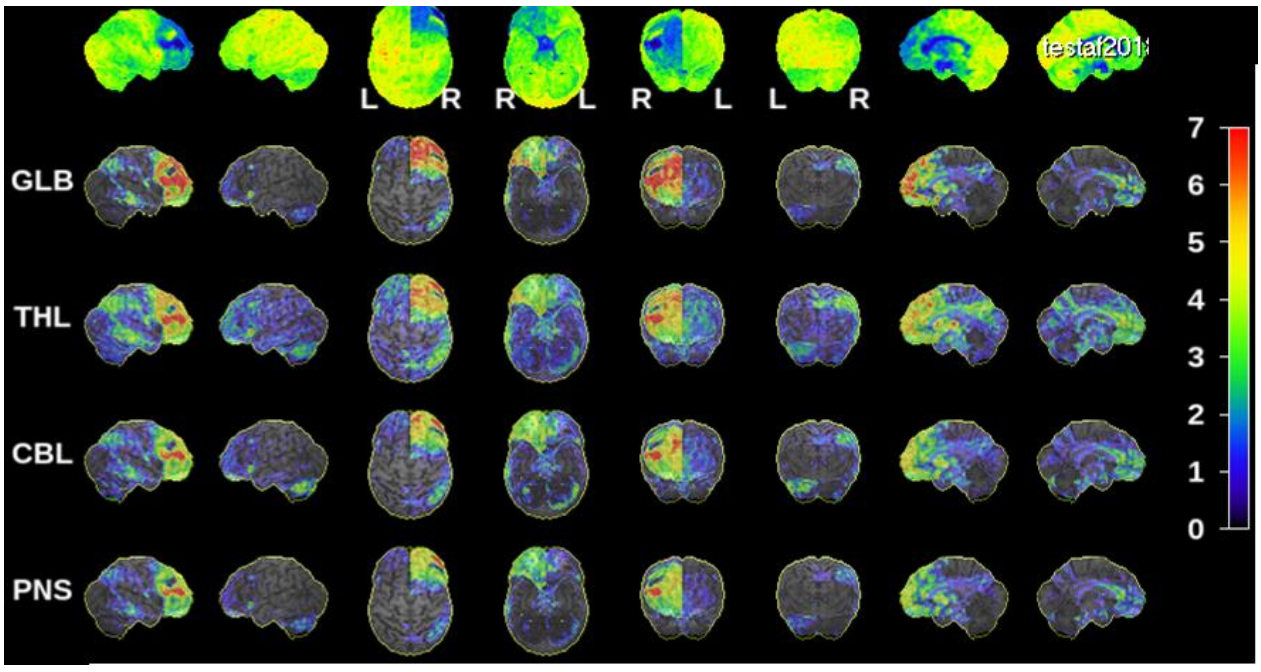

Figure 7.13: Z score image of 3D-SSP analysis global normalization MC- PET.

Chapter 8. Conclusions and Future Work

Motion artifacts are still present in many clinical images even with state-of-the-art CT scanners, especially in patients with mental disorders, stroke, and children. Sometimes a repeat scan is essential to acquire an artifact-free image, which certainly increases the radiation dose to patients. The data-driven ME and MC approach is based on measured raw data and successfully removed motion artifacts in head CT scans for a variety of rigid human head movements in clinical scans. Furthermore, it can be easily implemented to correct motion artifacts in clinical head helical CT scans as no further measurements are needed, and decrease the number of repeat scans. We conclude that, if the motion can be accurately determined, the established approaches can provide accurate and artifact-free MC images with most types of head motion expected to be encountered in CT imaging.

The data-driven motion estimation and compensation approach is based on measured raw data and successfully removed MA in head CT scans for a variety of rigid human head movements in clinical scans. Furthermore, it can be easily used in clinical head helical CT scans with MA as no further measurements are needed. Moreover, the smoothing kernel length, projection tolerance, and angle rebin have a considerable impact on motion estimation along with motion compensation in the data-driven algorithm. All experiments indicate that the SK 60, PT 0.001, and AR 8 produce acceptable artifact-free images. These scans were considered diagnostically appropriate and significantly decreased the number of repeat scans.

The data-driven iterative motion compensation method for head CT improves the quantitative and qualitative accuracy of the PET/CT brain image that is impacted by patient movement significantly. The motion-corrected CT PET/CT images were always superior. In brain PET, the attenuation map has an impact on both absolute and relative quantitation. The technique could be useful for both stand-alone helical CT scans and also in the CT part of hybrid imaging systems such as SPECT/CT and PET/CT.

The average time to perform motion correction on a normal head scan is about 8-10 hours. The first 1-2 hours are for the motion estimation, and 6-8 hours are required on a GPU for the final reconstruction. The bottleneck is the final iterative reconstruction. The future work could be the acceleration of final reconstruction. It can be achieved by the acceleration of the motion estimation.

As the motion can be different, it can be large in certain views but little in others. One can formulate an estimation scheme that does more computation on motion-affected views, but less on other views. This requires an initial identification of the views possibly affected by motion before the actual estimation. For example, similarity metrics (e.g. mean structural similarity index) can be measured for all adjacent views, which will probably produce a profile that can be used to identify views that are likely to be affected by motion. When performing the estimation, early iterations will only focus on the possible motion-affected views. Another way can be the use of advanced hardware for further acceleration of the final reconstruction such as implementing the whole iterative algorithm on GPU or replacing the iterative reconstruction with an iterative FBP reconstruction.

The data-driven method has been designed for rigid motion correction, it would be exciting to investigate how to extend it to non-rigid motion correction. For the non-rigid motion, more parameters need to be estimated in each view, compared with the previous six rigid parameters. One can calculate the derivative of the projection intensity with respect to each non-rigid parameter. From those derivatives, one can obtain a first estimate of the motion fields across views. Then, the motion compensation with this initial motion estimate can be performed, and repeat the motion estimation and compensation for several iterations until convergence.

The data-driven ME and MC approach is based on measured raw data and successfully removed motion artifacts in head CT scans for a variety of rigid human head movements in clinical scans. We conclude that this approach can offer accurate and artifact-free MC images with various types of head motion expected in CT imaging if the data is sufficient for accurately determining the motion. Furthermore, it can be easily implemented to correct motion artifacts in clinical head helical CT scans as no further measurements are needed, and it will possibly decrease the number of repeat scans. The technique could be very useful for both stand-alone helical CT scans and also in the CT part of hybrid imaging systems such as SPECT/CT and PET/CT. The data-driven iterative motion compensation method for head CT significantly increases the quantitative and qualitative accuracy of the PET/CT brain image affected by patient movement.

References

Aichert, A., Berger, M., Wang, J., Maass, N., Doerfler, A., Hornegger, J., and Maier, A. K., Epipolar consistency in transmission imaging, In: IEEE Trans. Med. Imaging 34 (2015) 2205–2219.

Akamatsu, M., Yamashita, Y., Akamatsu, G., et al. Influences of reconstruction and attenuation correction in brain SPECT images obtained by the hybrid SPECT/CT device: evaluation with a 3-dimensional brain phantom. Asia Oceania J. Nucl. Med. Biol.2 (2014) 24-29.

Allmendinger, AM., Tang, ER., Lui, W., et al., Imaging of stroke: perfusion CT overview of imaging technique, interpretation pearls, and common pitfalls, AJR Am. J. Roentgenol. 198 (2012) 52-62.

Anton-Rodriguez, JM., Sibomana, M., Huisman, MC., Matthews, JC., Feldmann, M., et al. Investigation of motion-induced errors in scatter correction for the HRRT brain scanner. IEEE Nucl Sci Symp Conf Rec (2010) 2935–2940.

Ay, MR., Sarkar, S., Computed Tomography based attenuation correction in PET/CT: principles, instrumentation, protocols, artifacts, and future trends. Iranian Journal of Nuclear Medicine.15 (2007) 1-29.

Bailey D. L., Townsend D. W., et. al., Positron Emission Tomography, London: Springer-Verlag London Limited, (2005).

Bailey D. L., Transmission scanning in emission tomography. Eur. J. Nucl. Med 25 (1998) 774–787.

Barrett, J. F., and Keat, N., Artifacts in CT: Recognition and avoidance. Radiographics, 24 (2004) 1679–1691.

Barrett, J. F., and Keat, N., Artifacts in CT: recognition and avoidance. Radiographics. 24 (2004) 1679-1691.

Beister, M., Kolditz, D., and Kalender, W. A., Iterative reconstruction methods in X-ray CT. Physica Medica, 28 (2012) 94–108.

Berger, M., et al., Motion compensation for cone-beam CT using Fourier consistency conditions, Phys. Med. Biol. 62 (2017) 7181-7215.

Beyer, T., Tellmann L., Nickel, I., et al. On the use of positioning aids to reduce misregistration in the head and neck in whole-body PET/CT studies. J. Nuc. Med. 46 (2005) 596-602.

Beyer, T., Townsend, D. W., Brun, T., Kinahan, P. E., Charron, M., Roddy, R., Jerin, J., Young, J., Byars, L., and Nutt, R. A combined PET/CT scanner for clinical oncology. J. Nucl. Med., 41 (2000) 1369–1379.

Bhowmik, U. K., Iqbal, M. Z., and Adhami, R. R., Mitigating motion artifacts in FDK-based 3D cone-beam brain imaging system using markers, Cent. Eur. J. Eng. 2 (2012) 369.

Bloomfield, P. M., Spinks, T. J., Reed, J., Schnorr, L., Westrip, A. M., et al., The design and implementation of a motion correction scheme for neurological PET. Phys Med Biol 48 (2003) 959–978.

Boas, F. E., and Fleischmann, D., CT artifacts: causes and reduction techniques. Imaging Med., 4 (2012) 229–240.

Bodensteiner, C., Darolti, C., Schumacher, H., Matthäus, L., Motion and positional error correction for cone beam 3D reconstruction with mobile C-arms, Med. Image Comput. Comput. Assist. Interv. Int. 10 (2007) 177.

Bongartz, G., Golding, SJ., Geleijns, J., et al., European Commission guidelines on quality criteria for computed tomography. https://op.europa.eu/en/publication-detail/-/publication/d229c9e1-a967-49de-b169-59ee68605f1a (1999).

Boone, J. M., Hendee, W. R., McNitt-Gray, M. F., et al., Radiation exposure from CT scans: how to close our knowledge gaps, monitor and safeguard exposure-proceedings and recommendations of the radiation dose summit. Radiology. 265 (2012) 544-554.

Brady, Z., Taylor, ML., Haynes, M., et al., The clinical application of PET/CT: a contemporary review, Australasian Physical & Engineering Sciences in Medicine. 31 (2008) 90-109.

Brady, Z., Taylor, M. L., Haynes, M., Whitaker, M., Mullen, A., Clews, L., Partridge, M., Hicks, R.J., Trapp, J. V., The clinical application of PET/CT: a contemporary review. Australas Phys Eng Sci Med. June 31 (2008) 90-109.

Brenner, D., Hall, E. J., Computed tomography - an increasing source of radiation exposure. N. Engl. J. Med., 357 (2007) 2277– 2284.

Brink, JA., Amis, ESJR., Image Wisely: a campaign to increase awareness about adult radiation protection. Radiology 257 (2010) 601–602.

Brodoefel, H., Kramer, U., Reimann, et. al, Dual-source CT with improved temporal resolution in the assessment of left ventricular function: a pilot study. Am. J. Roentgenol., 189 (2007) 1064–1070.

Bushberg, J. T., The essential physics of medical imaging, Philadelphia: Lippincott Williams & Wilkins, a Wolters Kluwer, 2nd Edition (2012).

Cherry, S. R., Badawi, R. D., and Qi, J. Essentials of in vivo biomedical imaging. CRC Press, Hoboken, NJ, USA (2015).

Cherry, S., Sorenson, J., Phelps, M., Physics in Nuclear Medicine. Saunders, Elsevier Inc., Philadelphia, 4th edition, (2012).

Clackdoyle, R., Desbat, L., Full data consistency conditions for cone-beam projections with sources on a plane, In: Phys. Med. Biol. 58 (2013) 8437.

Costes, N., Dagher, A., Larcher, K., Evans, A. C., Collins, D. L., et al., Motion correction of multi-frame PET data in neuroreceptor mapping: simulation-based validation. Neuroimage 47 (2009) 1496–1505.

Dance, D. R., Christofides, S., Maidment, A. D. A., McLean, I. D., and Ng, K. H. Diagnostic radiology physics: a handbook for teachers and students. International Atomic Energy Agency (IAEA), Vienna, Austria, (2014).

Davidson, AJ., Shrivastava, PP., Jamsen, K., et al. Risk factors for anxiety at induction of anesthesia in children: a prospective cohort study Pediatric. Anesthesia.16 (2006) 919-927.

Desbat, L., S. Roux, and P. Grangeat, Compensation of some time-dependent deformations in tomography, IEEE Trans. Med. Imaging 26 (2007) 261–269.

Edlow, JA., Caplan, LR., Avoiding pitfalls in the diagnosis of subarachnoid hemorrhage. New Engl. J. Med. 342 (2000) 29-36.

Fahmi, F., Beenen, L. F. M., Streekstra, G. J., Janssen, N. Y., De Jong, H. W., Riorda, A., Roos, Y. B., Majoie, C. B., Van Bavel, E., and Marquering, H. A. Head movement during CT brain

perfusion acquisitions of patients with suspected acute ischemic stroke. Eur. J. Radiol.82:2334-2341 (2013).

Fahmi, F., Marquering, HA., Borst, J., et al., 3D movement correction of CT brain perfusion image data of patients with acute ischemic stroke. Neuroradiology.56 (2014) 445-452.

Feldkamp, L. A., Davis, L. C., Kress J. W., Practical cone-beam algorithm, J. Opt. Soc. Am, A6, (1984) 612-619.

Ferrando, O., Foppiano, F., et al., PET/CT image quantification for diagnostic and radiotherapy applications. Journal of Diagnostic Imaging in Therapy, 2 (2015) 18-29.

Fessler, JA., Statistical image reconstruction methods for transmission tomography: Handbook of Medical Imaging: Medical Image Processing and Analysis. SPIE; FL, USA: 1 (2000) 1-70.

Fulton R., Hutton, B. F., Braun, M., Ardekani, B., and Larkin, R., Use of 3D reconstruction to correct for patient motion in SPECT. Phys. Med. Biol., 39 (1994) 563–574.

Fulton R., Steve, R. M., Eberl, S., Pfeiffer, J., Constable, C., and Fulham, M., Correction for head movements in positron emission tomography using an optical motion tracking system. IEEE Trans. Nucl. Sci., 49 (2002) 116–123.

Gendrin, C. et al., Monitoring tumor motion by real-time 2D/3D registration during radiotherapy. In: Radiother. Oncol. 102 (2012) 274.

Gonzalez, J. C., Rausch, I., et al., Hybrid imaging: instrumentation and data processing, Front. Phys., 18 May (2018).

Gullberg, G. T., Tsui, B. M. W., Crawford, C. R., Edgerton, E. R., Estimation of geometrical parameters for fan-beam tomography, Phys. Med. Biol. 32 (1987) 1581–1594.

Hahn, J., H. Bruder, C. Rohkohl, T. Allmendinger, K. Stierstorfer, T. Flohr, and M. Kachelrieß, Motion compensation in the region of the coronary arteries based on partial angle reconstructions from short scan CT data, Med. Phys. 44 (2017) 5795–5813.

Hanzelka, T., Dusek, J., Ocasek, F., et al., Movement of the patient and the cone-beam computed tomography scanner: objectives and possible solutions, Oral Surg. Oral Med. Oral Pathol. Oral Radiol. 116 (2013) 769-773.

Hausmann, D., Dinter D., et al., The impact of acquisition time on image quality in whole body ^{18}F-FDG PET/CT for cancer staging, Journal of Nuclear Medicine, 40 (2012) 255-58.

Helgason, S., et al., Radon Transform - Second Edition, (1999) 190.

Herzog, H., Tellmann, L., Fulton, R., Stangier, I., Rota-Kops, E., Bente, K., Boy, C., Hurlemann, R., and Pietrzyk, U., Motion artifact reduction on parametric PET images of neuroreceptor binding. J. Nucl. Med., 46 (2005) 1059–1065.

Hoffman, EJ., Cutler, PD., Digby, WM., Mazziotta, JC., 3-D phantom to simulate cerebral blood flow and metabolic images for PET. IEEE Trans Nucl Sci 37(2) (1990) 616–620.

Hsieh, J., Computed tomography: Principles, design, artifacts and recent advances. SPIE Press Monograph, Hoboken, NJ, USA, 2nd edition, (2009).

Huang, SC., Hoffman, EJ., Phelps, ME., et al., Quantitation in positron emission computed tomography: 2. effects of inaccurate attenuation correction. J Comp Assist Tomogr 3 (1979) 804–814.

Hudson, HM., Larkin, RS., Ordered subsets of projection data, IEEE Trans. Med. Imaging. 13 (1994) 601-609.

Ikari, Y., Nishio, T., Makishi, Y., et al., Head motion evaluation and correction for PET scans with ^{18}F-FDG in the Japanese Alzheimer's disease neuroimaging initiative (J-ADNI) multi-center study, Ann Nucl Med 26 (2012) 535–544.

Jacobson, M. W., and Stayman, J. W., Compensating for head motion in slowly-rotating cone-beam CT systems with optimization transfer based motion estimation, 8 IEEE Nuclear Science Symposium Conference Record. Germany, (2008) 5240-5245.

Jaffray, D. A., Image-guided radiotherapy: from current concept to future perspectives. Nat. Rev. Clin. Oncol., 9 (2012) 688–699.

Ji, F., Juntunen, M., Hietanen, L., Electrical crosstalk in front-illuminated photodiode array with different guard ring designs for medical CT applications. Nucl Instrum Methods Phys Res Sect A. 607 (2009) 150–153.

Kaste, S., Issues specific to implementing PET-CT for pediatric oncology: what we have learned along the way. Pediatr. Radiol., 34 (2004) 205–213.

Katsevich A., Silver M., and Zamyatin A., Local tomography and the motion estimation problem, SIAM J. Imaging Sci.; 4 (2011) 200.

Keller, S., Sibomana, M., Olesen, O., Svarer, C., Holm, S., et al. Methods for motion correction evaluation using FDG human brain scans on a high-resolution PET scanner. J Nucl Med., 53 (2012) 495–504.

Khalil, M. M., Basics of the PET imaging, Gewerbestrasse: Springer International Publishing, 2017.

Kim, J. H., Nuyts, J., Kuncic, Z., Fulton, R., The feasibility of head motion tracking in helical CT: a step toward motion correction, Med. Phys.40 (2013) 41903.

Kim, J., Nuyts, J., Kyme, A., et al., A rigid motion correction method for helical computed tomography (CT). Phys. Med. Biol. 60 (2015) 2047-73.

Kim, J., Sun, T., Alcheikh, AR., et al., Correction for human head motion in helical x-ray CT. Phys. Med. Biol. 61 (2016) 1416-1438.

Kinahan, P. E., Hasegawa, B. H., Beyer, T., X-ray based attenuation correction for PET/CT scanners. Semin. Nucl. Med, 33 (2003) 166–179.

Kinahan, PE., Townsend, DW., Beyer, T., et al., Attenuation correction for a combined 3D PET/CT scanner. Med. Phys, 25 (1998) 2046–2053.

Kyme, A., Stephen, S., Meikle, S., Angelis, G., Ryder, W., Popovic, K., Yatigammana, D., and Fulton, R. Markerless motion tracking of awake animals in positron tomography. IEEE Trans. Med. Imag., 33 (2014) 2180–2190.

Leng, S., B. Nett, M. Speidel, and G.-H. Chen, Motion artifact reduction in fan-beam and cone-beam computed tomography via the fan beam data consistency condition (FDCC), In: Proc. SPIE 6510, Med. Imaging (2007).

Levine, M. S., Sidky, E. Y., and Pan, X., Consistency conditions for cone-beam ct data acquired with a straight-line source trajectory, In: Tsinghua Sci. Technol. 15 (2010) 56–61.

Lewellen, T. K., Karp, J. S., PET systems. In: Wernick et al., Emission Tomography: The Fundamentals of PET and SPECT. Elsevier; CA, USA: 12 (2004) 169-178.

Li, L., Chen, Z., Jin, X., et al., Experimental measurement of human head motion for high-resolution computed tomography system design, Opt. Eng. 49 (2010) 063201.

Logan, J., Fowler, JS., Volkow, ND., Wang, GJ., Ding, YS., et al., Distribution volume ratios without blood sampling from graphical analysis of PET data. J Cereb Blood Flow Metab 16 (1996) 834–840.

Lu, W., and Mackie, T. R., Tomographic motion detection and correction directly in sinogram space, Phys. Med. Biol. 47 (2002) 1267– 1284.

Ludwig, D., The radon transform on euclidean space, In: Commun. Pure Appl. Math. 19.1, (1966) 49–81.

Malviya, S., Voepel-Lewis, T., Eldevik, O. P., Rockwell, D. T., Wong, J. H., and Tait, A. R. Sedation and general anesthesia in children undergoing MRI and CT: adverse events and outcomes. Br. J. Anaesth., 84 (2000) 743–748.

Man, B. D., Basu S., Distance-driven projection and back projection in three dimensions. Phys. Med. Biol. 49 (2004) 2463-2475.

Marchant, T. E., Price, G. J., Matuszewski, B. J., and C. J. Moore, Reduction of motion artifacts in on-board cone beam CT by warping of projection images, Br. J. Radiol. 84.999 (2011) 251–264.

Marcus, C., Mena E, Subramaniam RM. Brain PET in the diagnosis of Alzheimer's disease. Clin Nucl. Med. 39 (2014) 413–422.

Metzler, S. D., Greer, K. L., and Jaszczak, R. J., Helical pinhole SPECT for small-animal imaging: a method for addressing sampling completeness, IEEE Trans. Nucl. Sci. 50 (2003) 1575–1583.

Mourik, J. E., Lubberink, M., Van, V. F. H., Lammertsma, A. A., Boellaard, R., Offline motion correction methods for multi-frame PET data. Eur J. Nucl. Med. Mol. Imag., 36 (2009) 2002–2013.

Orlov, S. S., Theory of three-dimensional reconstruction. I. Conditions for a complete set of projections, Sov. Phys. Crystallogr. 20 (1975) 312– 314.

Peyrat, JM., Joshi, A., Mintun, M., et al., An automatic method for the quantification of uptake with Florbetapir imaging. Soc. Nucl. Med. 53 (2012).

Physicsopenlab: https://physicsopenlab.org/2018/02/13/x-ray-emission/

Polster, C., Hahn K., et. al., Improving material decomposition by spectral optimization of photon-counting computed tomography, Physics of Medical Imaging. 9783 (2016) 97831.

Popilock, R., Sandrasagaren, K., Harris L, et al., CT artifact recognition for the nuclear technologist. J. Nucl. Med. Technol.36 (2008) 79-81.

Quinn, B., Dauer, Z., Pandit-Taskar N, et al. Radiation dosimetry of 18F-FDG PET/CT: incorporating exam-specific parameters in dose estimates. BMC Med. Imaging 16 (2016) 41.

Rachel, A. P., and Palmer, M. R., Essentials of nuclear medicine and instrumentation, West Sussex: John Wiley & Sons, Ltd, (2013) 103-134.

Radiologycafe:www.radiologycafe.com/radiology-trainees/frcr-physics-notes/production-of-x-rays

Rahmim, A., et al., Strategies for motion tracking and correction in PET Clinics, 2, (2007) 251-266.

Raj, R., Siironen, J., Skrifvars, MB., et al., Predicting outcome in traumatic brain injury: development of a novel computerized tomography classification system. Neurosurgery.75 (2014) 632-647.

Reiser, M. F., Becker, C. R., Nikolaou, K., and Glazer, G., editors, Multislice CT. Springer, Berlin, 3rd edition (2009).

Roberts, R. O., Knopman, D. S., Cha, R. H., et al., Diabetes, and elevated hemoglobin A1c levels are associated with brain hypometabolism but not amyloid accumulation. J Nucl Med 55 (2014) 759–764.

Rohkohl, C., Herbert, B., Karl, S., et al., Improving best phase image quality in cardiac CT by motion correction with MAM optimization, Med. Phys. 40 (2013) 031901.

Roux, S., Desbat, L., Koenig, A., and Grangeat, P., Exact reconstruction in 2D dynamic CT: compensation of time-dependent affine deformations, Phys. Med. Biol. 49 (2004) 2169–2182.

Rydberg, J., Buckwalter, K. A., et al., Multisection CT: scanning techniques and clinical applications, Radiographics, 20 (2000) 1787-1806.

Saha, G. B., Basics of PET imaging, Physics, Chemistry and Regulations, 3rd Edition, NY, USA, Springer (2016).

Savitzky, A., and Golay, M. J. E., Smoothing and differentiation of data by simplified least squares procedures, Anal. Chem. 36 (1964) 1627-1639.

Schäfer, D., Bertram, M., Conrads N., Motion compensation for cone-beam CT based on 4D motion field of sinogram tracked markers, Int. Congr. Ser., 1268 (2004).

Schöder, H., Erdi, E. Y., et al., Clinical implication of different image reconstruction parameters for interpretation of whole-body PET studies in cancer patients, Journal of Nuclear Medicine, 45 (2004) 559-566.

Schretter, C., et. al., Image-based iterative compensation of motion artifacts in computed tomography, Med. Phys. 36 (2009) 5323–5330.

Shefer E., Altman A., et al., State of the art of CT detectors and sources: a literature review, Current Radiology Report, 1 (2013) 76–91.

Sisniega, A., Stayman, J., Yorkston, J., et al. Motion compensation in extremity cone-beam CT using a penalized image sharpness criterion. Phys. Med. Biol. 62 (2017) 3712-3734.

Slambrouck, K.. V., Nuyts J., Metal artifact reduction in computed tomography using local models in an image block iterative scheme. Med. Phys. 39 (2012) 7080-7093.

Steve, U., Marc, C., et al., Design and performance of a 32-slice CT detector system using back-illuminated photodiodes. Proc SPIE. 5368 (2004) 40–51.

Suchorska, B., Tonn, J. C., and Jansen, N. L., PET imaging for brain tumor diagnostics. Curr Opin Neurol 27 (2014) 683–688.

Sun, T., Rigid motion correction for head CT imaging, KU Leuven, Biomedical Science Group, 2018.

Sun, T., Clackdoyle, R., Kim, J. H., et al., Estimation of local data insufficiency in motion-corrected helical CT, IEEE Transaction on Radiation and Plasma Medicine Science. 1 (2017) 346-357.

Sun, T., Fulton, R., Kim, J. H., and Nuyts, J., Data-driven helical CT rigid motion correction, in Proc. of the 13th Int. meeting on fully three-dimensional image reconstruction in Radiology and Nuclear Medicine, (2015) 444–447.

Sun, T., Kim, J. H., Fulton, R., et al., An iterative projection-based motion estimation and compensation scheme for head x-ray CT. Medical Physics. 43 (2016) 5705-5716.

Tong, S., Alessio, A. M., and Kinahan, P. E., Image reconstruction for PET/CT scanners; past achievements and future challenges. Imaging in Medicine, 2 (2010) 529.

Townsend, D. W., Wensveen, M., Byars, L. G., et al., A rotating PET scanner using BGO block detectors: Design, performance, and applications. J Nucl. Med. 34 (1993) 1367–1376.

Tuy, H. K., An inversion formula for cone-beam reconstruction. In: SIAM J. Appl. Math. 43 (1983) 546–552.

Wachtel, R. E., Dexter, F., and Dow, A. J. Growth rates in pediatric diagnostic imaging and sedation. Anesth. Analg., 108 (2009) 1616–1621.

Wagner, A., Schicho, K., Kainberger, F., Birkfellner, W., Grampp, S., and Ewers, R. Quantification and clinical relevance of head motion during computed tomography. Invest. Radiol., 38 (2003) 733–741.

Wang, G., and Vannier, M. W., Preliminary study on helical CT algorithms for patient motion estimation and compensation. IEEE Trans. Med. Imag. 14 (1995) 205.

Wardak, M., Wong K. P., Shao W., Dahlbom M., Kepe V., et al. Movement correction method for human brain PET images: application to quantitative analysis of dynamic 18F-FDDNP scans. J Nucl. Med., 51 (2010) 210–218.

Watson, C. C., Casey, M. E., Michel, C., Bendriem, B., Advances in scatter correction for 3D PET/CT. IEEE Nucl. Sci. Symp. Conf. Rec 5 (2004) 3008–3012.

Westermann, B., and Hauser, R., Online head motion tracking applied to the patient registration problem, Comput. Aided Surg., 5 (2000) 137.

Wong, KP., Wardak, M., Shao, W., Dahlbom, M., Kepe, V., et al., Quantitative analysis of ^{18}F-FDDNP PET using subcortical white matter as reference region. Eur. J. Nucl. Med. Mol. Image 37 (2010) 575–588.

Xue, Z., Antani, S., Long, LR., et al., Window classification of brain CT images, AMI Annu. Sym. Proc. (2012) 1023-1029.

Yan, H., Zhen, X., et al., Progressive cone-beam CT dose control in image-guided radiation therapy, Med. Phys., 40 (2013) 060701.

Yazdi, M., Beaulieu, L., Artifacts in spiral x-ray CT scanners: problems and solutions. Int. J. Biol. Life Sci. 4 ((2008) 135-139.

Ye, Y., Zhao, S., Yu, H., and Wang, G., A general exact reconstruction for cone-beam CT via back-projection- filtration, IEEE Trans. Med. Imaging 24 (2005) 1190–1198.

Yu, H., and Wang, G., Data consistency based rigid motion artifact reduction in fan-beam CT, IEEE Trans. Med. Imag. 26 (2007) 249.

Zaidi, H., Hasegawa, B., Determination of the attenuation map in emission tomography. J Nucl Med 44 (2003) 291–315.

Zaidi, H., Montandon, M. L., Meikle, S., Strategies for attenuation compensation in neurological PET studies. NeuroImage 34 (2007) 518–541.

Zaidi, H., Montandon, M. L., Slosman, D. O., Attenuation compensation in cerebral 3D PET: effect of the attenuation map on absolute and relative quantitation. Eur. J. Nucl. Med. Mol. Imag. 31 (2004) 52–63.

Zaitsev, M., Dold, C., Sakas, G., Henning, J., and Speck, O., Magnetic resonance imaging of freely moving objects: Prospective real-time motion correction using an external optical motion tracking system. NeuroImage, 31 (2006) 1038–1050.

Curriculum Vitae

Academic teachers

My academic teachers at Philipps University Marburg Germany are;

Prof. Dr. Markus Luster
Dr. Tino Schurrat

My academic teachers at University of Sydney, Australia;

Prof. Dr. Roger Fulton

My academic teachers in my Masters studies;

Prof. Dr. Inam-ur-Rehman
Prof. Dr. M. Khaleeq-ur-Rehman
Prof. Dr. M. Shahid Rafique
Prof. Dr. Maqsood Ahmed
Prof. Dr. Aurangzeb
Prof. Dr. Tariq Majeed
Prof. Dr. Matiullah Marwat
Prof. Dr. Masroor Ikram
Prof. Dr. Nasir Majid
Prof. Dr. Sikander Majid
Prof. Dr. Anwer Latif
Prof. Dr. Khurrum Siraj
Prof. Dr. Muhammad Yousaf
Dr. Muhammad Sohaib

Acknowledgment

Whole praise to ALLAH, the sovereign power, the creator of the universe, WHO gave us knowledge, made us the superior creature, blessed us with knowledge, and enabled me to accomplish this task.

All respects are to Holy Prophet Muhammad (Sallallaho-Alaihe-Wasallum), WHO is forever a source of knowledge and guidance for the whole of mankind.

My greatest appreciation is for my mentor Prof. Dr. Markus Luster, department of Nuclear Medicine, Philipps University Marburg, for his guidance, immense knowledge, and expertise in the field, which has been particularly valuable to this thesis. His leadership abilities gave me a passion for research work. His support and friendly behavior encouraged me a lot to complete this project.

I also express my profound gratitude to Dr. Tino Schurrat as my advisor for his interest in the project, tremendous cooperation, and valuable suggestions. He is always there to help, no matter when I got stuck with my project or when I seek suggestions even on minor things. I am extremely thankful to him for his kind cooperation and encouragement in this project.

I further extend my greatest appreciation and thanks to Prof. Dr. Roger Fulton from the University of Sydney for his keen interest and guidance during the project work. He is always available for discussion about the project. I am also extremely thankful to him for providing me an opportunity to visit Sydney Australia to carry out the experimental work at Westmead Hospital Sydney Australia. Furthermore, he provided me CT motion correction prototype algorithm and data of the patients.

Most importantly I would like to thank my best friend and my husband, Dr. Arslan Usman for his care and unconditional support throughout this project. His confidence in me always gave me the strength and courage to achieve my goal. My best regards to my parents, brothers, and sisters for their love, affection, encouragement, and prayers that are always with me in every front of my life.

I would like to express my deep wishes and thanks to my best friend Dr. Sobia, Dr. Rafia, and Dr. Nouroze for their cooperation and moral support.

Ehrenwörtliche Erklärung

Ich erkläre ehrenwörtlich, dass ich die dem Fachbereich Medizin Marburg zur Promotionsprüfung eingereichte Arbeit mit dem Titel

Data-driven iterative image reconstruction for motin correction in head computed tomography

in der Klinik für Nukearmedizin unter Leitung von Prof. Dr. Markus Luster und mit Unterstützung durch Dr. Tino Schurrat ohne sonstige Hilfe selbst durchgeführt und bei der Abfassung der Arbeit keine anderen als die in der Dissertation aufgeführten Hilfsmittel benutzt habe. Ich habe bisher weder einem in- oder ausländischen medizinischen Fachbereich ein Gesuch um Zulassung zur Promotion eingereicht, noch die vorliegende oder eine andere Arbeit als Dissertation einem medizinischen Fachbereich vorgelegt.

Ort, Datum, Unterschrift Doktorandin/Doktorand

Marburg, 27.03.2022 Afshan Ashfaq

„Die Hinweise zur Erkennung von Plagiaten habe ich zur Kenntnis genommen."

Ort, Datum, Unterschrift Referentin/Referent

Marburg, 27.03.2022 Prof. Dr. Markus Luster